

REPORT DOCUMENTATION PAGE

Form Approved
OMB No. 0704-0188

Public reporting burden for this collection of information is estimated to average 1 hour per response, including the time for reviewing instructions, searching existing data sources, gathering and maintaining the data needed, and completing and reviewing this collection of information. Send comments regarding this burden estimate or any other aspect of this collection of information, including suggestions for reducing this burden to Department of Defense, Washington Headquarters Services, Directorate for Information Operations and Reports (0704-0188), 1215 Jefferson Davis Highway, Suite 1204, Arlington, VA 22202-4302. Respondents should be aware that notwithstanding any other provision of law, no person shall be subject to any penalty for failing to comply with a collection of information if it does not display a currently valid OMB control number. PLEASE DO NOT RETURN YOUR FORM TO THE ABOVE ADDRESS.

1. REPORT DATE (DD-MM-YYYY)

10-29-2007

2. REPORT TYPE

final

3. DATES COVERED (From - To)

09-28-2004 to 08-31-2007

4. TITLE AND SUBTITLE

Micro Chemical Oxygen-Iodine Laser (COIL)

5a. CONTRACT NUMBER

HR0011-04-C-0140

5b. GRANT NUMBER

5c. PROGRAM ELEMENT NUMBER

5d. PROJECT NUMBER

5e. TASK NUMBER

5f. WORK UNIT NUMBER

6. AUTHOR(S)

Carol Livermore-Clifford

7. PERFORMING ORGANIZATION NAME(S) AND ADDRESS(ES)

Massachusetts Institute of
Technology
77 Massachusetts Avenue
Cambridge, MA 02139

8. PERFORMING ORGANIZATION REPORT NUMBER

9. SPONSORING / MONITORING AGENCY NAME(S) AND ADDRESS(ES)

DARPA
Tactical Technology Office
3701 North Fairfax Drive
Arlington, VA 22203-1714

10. SPONSOR/MONITOR'S ACRONYM(S)

DARPA

11. SPONSOR/MONITOR'S REPORT NUMBER(S)

12. DISTRIBUTION / AVAILABILITY STATEMENT

Approved for public release; distribution unlimited.

13. SUPPLEMENTARY NOTES

none

20071030285

14. ABSTRACT

It has been previously proposed to improve the performance and compactness of chemical oxygen-iodine lasers (COIL) through the replacement of some of their macroscale components with arrays of higher-performing microscale (MEMS) components. In this program, a MEMS singlet oxygen generator (SOG) to power a COIL laser was designed, microfabricated from silicon and glass wafers, and successfully demonstrated. The MEMS SOG contained an array of reaction channels for the chemical reaction of BHP and chlorine gas, a liquid-gas separator based on capillary effects, and integrated heat exchangers for thermal management. The MEMS SOG was shown to have high singlet delta oxygen yield, high output flow rates, and an ability to operate in near single-pass reactant utilization. The results were also shown to agree with the models. In addition, devices for a second generation MEMS COIL system (second generation MEMS SOG, MEMS steam generators to power ejector pumps, and component interfaces) were designed. Based on its models, the second generation MEMS SOG is predicted to operate at four times higher flow rates than the first generation MEMS SOG. Based on its models, the MEMS steam ejectors are predicted to offer a low vibration, compact source of driving fluid for a COIL pumping system.

15. SUBJECT TERMS

Chemical oxygen iodine laser; COIL; MEMS; microCOIL; singlet oxygen generator; SOG; singlet delta oxygen

16. SECURITY CLASSIFICATION OF:

a. REPORT
U

b. ABSTRACT
U

c. THIS PAGE
U

17. LIMITATION OF ABSTRACT

UU

18. NUMBER OF PAGES

16 + 108
attached

19a. NAME OF RESPONSIBLE PERSON

Carol Livermore-Clifford

19b. TELEPHONE NUMBER (include area code)
617-253-6761

*Department of Mechanical Engineering
Massachusetts Institute of Technology
Cambridge, MA 02139*

FINAL REPORT

for the project entitled

MICRO CHEMICAL OXYGEN-IODINE LASER (COIL)

Sponsored by

Defense Advanced Research Projects Agency
Tactical Technology Office (TTO)
Program: Micro Chemical Oxygen-Iodine Laser (COIL)
ARPA Order No. T171/00, Program Code: 4G10
Issued by DARPA/CMO under Contract No. MDA972-04-C-0140

PRINCIPAL

INVESTIGATOR: Carol Livermore-Clifford (Technical Contact)
SMA Assistant Professor of Manufacturing, Mech. Engineering
Massachusetts Institute of Technology
Tel: (617) 253-6761, FAX: (617) 258-6427
email: livermor@mit.edu

The views and conclusions contained in this document are those of the authors and should not be interpreted as representing the official policies, either expressed or implied, of the Defense Advanced Research Projects Agency or the U.S. Government.

Final Report: Micro Chemical Oxygen-Iodine Laser (COIL)

Task objectives

This program included an initial statement of work plus follow-on statements of work. The initial task objectives were to demonstrate a first generation single-chip microSOG. Given the short timeframe of the initial statement of work, the first device was not specifically optimized for maximum singlet oxygen production or efficiency but rather was an adaptation of an existing microchemical reactor in order to reduce the chip process development and manufacture time. The specific tasks during this initial phase were as follows:

1. SOG design
2. SOG chip manufacture
3. Test apparatus design and assembly
4. Testing
5. Data reduction and analysis

The initial statement of work provided initial proof of concept of the microSOG device and was subsequently added to in a follow-on statement of work. The purpose of the follow-on statement of work was to expand the microSOG testing in order to more completely understand the performance, capabilities, and limitations of the first generation of microSOG chips. The specific tasks during the follow-on were as follows:

1. Microfabrication of additional SOG chips
2. Design and assembly of singlet oxygen diagnostic by chemical titration
3. Testing
4. Data reduction and analysis

The success criteria for this work were that the measured singlet oxygen production per unit volume should be twice that of published SOGs, and that there should be agreement between the SOG analytical model and the test data.

Finally, there was one more follow-on statement of work. The purpose of this statement of work was to leverage the prior results to set the stage for a future, full-scale microCOIL program. The specific tasks during this follow-on were as follows:

1. Update microSOG model based on experimental results
2. Design a second generation microSOG based on the updated model
3. Conceptual design of steam generators for microCOIL pressure recovery system
4. Conceptual design of iodine injection system
5. Final report

The success criteria for this final follow-on statement of work were that the second generation model should agree with experiment, that the second generation microSOG

should be designed, and that conceptual designs and models of the iodine injection system and steam generator should be created.

General methodology

The tasks involved in this program were diverse and therefore required a range of methodologies. In general, the entire program focused on the creation and evaluation of technologies for microCOIL: a MEMS-based approach to creating more compact, higher-performing COIL systems by replacing the conventional components of a COIL system with arrays of higher-performing microcomponents. The overall methodology was a combination of conceptual design, detailed design, device modeling, microfabrication of MEMS chips to test, creation and calibration of test apparatus, experimental measurement of device performance, and reconciliation of the experimental results with the previously-created analytical models. The details of the methodologies employed for the microSOG aspects of the project are described in greater detail in the attached conference and journal publications; the details of the non-SOG aspects are described in greater detail below.

Technical challenges

It is not surprising, given the broad range of tasks, that the execution of this project included addressing a number of technical challenges in a number of different areas. One area that included significant technical challenges was the microfabrication of the microSOG chips. These microfabrication challenges and problems were successfully addressed through careful fabrication process design and attention to detail. The details of this work are written up in a journal article entitled "A MEMS Singlet Oxygen Generator – Part I: Device Fabrication and Proof of Concept Demonstration" that has been accepted for publication in the *IEEE Journal of Microelectromechanical Systems*. A preprint of this publication is included with this report. These matters were also addressed at the April 2005 program review.

A second set of technical challenges were faced in the testing of the microSOG chips to evaluate their performance. Because the microSOG chips were being tested alone, without subsequent injection of iodine or the possibility for gain diagnostics, it was necessary to measure directly the singlet delta oxygen concentration beyond the chip's exit. This is a known challenge in the COIL field; singlet delta oxygen is difficult to measure quantitatively because it has a long (and somewhat uncertain) lifetime, and because the most accurate measurement techniques require substantial hardware investment and substantial specific expertise. Our goal was to make several complementary measurements in order to assess the singlet delta oxygen production, including both quantitative and qualitative measures of singlet delta oxygen production. In the end, a range of qualitative measures were employed: visual observation of singlet delta oxygen's characteristic red dimol emission, mass spectrometry to observe the creation of oxygen, and spectroscopic measurement of the dimol emission spectrum. Two quantitative measures were initially proposed in order to provide corroboration of the results: quantitative measurement of singlet delta oxygen concentration via

measurement of its spontaneous emission spectrum, and quantitative measurement of singlet delta oxygen concentration through chemical titration.

The spontaneous emission measurement was implemented at MIT without significant problems; the main challenge was the large error bars accompanying the measurement. The chemical titration was also implemented, but it had more significant technical problems. In the chemical titration approach, the singlet delta oxygen that exited the chip was to be trapped, and its reaction with the trapping species was to be monitored in order to quantify the singlet delta oxygen production. Technical problems arose with the chemical titration approach, however. Because of the different operating pressures in various parts of the overall microSOG/test apparatus/chemical titration system, it proved difficult to pump the system down to its low operating pressure reliably without sucking some of the chemical titration fluid into the chip. The introduction of chemical titration fluid to the chip was a destructive event. Ultimately, the decision was made to abandon the chemical titration approach because of the significant risks to the valuable microSOG test chips. In its place, a different confirming measurement was chosen: absolutely-calibrated spectroscopy of the quantitative emission spectrum in collaboration with Physical Sciences Inc., who have created a highly accurate tool and methodology for making this measurement. The challenges associated with measuring the singlet delta oxygen concentration, along with the steps taken to overcome them, were addressed at the September 2005 and May 2006 program reviews.

A third challenge emerged in operating the microSOG devices at high flow rates. Because of the design of the fluidic distributors that deliver the reactants to the reaction channels, and because of the high viscosity of BHP, it required significant driving pressures (above the 4 atm that were actually employed during testing) to deliver the liquid reactants to the chip at high flow rates. However, these high pressures were not compatible with the otherwise reliable o-ring based packaging method that was ultimately chosen. Therefore, the devices were not tested at the upper part of their range of liquid reactant flow rates. This limited our ability to test at the upper part of the range of chlorine flow rates, and therefore limited the total achievable singlet delta oxygen production rate in these devices. Given that we only had one device design in this program, the higher flow rate regime remained unexplored. Ensuring that the next generation of devices will be able to be operated at higher flow rates was then a significant goal of the subsequent redesign of the microSOG device.

The final significant challenge was to reconcile the measured SOG data with the analytical models. Initially, the measured data did not seem consistent with the SOG model; it appeared that the singlet delta oxygen production was unphysically high. This technical challenge was met through an extensive updating of the analytical model of the microSOG. Ultimately it was realized that the experiments carried out here highlight the uncertainty of some of the standard COIL chemical kinetics constants. Using the uncertain constants as a fitting parameter resolved the problem; our results were then in agreement with the range of kinetics constants values given in the literature. The details of the singlet delta oxygen concentration measurement, the kinetics analysis, and the model reconciliation are given in a second paper entitled "A MEMS Singlet Oxygen Generator – Part II: Experimental Exploration of the Performance Space," which has

also been accepted for publication in the *IEEE Journal of Microelectromechanical Systems*.

Technical results

The technical results on the design, manufacture, testing, and model reconciliation for the microSOG will be described briefly here. A significantly greater level of detail is provided in the attached journal papers. In addition to the two journal papers mentioned above that have been accepted for publication, some of the results are captured in a third journal paper that has been submitted for publication in the *AIChE Journal*. This paper is entitled "Design of a Silicon-Based Microscale Trickle-Bed System for Singlet-Oxygen Production" and is also attached. The technical results on the design and modeling of future devices is not described in those papers and will therefore be described in greater detail below.

First generation microSOG

The technical results on the design, manufacture, and characterization of the microSOG may be summarized as follows. The device was designed in accordance with pre-existing technical models created during a prior HEL-JTO-funded study. The devices were implemented in a three-wafer stack. Two of the wafers were made of silicon. The first housed the reactant distributors, packed-bed reaction channels for singlet delta oxygen generation, and a gas-liquid separator to separate the exiting gas and liquid streams using capillary effects. The second housed the chip's connection ports and the integrated cross-flow heat exchanger to remove excess heat of reaction. The third wafer was made of Pyrex (for optical access) and contained no functional features. The silicon structure was protected from the reactants by a layer of silicon nitride that covered all of the silicon surfaces. Ultimately, the microfabrication yield rate of the final process approached 100%, with successive wafer stacks being created without leaks or other significant defects.

The microSOG chips were then characterized. First, their flow patterns were assessed, their pressure drops were measured, and the cooling capabilities of their heat exchangers were measured. Then their singlet delta oxygen generating capability was assessed. Using a combination of spectroscopic measurements downstream from the microSOG chips, kinetics analyses to relate those measured values to the values at the chip exit (which are most relevant for a complete microCOIL system), and model fits and comparisons to ensure that the kinetics analyses were accurate, the following conclusions were reached.

- The microSOG's basic functionalities (mixing, cooling, product separation) were all successfully demonstrated.
- Singlet delta oxygen yield at the chip outlet was determined to be as high as about 78%.
- The molar flow rate of singlet delta oxygen from the chip per unit volume (counting the entire volume of the chip, minus those parts that were exclusively devoted to single-chip packaging) was as high as 0.067 moles/liter/second. If

only the internal reaction volume were taken into account (as is the customarily done in evaluating SOGs), the flow rate per unit volume would be approximately twice that value. This is comparable to flow rates per unit of internal volume demonstrated in the last few years for the very best modern jet SOGs. Given that the microSOG data were taken on initial prototype, not-yet-optimized devices, this is a very favorable comparison.

- The microSOG chips operated at very high ratios of chlorine to BHP as compared with conventional SOGs. The microSOG was designed to operate at a ratio of peroxide ions to chlorine of 10:1, as compared to many tens to one for conventional SOGs. In practice, the SOG operation was measured over a range of ratios from about 3.7:1 to 13:1. The lower end of this range clogged as expected, and the higher end of this range operated without clogs, also as expected for the microdevice. This will permit essentially single-pass reactant utilization.
- The total flow rates of chlorine were limited by the need to stay above a 10:1 peroxide to chlorine ratio as described above and the limited ability to deliver high flow rates of BHP to the first generation device in the first generation package, also as described above. This limited the total flow rates of oxygen that were possible. Therefore, the observed flow rates of singlet delta oxygen per unit volume that were observed are about four times less than the flow rates that are expected to be possible when BHP is delivered at higher flow rates. This simply requires a redesign of the chip's reactant feed systems.

Second generation microSOG design and model

Overall, the first generation microSOG chip worked very well. The primary goal of the redesign was therefore to fix the one significant documented shortcoming of the initial device: a high interior flow resistance that led to leakage at the device-package interface when the device was operated at more than about 25% of the design flow rates. This challenge could be addressed either through device redesign to reduce the interior flow resistance or through the introduction of new packaging technologies. Because the microSOG system should be robust and convenient to use, the decision was made to redesign the microSOG system itself. The updates were guided by the second generation SOG model. The revised model is quite similar to the initial model, the framework of which was proved to be essentially accurate through the initial microSOG work. The updates that were made are described in more detail in the Technical Challenges section above, and in the second JMEMS article that accompanies this report.

The dominant pressure drop is in the pressure drop channels that serve to ballast the flow and distribute it evenly among the chip's 32 reaction channels. In particular, the pressure drops in the liquid distribution channels imposed the most stringent limits on the operation of the first generation devices. A reduction in the flow resistance of these originally 25 micron wide and 20 micron deep channels may be accomplished by increasing either their width or their depth, or by increasing both. The decision was made to increase their depth to 35 microns and their width to 30 microns, with a 2750 micron length. This gives a factor of four reduction in the flow resistance as compared with the first generation microSOG devices. It also ensures that the resulting channel structure is most sensitive to variations in the (better-controlled) width dimension, rather than to

variations in the (harder-to-control) depth dimension. This reduced sensitivity to microfabrication variations will reduce flow nonuniformity among the channels. The gas pressure drop channels are resized to 100 microns wide and 100 microns deep, with a length of 800 microns.

In order to ensure that the pressure drop channels will still effectively ballast the flow, the resistance of the reaction channels themselves must also be reduced by a factor of four. This is somewhat more complicated; the multiphase flow resistance of a packed bed channel is not simply described as Pouiseuille flow. The reaction channels were redesigned to contain approximately the same number of periods of the post pattern as in the original device, and to have the same bed porosity. However, the width of each channel, the post diameter, and the post periodicity were all increased to reduce the flow resistance, to 756 microns, 88 microns, and 113 microns respectively. Finally, the lengths of the reaction channels had to be resized in order to ensure that the reaction has time to go to completion with the new geometry, without being so long that losses increase unnecessarily. To meet these requirements, the new length is 0.75 cm. The model indicates that the resulting yield will be 76% for this geometry and for a He:Cl₂ flow rate that is four times the flow rate used in the initial round of experiments.

The capillary separator and cooling channels were also re-examined. The capillary separator did not need to be resized to accommodate the larger flow rate through the reaction channels, because it had been sized for these flow rates in the first place. In fact, the original capillary separator had been oversized (with about 7000 pores) by a factor of approximately three to compensate for any microfabrication difficulties that might have prevented all of the pores from forming. Since it has been shown that the pore fabrication process is robust, the capillary separator is reduced in the redesigned chip to 3000 pores. This is still an overdesign by a factor of about 50%; the overdesign will help to prevent leakage of liquid into the gas line, while the reduction in size will cut down on the volume of the microSOG chip. The cooling channels did not need to be significantly resized. They had been sized originally to ensure that the device could be adequately cooled at the design flow rates, so they are still capable of carrying out this task. A small increase in the length of the cooling channels may be included to span the slightly widened region of the reaction channels.

Iodine injection/SOG-nozzle interface design

The work done during this task focused on the questions of how best to inject iodine and how best to interface the SOG and nozzle hardware with each other and with the iodine injection system. The options included a) MEMS SOGs monolithically integrated with MEMS iodine injection/mixing nozzle hardware, b) MEMS SOGs externally interfaced to MEMS iodine injection/mixing nozzle hardware, or c) MEMS SOGs externally interfaced to conventional macroscale iodine injection/mixing nozzle hardware.

It was found that the primary argument for MEMS iodine injection and MEMS nozzles was one of system integration. Iodine is injected after the singlet delta oxygen exits the SOG and as it is entering the supersonic mixing nozzle. Supersonic mixing nozzle geometries for large scale devices are well known, and MEMS nozzles for microCOIL were preliminarily designed and modeled in the prior HEL-JTO-funded study. The conclusions of that work had indicated that a MEMS-scale nozzle could be created using

standard bulk micromachining techniques, and that its performance would be similar to that of a macroscale nozzle; the main exception to that statement is in the effects of boundary layers. Because boundary layers of given extent can occupy a larger percentage of a small mixing nozzle's area than they can of a large mixing nozzle's area, it was seen that the mixing nozzle required a certain minimum set of dimensions in order to operate successfully. This dimension was at the approximately half-centimeter scale, leaving open the possibility of coupling either a MEMS nozzle or a macroscale nozzle to the SOG and pump hardware. The other factor that comes into play is the ability to mix the iodine with the singlet delta oxygen stream. Cross-flow injection mixing has been demonstrated in MEMS systems, much like the iodine injection in macroscale COIL. The enhanced ability to create very small injection pores in MEMS, and the shorter flow distance that the iodine must travel to reach the center of the flow stream in MEMS, can in principle offer a performance benefit for MEMS nozzles: enhanced iodine/oxygen mixing. In practice, however, it is not clear that this offers a compelling argument for MEMS nozzles. The ability to implement iodine injection through tiny pores will be limited by iodine's tendency to solidify and form deposits on the walls of the injection pores. In addition, the mixing for COIL lasers, at least, has not been a major performance limiting factor.

Therefore, the primary potential benefit of MEMS iodine injectors and MEMS mixing nozzles was seen to be in system integration. Monolithically integrated MEMS devices can have extremely tight coupling between components because no external interface hardware is required. This enables very short residence times between the components and therefore reduces losses of excited species such as singlet delta oxygen due to mechanisms like pooling. Reduced losses offer higher yields at the point of singlet delta oxygen utilization, and therefore offer higher chemical efficiency for the laser. The reduction in residence time will be partially offset by increases in wall deactivation due to the higher surface to volume ratio for small, MEMS-scale flow paths. However, the cross-over from a pooling-dominated loss mechanism to a wall-deactivation-dominated loss mechanism was calculated to take place only after the flow paths reach a characteristic dimension of 1 mm or below for silicon dioxide or silicon nitride-coated walls. This small length-scale cross-over means that the benefits of tight component integration are very real, and could offer significant performance benefits for a completely MEMS microCOIL laser.

The challenge therefore came down to a matter of interfaces, and which system architecture offers the best system performance. Tight system integration pushes towards an all-MEMS solution, because the exit of the SOG may be routed directly to the inlet of the nozzle via the on-chip flow paths of a monolithic system. The question that was addressed in this work was whether an all-MEMS solution can meet the other requirements of the system. The main challenge was thermal control. The iodine injection hardware (and, to a lesser extent, the nozzle hardware) must be maintained at a high enough temperature to prevent iodine from solidifying on the hardware's surfaces. In contrast, the SOG hardware must be maintained at a reduced temperature in order to minimize the amount of water vapor in the exiting gas flow. Monolithic integration of MEMS-scale SOGs with MEMS-scale nozzles and iodine injection would require that the silicon structure be continuous between the SOGs and the nozzles. However, because silicon's thermal conductivity is very high, approaching that of copper, it is a challenge to

design a system that has structural and flow connections without having a thermal short between the components.

A model was created to examine the tradeoffs between monolithic integration of flow paths and thermal leakage. The essential requirement was that the thermal resistance between the nozzle/iodine injection system and the SOGs should be significantly greater than the thermal resistance between the nozzle system and its environment. The resistance between the components and their environment is difficult to calculate precisely because certain details are unknown, such as the structural supports that hold the hardware and their resulting conductive heat flow paths. For purposes of these estimates, the thermal resistance to the environment was approximated as being dominated by convective heat transfer to the ambient. The thermal resistance between the nozzle assembly and the SOGs was approximated as being dominated by conductive heat transfer through a shell of silicon that encloses the flow path between the two components. For purposes of the calculation, the overall system was assumed to be a small-scale test laser with a slit nozzle (1 mm nozzle throat width, 1 cm nozzle height). In order for the thermal resistance of the silicon shell to significantly exceed the thermal resistance to ambient, the shell would have to be of order 100 microns thick. This dimension is much too thin for structural stability and robustness. Therefore, the decision was made to create external interfaces to connect the SOGs to macroscale nozzle assemblies.

The integration design employs batch-fabricated SOGs as in the original concept, but the SOG-nozzle interface is oriented at 90 degrees to what was originally envisioned. The simplest way to build scaled-up SOGs is by fabricating groups of them on the same wafer and including monolithic inter-SOG interconnects between them. The next step in scale-up is to laminate additional wafer-level groupings of SOGs onto the first wafer-scale SOG structure, like adding additional floors to a house. The interface to the nozzle then utilizes an o-ring (or gasket) seal between the flat face of a SOG device (in the plane of the wafer) to an external interface piece that includes an o-ring groove. This is conceptually similar to the packaging approach for the initial demonstration SOGs. This allows a given block of SOGs to supply a given height of nozzle with singlet delta oxygen; additional blocks of SOGs may be connected elsewhere along the nozzle in order to supply larger nozzle heights. This interface design rotates the microdevices out of the natural plane of fabrication and enables the interface seal to be made with the very flat surface of the upper wafer. It would be significantly more challenging to make connections out of the side of the block of microSOG chips because the surface roughness would be significantly greater than the sub-micron roughness required to form a good o-ring seal.

Steam generator design

A pumping system based on steam ejectors was designed during the course of the previous HEL-JTO-funded design and modeling study. Here we designed and modeled a steam generator based on hydrogen peroxide decomposition to provide the driving steam for the steam ejectors. The goals were that the steam generators should be compact, should provide high quality, dry steam, and should offer uniform peroxide decomposition in order to minimize the vibration that the steam generators impart to the rest of the laser system.

There were two basic options for the steam generator design. The first is to catalyze the decomposition of hydrogen peroxide through the use of a standard solid (heterogeneous) catalyst, such as silver. The second was to catalyze the decomposition of the peroxide through the use of a liquid (homogeneous) catalyst, such as FeCl_2 or sodium permanganate monohydrate. The liquid catalyst was chosen because it offers a distinct performance advantage over the solid catalyst approach. Solid catalysts are not stable over the long term in the presence of stabilized hydrogen peroxide; the stabilizers “poison” the catalyst, rendering it ineffective. In contrast, the liquid catalysts are not poisoned by the stabilizers; they are vaporized with the rest of the liquid in the system and flow out with the exiting steam, and are constantly replaced from the reactant feeds. The liquid catalyst does have one downside; it adds additional liquid to the system. The complete decomposition and vaporization of peroxide becomes more difficult at higher levels of peroxide dilution, and minimizing parasitic heat loss becomes increasingly important when there is more liquid to be vaporized.

One major challenge of the liquid catalyst was ensuring adequate mixing. If the peroxide is to decompose with good spatial and temporal uniformity, the time scale for mixing between catalyst and peroxide must be less than or equal to the inherent reaction delay of the peroxide in the presence of the catalyst, which is of order 1 ms. If the reaction occurs before the two streams are well-mixed, the resulting decomposition will be spatially and temporally nonuniform, leading to significant system vibration which will then impact the optical functioning of the laser. If the mixing is faster than the reaction, the decomposition will take place with good uniformity, and vibration will be minimized as compared with macroscale steam generators (and as compared with less uniform microscale designs).

Several approaches to enhancing mixing were considered. It is relatively easy to reject diffusive mixing of broad streams of flow based on its long diffusion time. Although injection of alternating layers of peroxide and catalyst would greatly reduce the time scale for diffusive mixing, the length scale of the laminations would need to be on the order of 10 microns for the mixing to be sufficiently rapid. This short length scale would lead to both extreme fabrication challenges and concerns about the reactor’s structural stability in the face of the driving and generated pressures. Neither chaotic micromixers nor cross-flow injection mixing offered sufficiently short time scales. Ultimately, one promising approach was identified and selected: micro jet impingement mixing, in which opposing streams of liquid are injected through injection pores on opposite faces of the reaction chamber, and mixing at the interface is facilitated by the velocities of the incoming flows. Microjet impingement mixing is shown schematically in Figure 1. The sizes of the injection pores must be set to ensure that the catalyst and liquid flows enter with both at the right flow ratio and with equal momenta. To accomplish this, the peroxide

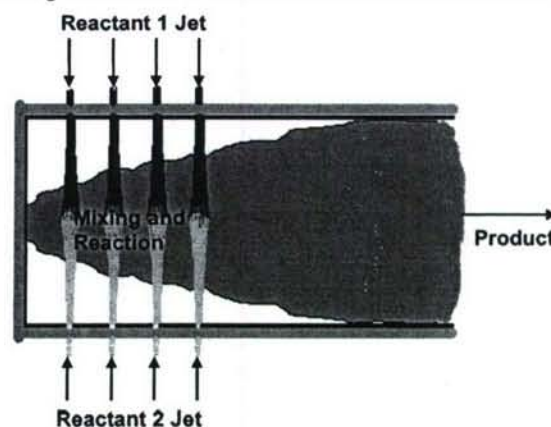


Fig. 1. Schematic diagram of micro jet impingement mixing.

pores are set at 60 microns in diameter and 400 microns long, while the catalyst pores are set at 12 microns in diameter and 100 microns long.

The second major challenge is thermal management. There is a certain amount of energy that is released from the complete decomposition of a given amount of hydrogen peroxide, and this is the energy budget. At the same time, a certain amount of energy is required to convert all of the water in the system (from the peroxide and from the catalyst) into a dry steam, and this is the energy requirement. This imposes two coupled requirements on the system. First, the total fraction of water in the initial system must be small enough to ensure that the energy that's released is sufficient to accelerate the decomposition and vaporize all of the resulting water. Second, the amount of energy lost to the environment through thermal leakage must be small enough to ensure that enough energy remains to convert the liquid to steam.

Two potential solutions were considered. The first, which is reflected in some of the monthly reports, was to provide effective MEMS-scale thermal insulation to prevent heat leakage. The second, which was ultimately chosen for the design, was to design the steam generators such that the ratio of the heat released by the reaction (which is proportional to the total peroxide mass flow rate) to the device's surface area is high enough to minimize the fractional impact of the losses. (The surface area is relevant because it turns out that natural convection from the hot steam generator chip to the environment is the limiting resistance in the thermal leakage path.) If the amount of heat that is released from decomposition is large enough, the heat that is lost through natural convection will not significantly load the system. This second option is preferred because of its greater simplicity. MEMS packaging remains a significant challenge, and radiation-shielded MEMS vacuum packaging is more difficult to implement than most other forms of packaging. This system design is in part made possible by the use of micro-jet impingement mixing, which does not require any microstructuring in the reaction space. The lack of microstructuring makes it easier to maintain large flow rates through the system. This point is addressed further below.

A multi-domain system model was created to guide the design of the system based on these criteria. The model includes thermal leakage (from the fluid in the reaction chamber to the silicon, through the silicon, and from the silicon to the ambient environment), the coupled thermodynamics and kinetics of the decomposing and vaporizing hydrogen peroxide, and the flow functionality of the impingement mixer. The reaction channel itself is treated as a one-dimensional system for the purposes of this analytical model. Using this model, the various system components were sized to operate not only under the design conditions (15 atm pressure with the target mass flow rate of 50 mg/s to drive each chip-scale steam ejector unit), but also under lower pressure conditions that are more conducive to initial testing.

The resulting dimensions included the injection nozzles as described above along with chamber dimensions of 1 mm width, 1 mm depth, and 5 mm length. These channel dimensions are predicted to ensure complete decomposition and vaporization of the liquid at chamber pressures as low as 2 atm, in the presence of losses due to natural convection from the external surface of the device. They also enable operation at higher chamber pressures, including at the design point of 15 atm. In the high pressure case, decomposition and vaporization occur more quickly than at lower pressure, so the latter

part of the reaction chamber flow distance merely provides an opportunity for some of the energy in the flow to be lost. The thermal losses with additional flow length are small, however. The wall thicknesses are sized to avoid rupture due to the internal pressures in the system; a wall thickness of 0.5 mm is found to be more than sufficient to prevent failure in operation, given the small chamber dimensions. The system is implemented in silicon because of its excellent micromachinability (which enables the creation of the most challenging features, the injection nozzles) and because of its thermal robustness, which is necessary for the steam generator's high temperature operation.

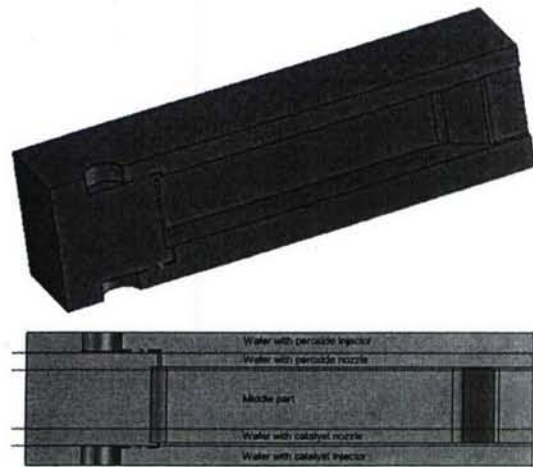


Fig. 2. Schematic cutaway (top) and schematic cross-section (bottom) of the proposed steam generator.

Figure 2 shows the system design. The structure described above is implemented in five silicon wafers. The outermost silicon wafers (wafers 1 and 5) provide external fluid connections through which the peroxide and catalyst enter the system. The next wafers in the stack (wafers 2 and 4) contain the catalyst and peroxide injectors, along with some of the reaction channel thickness. Finally, the center wafer contains the bulk of the reaction channel in which the hydrogen peroxide is decomposed.

Figure 3 plots the temperature of the device as a function of distance along the reaction channel, including thermal leakage. The reactants are assumed to be 88% hydrogen peroxide mixed 85%/15% with a liquid catalyst, for a total peroxide concentration of 75%. The plot on the left is for a chamber pressure of 3 atm, while the plot on the right is for a chamber pressure of 5 atm. The temperature first rises to the point at which both the liquid water and the liquid peroxide become saturated and start to evaporate; once all the

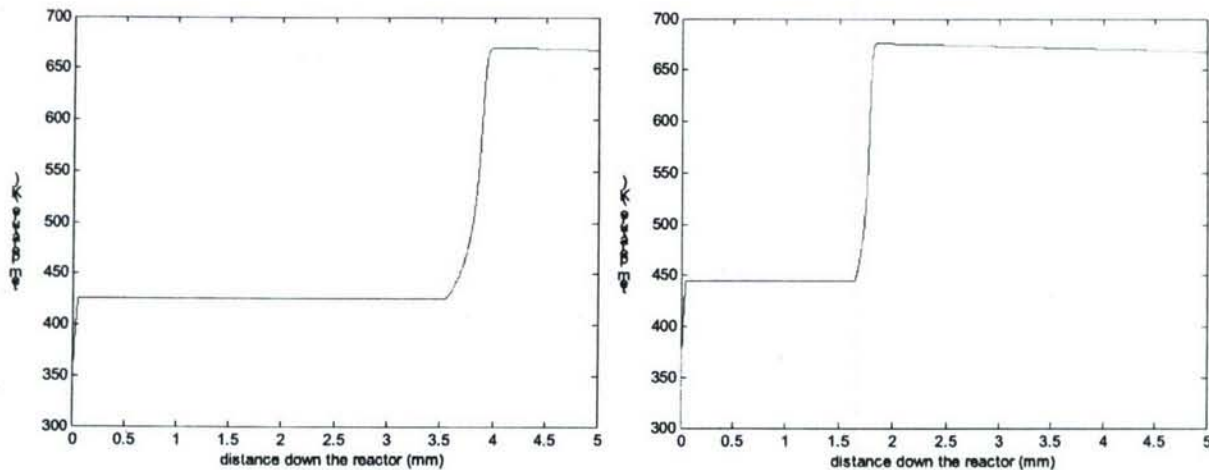


Fig. 3. Left: Temperature vs. distance along the reactor for an 85%/15% mixture of 88% hydrogen peroxide and liquid catalyst at 3 atm chamber pressure. Right: Same temperature vs. distance profile, but at 5 atm.

liquid is fully vaporized, the temperature starts rising again while the remaining gas phase peroxide decomposes. Once the decomposition is complete, there is a slight decline in temperature due to thermal losses as the flow continues. The primary difference between the two plots is the distance at which the peroxide is completely decomposed; the higher pressure system decomposes more quickly. Since the thermal losses after decomposition are relatively modest, it is better to err on the side of a channel that is slightly overlong than one that is a little too short. Figure 4 shows how this temperature profile would change if the thermal leakage from the system were increased. On the left hand side is the temperature profile that would be created if the thermal leakage were 20 times greater than is predicted for the system designed here; on the right

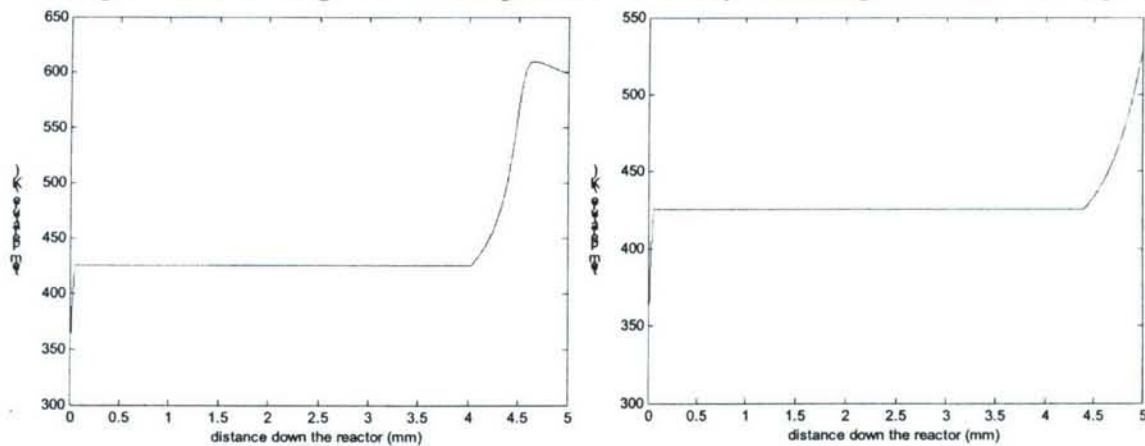


Fig. 4. Left: Temperature vs. distance along the reactor for an 85%/15% mixture of 88% hydrogen peroxide and liquid catalyst at 3 atm chamber pressure, but with 20x the predicted thermal losses. Right: Same temperature vs. distance profile, but with 30x the predicted thermal losses.

side is the temperature profile for a system with 30 times greater thermal leakage. These plots show that the system is not designed at the very edge of its tolerance. The thermal losses may be increased significantly while still decomposing all of the hydrogen peroxide, but there is a level of thermal leakage at which the thermal load abruptly becomes too great, and the decomposition reaction is not completed.

The design concept described above was to minimize thermal leakage by ensuring that the ratio of heat introduced to thermal leakage was sufficiently high. The model results indicate that this design concept can be an effective means of ensuring that a large enough fraction of the released energy goes where it is needed, namely to the decomposition and vaporization of the liquid in the system to produce dry steam. Looking at the present situation in a bit more detail, it is found that the convective heat transfer from the hot fluid to the silicon device structure is extremely effective, as is the conductive heat transfer from the interior of the silicon structure to the exterior of the silicon structure. The heat transfer from the exterior of the silicon structure to the ambient, however, is limited by natural convection in air and by radiation. This is the dominant thermal resistance, so the net result is that the silicon heats up to almost the temperature of the fluid, and then there is a significant temperature drop in temperature from the device to the environment. The predicted successful operation of this device is enabled by a ratio of mass flow rate to outer surface area that is about ten times higher than in previously-built hydrogen peroxide microthrusters that were unable to completely

decompose the input peroxide. In addition, the issue of retaining heat will become progressively less significant as the micro steam generators are scaled up from the single MEMS chip scale to the multi-chip array scale.

Important findings and conclusions

The dominant finding of this program was that MEMS devices do offer significant performance and compactness advantages for COIL, as was suggested by the initial theoretical research. The initial, not-yet-optimized generation of microSOG chips have been shown to have performance that ranges from competitive with to better than that of macroscale SOG systems. There is a clearly-defined path to improving their performance still further, and this path does not introduce any new kinds of technical risks beyond those that have already been introduced in the first phase of this program. In addition, the present work has identified and modeled the path forwards for other parts of the microCOIL system, including interfaces between SOG and nozzle hardware and very promising designs for future MEMS steam generators to drive MEMS steam ejector pumps for more compact pumping for both large and small-scale COIL systems.

Implications for further research

The primary implication of the research done here is that it has set the stage for practical implementation of microCOIL technology for more compact, high-performing systems. The designs, models, and experimental results from this program will be directly applicable to future research in this area.

Bibliography

L.F. Velásquez-García, T.F. Hill, B.A. Wilhite, K.F. Jensen, A.H. Epstein, and C. Livermore, "A MEMS Singlet Oxygen Generator – Part I: Device Fabrication and Proof of Concept Demonstration," accepted for publication in the Journal of Microelectromechanical Systems.

T.F. Hill, L.F. Velásquez-García, B.A. Wilhite, W.T. Rawlins, S. Lee, S.J. Davis, K.F. Jensen, A.H. Epstein, and C. Livermore, "A MEMS Singlet Oxygen Generator – Part II: Experimental Exploration of the Performance Space," accepted for publication in the Journal of Microelectromechanical Systems.

B.A. Wilhite, T.F. Hill, L.F. Velasquez-Garcia, A.H. Epstein, K.F. Jensen, and C. Livermore, "Design of a Silicon-Based Microscale Trickle-Bed System for Singlet-Oxygen Production," submitted to the American Institute of Chemical Engineers Journal.

T.F. Hill, B.A. Wilhite, L.F. Velasquez-Garcia, A.H. Epstein, K.F. Jensen, and C. Livermore, "A MEMS Singlet Oxygen Generator," Proceedings of the 2006 Solid State Sensor, Actuator, and Microsystems Workshop, Hilton Head Island, SC, June 2006, pp. 114-119.

L.F. Velasquez-Garcia, T.F. Hill, B.A. Wilhite, K.F. Jensen, A.H. Epstein, and C. Livermore, "A MEMS Singlet Oxygen Generator for a MEMS Chemical Oxygen Iodine Laser," Proceedings of Power MEMS 2006, Berkeley, CA, November 2006, pp. 117-120.

C. Livermore, T.F. Hill, B.A. Wilhite, L.F. Velasquez-Garcia, A.H. Epstein, K.F. Jensen, W.T. Rawlins, S. Lee, and S. Davis, "Singlet Oxygen Generator on a Chip for MEMS-Based COIL," Proceedings of the LASE 2007 Symposium of SPIE Photonics West, San Jose, CA, January 2007.

A MEMS Singlet Oxygen Generator – Part I: Device Fabrication and Proof of Concept Demonstration

Luis F. Velásquez-García¹, Tyrone F. Hill¹, Benjamin A. Wilhite², Klavs F. Jensen¹, Alan H. Epstein¹, and Carol Livermore¹

¹ Massachusetts Institute of Technology, Cambridge, MA 02139 USA

² Department of Chemical Engineering, University of Connecticut, Storrs, CT 06269 USA

Corresponding Author:

Luis Fernando Velásquez-García, Massachusetts Institute of Technology
77 Massachusetts Avenue Building 39-657 Cambridge, MA 02139 USA
Phone (617) 2530730 FAX (617) 253 0062lfvelasq@mit.edu

Abstract— This paper reports the design, fabrication, and proof of concept demonstration of a singlet oxygen generator (SOG) that operates on the microscale. The micro singlet oxygen generator (μ SOG) chip is implemented in a three-wafer stack using deep reactive ion etching (DRIE) and wafer bonding as key technologies. The device creates singlet delta oxygen ($O_2(a)$) in an array of packed bed reaction channels fed by inlet manifolds with pressure drop channels that ballast the flow. An integrated capillary array separates the liquid and gas by-products, and a microscale heat exchanger removes excess heat of reaction. The fabrication process and package are designed to minimize collisional losses and wall deactivation of $O_2(a)$. The design, fabrication, and package of the device are documented. Proof of concept demonstration of the device is given by optical emission measurements of the spontaneous decay of the $O_2(a)$ molecule into its triplet state, and by the observation of the emission from dimol pairs of $O_2(a)$ molecules.

Index Terms— singlet oxygen, Chemical Oxygen Iodine Laser (COIL), microfluidics, DRIE.

I. INTRODUCTION

AN oxygen molecule has four electrons in its outer p-subshell. The $O_2(X^3\Sigma^-)$ state (also known as triplet oxygen, ground state oxygen, or $O_2(X)$) has three electrons in one spin state and the fourth in the other, while the $O_2(a^1\Delta_g)$ state (also known as singlet delta oxygen, spin-excited molecular oxygen, or $O_2(a)$) has two electrons in each of the 'spin up' and 'spin down' configurations [1]. Singlet delta oxygen is valuable as a reactant for organic synthesis and as an energy carrier for the Chemical Oxygen-Iodine Laser (COIL). COIL is attractive for applications requiring very high average powers, light weight, and overall system compactness, and it provides a promising alternative to CO_2 lasers for industrial machining. A lower emission wavelength (1.315 μm vs. 10.6 μm for CO_2) results in more efficient coupling to metals, reducing the power needed for welding and cutting. The lower wavelength also results in smaller spot size, so COIL systems offer higher machining resolution, and enables fiber-optic beam delivery for greater flexibility. In a flowing gas laser such as COIL, the waste heat flows out with the exhaust gas stream; therefore, the laser's average power is not limited by cooling, as are most high-energy solid-state lasers.

COIL systems are chemical lasers in which iodine acts as the lasing species [2]. Population inversion of the gain medium is sustained by collisions between ground state iodine atoms ($I(^2P_{3/2})$) and $O_2(a)$, *i.e.*, COIL is a two-species two-level laser where the near resonance between the $O_2(a)$ state and the $I(^2P_{1/2})$ state of atomic iodine makes $O_2(a)$ an ideal pumping source for laser emission. $O_2(a)$ is metastable and may be synthesized through the highly exothermic multiphase reaction of gaseous Cl_2 with an aqueous mixture of concentrated H_2O_2 and KOH , commonly referred to as basic hydrogen peroxide (BHP). Usually the reactant Cl_2 is buffered with a non-reacting gas such as helium. The laser application of $O_2(a)$ generation requires a high yield to sustain laser emission, where yield is defined as the fraction of product oxygen in the $O_2(a)$ state. The laser application also requires high conversion of Cl_2 to $O_2(a)$, which is achieved by effective mixing of the gas and liquid reagents.

Once produced, $O_2(a)$ may deactivate into ground-state oxygen by gas-phase collisions with water vapor, with other oxygen or helium molecules, or by heterogeneous collisions with solid surfaces. Thus, the

reactor design must provide large surface areas for initial $O_2(a)$ generation, followed by rapid separation of gas and liquid phases. The output gas must be maintained at low pressures (~ 50 -250 torr) to minimize homogeneous deactivation, and the reactor must be maintained at low temperatures ($< 0^\circ C$) to minimize water vaporization and the resulting iodine deactivation that water vapor would cause in a complete COIL system. The present work shows that the challenges of high yield, thermal management, and product separation can be successfully addressed by a MEMS-based approach to $O_2(a)$ generation.

Generation of $O_2(a)$ for COIL was first demonstrated by McDermott et al. in 1978 [2]. A 6000 sccm flow of Cl_2 gas was bubbled through an aqueous solution of 90% wt H_2O_2 and 6M NaOH in a dry ice and ethanol-cooled sparger, producing $O_2(a)$. A cold trap removed moisture and unreacted chlorine from the product gas before mixing it with I_2 and Ar. The $O_2(a)$ yield was approximately 40%. McDermott's method was successful, but it is limited by significant deactivation of the $O_2(a)$ gas before its separation from the liquid phase. Subsequent SOG configurations have employed either jets of BHP droplets mixed with Cl_2 [3] or rotating-disk configurations [4]. In rotating-disk SOGs, a film of BHP on the surface of a rotating wheel is exposed to a Cl_2 stream, resulting in $O_2(a)$ production at the interface. However, these configurations also have limitations: a small gas-liquid contact area for rotary SOGs, and a large volume for the jet configuration.

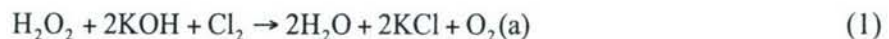
Modeling suggests that a COIL utilizing MEMS components has key advantages as compared with fully macroscale implementations. These advantages include smaller hardware size for the same power level, more efficient reactant utilization, gravity independence and feasible batch manufacturing [5]. The present work demonstrates successful generation of $O_2(a)$ in a MEMS-based SOG chip, and it suggests that arrays of MEMS-based SOGs can address the shortcomings of macroscale SOG designs, thus providing higher yields and greater $O_2(a)$ flow per unit reactor volume. The advantages of the MEMS-based SOG reported here are enabled by a set of key device characteristics, which may be summarized as follows. First, the MEMS-based SOG has a large surface-to-volume ratio, which enhances reactant mixing and facilitates excess heat removal as demonstrated in previous gas-liquid reactions in microreactors [6]. Second, the

device has no moving parts, which increases the robustness and reliability of the system. Third, the $O_2(a)$ travels a shorter distance from the point of formation to the point of utilization in the microdevice, thus reducing $O_2(a)$ losses. Fourth, the integration of a microfabricated heat exchanger in the microSOG chip simplifies the overall COIL system. Fifth, capillary gas-liquid separator permits orientation independent operation or even operation in zero g. The final enabling characteristic is the ability to manufacture COIL components efficiently and scalably through batch fabrication.

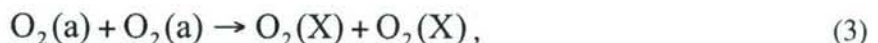
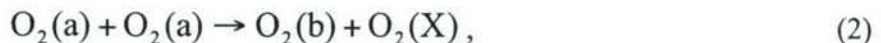
In Section II this paper presents a conceptual discussion of SOG operation and details of the device structure. In section III the process flow and fabrication characterization of the device are documented. In section IV, the package is described. In Section V, experimental results that confirm the production of singlet delta oxygen are presented as a proof of concept demonstration.

II. SOG CONCEPT AND STRUCTURE

SOGs typically produce $O_2(a)$ by mixing gaseous chlorine and BHP, according to the overall chemical reaction



Often the Cl_2 is mixed with a buffer gas (He or N_2) in order to raise the total pressure of the stream. After generation, $O_2(a)$ may be deactivated by several mechanisms, the most prominent being collisions between $O_2(a)$ molecules,



where $O_2(b)$ refers to the excited $O_2(b^1\Sigma_g^+)$ state of oxygen, and wall interactions



The reaction rate is limited by (and the subsequent $O_2(a)$ deactivation depends on) the transport of gaseous chlorine into and gaseous $O_2(a)$ out of the liquid phase. Therefore, maximizing the gas-liquid contact area is critical both to promote the reaction and to obtain high $O_2(a)$ yield.

Figure 1 shows a schematic of the μ SOG chip. The system is composed of 32 packed bed reaction channels that are fed in parallel with the gas and liquid reactants using bifurcating manifolds. The reactants mix inside the reactor beds. Chlorine diffuses into the BHP, where it reacts to produce $O_2(a)$. The $O_2(a)$ then diffuses back out into the flow of gas. The packed bed has a staggered configuration that increases mixing of the laminar reactant flows by increasing the vorticity without moving parts. Pressure-drop channels located upstream of each packed bed equalize flows among the reaction channels of the microdevice, thus acting as hydraulic impedances that ballast the reactor array. The reactor design builds upon and extends previous gas-liquid microreactors for oxidizing organic liquids with highly reactive ozone gas [7]. The reaction channels flow into a gas-liquid separator in which an array of capillaries removes the liquid by-products from the gaseous output stream. The $O_2(a)$ is then collected and routed to the chip's gas outlet port. A previous analytical study evaluated the feasibility of microscale $O_2(a)$ generation [5]. Using standard MATLAB numerical simulation techniques and estimates of physical parameters, key SOG dimensions and operating points were optimized. The dimensions employed in the present μ SOG mask design were largely based on the results and conclusions of this study. The optimum device dimensions from the study (given the estimated parameters) included a reaction channel 0.516 cm long, 0.25 cm long pressure drop channels, a 1-cm section for gas and liquid flow distribution, and an optimal total gas (helium plus chlorine) flow rate of 175 sccm at a 3:1 He:Cl₂ ratio.

Figure 2 is a photograph of a completed μ SOG chip made as a three-wafer stack. Figure 3 (A) shows a simplified 3D model of the μ SOG. The top wafer is Pyrex[®] and seals the flow channels while providing optical access to the reaction channels and separator. The middle wafer is silicon and contains the distribution manifold for the liquid reactants, the pressure drop channels, the capillary separator, and the packed bed reaction channels. The pressure drop channels have a width of 25 μ m and a depth of 20 \pm 1 μ m. The BHP pressure drop channels are 2750 \pm 50 μ m long, and the gas pressure drop channels are 2428 \pm 35 μ m long. In both cases the aspect ratio is larger than 100, and the pressure drop channels' hydraulic diameter is about 22 μ m. The reaction channels are each 6.1 mm long, 630 μ m wide, and 300 μ m high; the

length was increased above the optimized length given above to ensure adequate residence time for complete reaction of the chlorine. Each reactor packed bed contains a hexagonal array of columns with 360 μm height, 70 μm diameter, and 90 μm pitch. This post-bed configuration is a two-dimensional approximation of a conventional packed-bed, providing reduced pressure drops while eliminating the need for subsequent packing of reaction channels. The separator is composed of a hexagonal array of more than 7,000 capillary holes with 265 μm length, 25 μm diameter and 90 μm pitch that relies on surface tension effects to separate the two-phase exit stream [8]. There is a wide range of separator dimensions that is expected to be able to separate the exit stream; the set of dimensions used here ensures that the separator's flow capacity exceeds the anticipated flow rates. The hexagonal packing maximizes the feature density per unit area. Figure 3 (B) shows a cross section of the middle wafer. The bottom wafer is silicon and contains the distribution manifold for the gas reactants, the heat exchanger, and a port for an external thermocouple. The heat exchanger removes excess heat generated during the reaction, enabling low-temperature operation. The heat exchanger is made of 19 cooling channels, each of which is 23.9 mm long, 300 μm wide and 300 μm deep. The BHP and Cl_2 inlets are 1 mm in diameter; all other inlet and outlet connections are 2 mm in diameter. The die size was set at 3.6 cm x 2.8 cm to accommodate packaging. Figure 4 (A) shows a photograph of a microfabricated middle wafer die, and Figure 4 (B) shows a photograph of a microfabricated bottom wafer die. All ports are on the back of the three-wafer stack to facilitate packaging and testing.

III. FABRICATION

The fabrication process for the μSOG is intended to address the need for uniform flow rates across the chip (particularly reactor bed uniformity and capillary separator uniformity) and chemical inertness of the chip to BHP, chlorine, and singlet delta oxygen. Described broadly, the process flow relies heavily on DRIE, fusion bonding, and anodic bonding to build the device and uses a conformal layer of LPCVD silicon-rich nitride to protect the bulk silicon from the reactants and products. However, the successful

creation of the μ SOG chip depends critically on the details of the process flow, which ensure that three key requirements are met. First, different types of high aspect ratio features (posts and pores) must be created in the same process steps as features that have vastly different aspect ratios and in plane dimensions. Second, the pattern definition and transfer techniques must permit wafer processing even after the removal of significant portions of the bulk silicon. Third, the assembly procedures must ensure that the silicon is entirely covered by a defect-free, chemically inert coating of silicon nitride in order to prevent the dissolution of the μ SOG chip upon exposure to BHP. The process flow for the μ SOG, including the enabling details, is described in subsection A; the fabrication characterization is described in subsection B.

A. Process Flow

The device is made of three 6-inch wafers: one Pyrex[®] wafer 2 mm thick (Bullen Ultrasonics, Eaton, OH), and two double-side-polished (DSP) p-Si <100> wafers 625 \pm 20 μ m thick (Silicon Quest, San Jose, CA). The Pyrex[®] wafer is 2 mm thick for greater stiffness and higher pressure capability, but devices with Pyrex[®] wafers 625 μ m thick were also successfully fabricated and tested. The following is the process flow for the μ SOG:

- 1) **Middle Wafer.** Figure 5 shows a schematic of the process flow for the middle wafer. The middle wafer starts as a lightly doped DSP p-Si 6-inch wafer 625 μ m thick (a). First, 0.5 μ m of thermal silicon oxide is grown on the wafer, and alignment marks are transferred to front and back (b). The silicon oxide film protects the wafer surfaces for later fusion bonding. A 0.5 μ m thick silicon-rich LPCVD silicon nitride film is deposited to serve as a diffusion barrier for the future oxidation in step (f). If the nitride layer were omitted, any nonuniformities in the thickness of the oxide brought on by processing could be amplified by the subsequent oxidation, compromising the flatness of the bonding surface. The silicon-rich silicon nitride film is stripped from the wafer's top surface using an SF₆-based recipe on a LAM 490-B RIE plasma etcher (c). The wafer top then receives a nested mask to form the deep features (reaction channels, the liquid reactants manifold, and capillary separator region) and the shallow

features (pressure drop channels). The features to be patterned in the oxide mask layer (liquid distribution network, pressure drop channels, reaction channels without the columns, and the region that will contain the capillary separator) are patterned in 10 μm thick AZ P4620 resist on the top of the wafer with contact photolithography. The back side of the wafer is protected with photoresist, and the patterns are transferred to the oxide with sonicated BOE. The photoresist is stripped with piranha and oxygen plasma (d). The features to be patterned in the resist mask layer (reaction channels and capillary separator region) are transferred to a 10 μm thick AZ P4620 photoresist layer. Using the patterned resist as a mask, an optimized DRIE etching step etches 340 μm of silicon anisotropically to form the packed bed reaction channels and define the thickness of the remaining silicon where the capillary pores of the separator will ultimately be formed. The resist mask is stripped with oxygen plasma, and the silicon exposed by the oxide mask is etched with DRIE to pattern the pressure drop channels, pattern the liquid inlet manifold, and finish etching the packed bed reaction channels to a total depth of 360 μm (e). The wafer is RCA cleaned and oxidized to grow 0.5 μm of silicon oxide on all exposed silicon surfaces. The silicon oxide protects the posts from collateral damage during future DRIE processing (f). The silicon nitride is stripped using a hot phosphoric acid mixture at 165 $^{\circ}\text{C}$ (g). The wafer is then flipped over and attached to die saw tape to provide a removable, sealable surface to the spin coater's vacuum chuck. The bottom of the wafer receives a 10 μm thick AZ P4620 photoresist film with the layout of the chip ports and the capillary separator pores. The exposed oxide is removed in BOE, and the wafer is etched with DRIE to form the capillary separator (h). The wafer is dismounted, and the photoresist is stripped using piranha and oxygen plasma.

- 2) **Bottom Wafer.** Figure 6 shows a schematic of the process flow for the bottom wafer. The bottom wafer starts as a lightly doped DSP p-Si 6-inch wafer 625 μm thick (a). First, 0.5 μm of thermal silicon oxide is grown on the wafer, and alignment marks are transferred to front and back (b). The silicon oxide film protects the wafer surfaces for later fusion bonding. Next, a 4 μm thick PECVD silicon oxide is deposited on both sides of the wafer, and the films are annealed for one hour at 950 $^{\circ}\text{C}$ in nitrogen (c).

After annealing, both sides of the wafer are coated with 10 μm thick AZ P4620 photoresist. The heat exchanger and gas inlet manifold are patterned in the front side resist, and the chip ports (liquid and gas inlets and exits, including the coolant ports) are patterned in the back side resist. The exposed oxide on both sides is anisotropically etched with a cycled CHF_3 C_2F_4 -based RIE plasma etch to form DRIE etch masks (d). The photoresist is stripped with piranha followed by oxygen plasma. The heat exchanger and gas inlet network are etched to a total depth of 315 μm with DRIE (e). The wafer is flipped over, mounted on a quartz handle wafer, and etched with DRIE to pattern the chip ports (f). The wafer is then dismounted from the quartz handle wafer.

3) **Final Processing:** Figure 7 shows a schematic of the process flow that completes the device. The completed middle and bottom wafers are immersed in 49% HF to strip the silicon oxide films and are then RCA cleaned, contacted, pressed with 2500 N of force for twelve hours, and fusion bonded at 1050 $^{\circ}\text{C}$ for one hour in nitrogen (a). The silicon wafer stack then goes directly to the LPCVD reactor to be coated with a 0.4 μm -thick, conformal, silicon-rich silicon nitride film (b). The silicon-rich silicon nitride film acts like a glove that protects the silicon substrate from the reactants and products, in particular from the BHP. The stack is anodically bonded to an unpatterned Pyrex[®] wafer for ten minutes, using 1000 V_{DC} , a compressive force of 1000 N, and a bonding temperature of 350 $^{\circ}\text{C}$ (c). The wafer stack is then die-sawed using a glass blade 250 μm thick. Eight μSOG chips are obtained from each wafer stack, and near 100% yield was achieved in all batches.

B. Fabrication characterization

Figure 8 is a set of SEM pictures that show cross sections of one of the μSOG chips. Key features such as the reactor packed beds, the cooling channels, the liquid by-products collector tray, and the capillary separator can be identified. Figures 9 (A) and 9 (B) are SEM micrographs that show the structure of a reactor packed bed channel. The as-fabricated columns have a diameter of 70 μm , an aspect ratio of 5.5, and 90 μm pitch. The roots of the columns have large radii to avoid fracture. Figures 9 (C) and 9 (D) are

SEM micrographs that illustrate the capillary separator structure. The separator consists of 25 μm diameter capillary holes on a 90 μm pitch. The DRIE recipe that patterned the packed bed is insensitive to microloading, *i.e.*, the etch rate of the columns is the same as the etch rate of the open area where the separator is formed. Figure 10 is a set of IR pictures that show the structure of the μSOG , including the reactant manifolds, the reactant injector structure (the gaseous reactant flow is surrounded by the liquid reactant flow at the entrance to the reaction channels), the reactor packed bed (the reactor is right on top of the cooling channels of the heat exchanger), the heat exchanger structure (there is a set of ribs to stiffen to the heat exchanger as well as to increase the surface area for better heat transfer), and the separator.

IV. PACKAGE

BHP and chlorine are very reactive, and the μSOG package materials must be selected for resistance to these chemicals (including resistance to chlorine in the presence of humidity). The μSOG package must also minimize deactivation of $\text{O}_2(\text{a})$ in order to maximize yield. To meet these requirements, connections to the μSOG chip were made with 1/8" and 1/16" Teflon tubing, except for the gas outlet, which was connected directly to a quartz optical cell for $\text{O}_2(\text{a})$ detection. Glass is ideal for the gas outlet because it permits optical access and has a $\text{O}_2(\text{a})$ wall deactivation coefficient that is half that of the best metals and an order of magnitude lower than that of Teflon® and therefore minimizes surface deactivation of $\text{O}_2(\text{a})$ [9]. Minimizing $\text{O}_2(\text{a})$ deactivation also requires that the gas outlet path have low enough surface to volume ratio to ensure that wall deactivation is not a dominant $\text{O}_2(\text{a})$ loss mechanism, while still having a short enough residence time to ensure that homogeneous deactivation of $\text{O}_2(\text{a})$ is as low as possible; the 2 mm diameter entrance to the quartz optical cell is a good compromise between these two competing requirements. The package must also seal to the chip's ports for internal chip pressures ranging from vacuum to several atmospheres. For the proof of concept demonstration shown in this paper, the connections were simply epoxied to the chip. For the systematic exploration of the performance space shown in the Part II paper [10], the connections were made by means of a chemically-resistant, readily-

machinable, and stiff Tefzel® package that seals to the chip with chemically-resistant Simriz® and Kalrez® o-rings and gaskets. The package comprises a chuck (with o-ring ports to interface to the chip) that is clamped with Tefzel® screws to a plate that includes an opening to permit optical access to the chip (Figure 11). Finger-tight Tefzel® fittings (Bio-Chem Valve Inc., Boonton, NJ) connect to the tubing to allow easy package reassembly.

V. EXPERIMENTAL RESULTS

Prior to operation with Cl_2 and BHP, the μSOG 's flow functionality was investigated using He and distilled (DI) water. The most important functionalities are (i) the gas-liquid hydrodynamics in the packed-bed reaction channels, and (ii) the extent of liquid removal by the capillary separator. Both are critical to device performance, as effective mixing directly affects the rate of $\text{O}_2(\text{a})$ generation, and complete removal of the liquid by-products is necessary for the μSOG 's use in a complete COIL system. In addition, although microscale packed bed reaction channels and capillary separation have been demonstrated before (see for example [6-8]), differences in the design and functionality of this system necessitate the flow characterizations described here. One key difference is in the operating point of the capillary separator, which must operate with low pressures of 50 – 250 Torr on the inlet side of the capillary separator instead of with atmospheric pressure at the inlet as in [8]. A second key difference is the integration of the elements described here into a complete system.

Two unique modes of gas-liquid flow were observed in the present device. At low gas flow rates (below about 50 sccm), a steady flow pattern is observed in which the liquid flows continuously as a wetted film along the channel walls and partially wets the posts, while the gas flows through the remaining voids. Once developed, gas-liquid interfaces in this regime remain stationary with the majority of the reactor volume being occupied by gas, resulting in limited interaction between the two phases. At higher gas flow rates, the gas-liquid interface was observed to fluctuate rapidly, resulting in an unsteady liquid flow, which may enhance gas-liquid mixing. Steady flow was observed under all reacting conditions investigated.

The capillary separator's performance was also investigated using He and DI water. As far as the authors are aware, this is the first reported demonstration of separation of a liquid-gas mixture below atmospheric pressure using the capillary micropore concept [8]. The separator operates on the basis of liquid capillary pressure; during operation the pores are filled with liquid, which is driven through the holes and out of the chip by an externally-imposed pressure drop. The capillary pressure of the liquid film resists flow of gas through these same holes, thus effectively separating the two phases. A linear relationship was observed between the plenum pressure (the pressure at the phase separation point) and the minimum applied pressure drop across the capillary pores necessary to ensure phase separation. Figure 12 illustrates this relationship for three different liquid delivery pressures corresponding to three different liquid flow rates. No relationship between the liquid flow rate and the required pressure drop was observed, most likely because the liquid flow rates are significantly below the separator's designed capacity. Detailed models of the separator's performance are relevant for the quantitative analysis of the μ SOG's performance across its operating space, and they are described in the Part II paper [10].

Using the results of the water and He experiments, the chip was operated with BHP and chlorine flows to generate $O_2(a)$ using steady BHP flow and typically one minute long chlorine pulses. It is relatively straightforward to confirm $O_2(a)$ generation, but quantitatively measuring the yield is a significant challenge. A detailed account of the quantitative measurement of the $O_2(a)$ is presented in the Part II paper [10]. Three measurement techniques were used to verify qualitatively the generation of $O_2(a)$. The first approach relies on the fact that two $O_2(a)$ molecules can collide to form a dimol. The subsequent dimol emission appears as a red glow (Figure 13). In the second approach (Figure 14), an optical system monitors the spontaneous decay of the $O_2(a)$ molecule to its ground state, $O_2(X)$, and the resulting emission of a photon. The chip was operated under the experimental conditions described in Table 1 to demonstrate the proof of concept of the μ SOG. Figure 15 shows a typical spectral measurement. The spectrum is centered around the 1.268 μm wavelength of the $O_2(a) - O_2(X)$ emission. The IR spectral data in Figure 15 have a signal-to-noise-ratio better than 12. Finally, the third approach consisted of analyzing the gas products by

mass spectrometry. A commercial mass spectrometer was used to measure the total molar fraction of oxygen (in all states of excitation combined), and in particular to capture the rise in the oxygen molar fraction above the background signal when chlorine is flowing. Figure 16 shows the time variation of the oxygen molar fraction during two successive chlorine pulses. The rise in O_2 mole fraction correlates with the chlorine pulses and is clear evidence of oxygen production from the chip.

CONCLUSIONS

The microfabrication and proof of concept demonstration of a MEMS-based singlet oxygen generator have been shown. The fabrication process for the μ SOG is driven by the need to meet the device's stringent specifications in geometry, device uniformity, and chemical compatibility. This process has been shown to be robust, with typical yields of about 100%; the high repeatability offers the potential for future integration of arrays of μ SOG chips to form singlet oxygen generating hardware that combines the total capacity of a macroscale SOG with the performance advantages of a MEMS-based system. The μ SOG's generation of singlet delta oxygen has been qualitatively confirmed by the three complementary observations of visible dimol emission, emission of 1268 nm photons as the singlet delta molecule spontaneously decays to the ground state, and increases in total oxygen in the output flow, as measured by mass spectrometry, that correlate with the chlorine feed.

ACKNOWLEDGMENTS

The authors acknowledge J. Letendre for his expertise in building the experimental apparatus and D. Park for help with images of the SOG and optics. Additionally, the microfabrication expertise of Dr. Hanqing Li was critical to the success of the project. The microfabrication was done in the Microsystems Technology Laboratories at MIT. The Tactical Technology Office at DARPA, the Missile Defense Agency (MDA), and the Air Force Research Laboratory (AFRL) generously provided funding for this research (DARPA Order No. T171/00, Program Code: 4G10; Issued by DARPA/CMO under Contract No. MDA972-04-C-0140). The views and conclusions contained in this document are those of the authors and should not be

interpreted as representing the official policies, either expressed or implied, of the Defense Advanced Research Projects Agency or the U.S. Government.

REFERENCES

- [1] H. H. Wasserman and R. W. Murray, *Singlet Oxygen*. New York, New York: Academic Press Inc., 1979, p. 25.
- [2] W. E. McDermott et al., "An electronic transition chemical laser," *Appl. Phys. Lett.*, vol. 32 (8), 1978.
- [3] S. Yoshida, H. Saito, and T. Fujioka, "New singlet oxygen generator for chemical oxygen-iodine lasers," *Appl. Phys. Lett.*, 49 (18), 1986.
- [4] K. R. Kendrick et al., "Determination of Singlet-Oxygen Generator Efficiency on a 10-kW Class Supersonic Chemical Oxygen-Iodine Laser (RADICL)" *IEEE J. Quantum Electronics*, vol. 35(12), pp. 1759-1764, 1999.
- [5] B. A. Wilhite et al., "Design of a MEMS-Based microChemical Oxygen-Iodine Laser (μ COIL) System," *IEEE J. Quantum Electronics*, vol. 40 (8), pp. 1041-1055, 2004.
- [6] M. W. Losey et al., "Microfabricated Multiphase Packed-Bed Reactors: Characterization of Mass Transfer and Reactions," *Ind. Eng. Chem. Res.* 2001, vol. 40, pp. 2555-2562.
- [7] Y. Wada, M. A. Schmidt, and K. Jensen, "Flow Distribution and Ozonolysis in Gas – Liquid Multichannel Microreactors", *Ind. Eng. Chem. Res.* Vol 45, pp 8036 – 8042, 2006.
- [8] A. Günther, et al., "Micromixing of Miscible Liquids in Segmented Gas-Liquid Flow," *Langmuir*, vol. 21, pp.1547-1555, 2005.
- [9] K. A. Truesdell, S. E. Lamberson, G. D. Hager, "Phillips Laboratory COIL Technology Overview," AIAA 92-3003.
- [10] T. F. Hill, L. F. Velasquez-Garcia, B. A. Wilhite, K. F. Jensen, A. H. Epstein, C. Livermore, "A MEMS Singlet Oxygen Generator – Part II: Experimental Exploration of the Performance Space", submitted to the *Journal of Microelectromechanical Systems*.

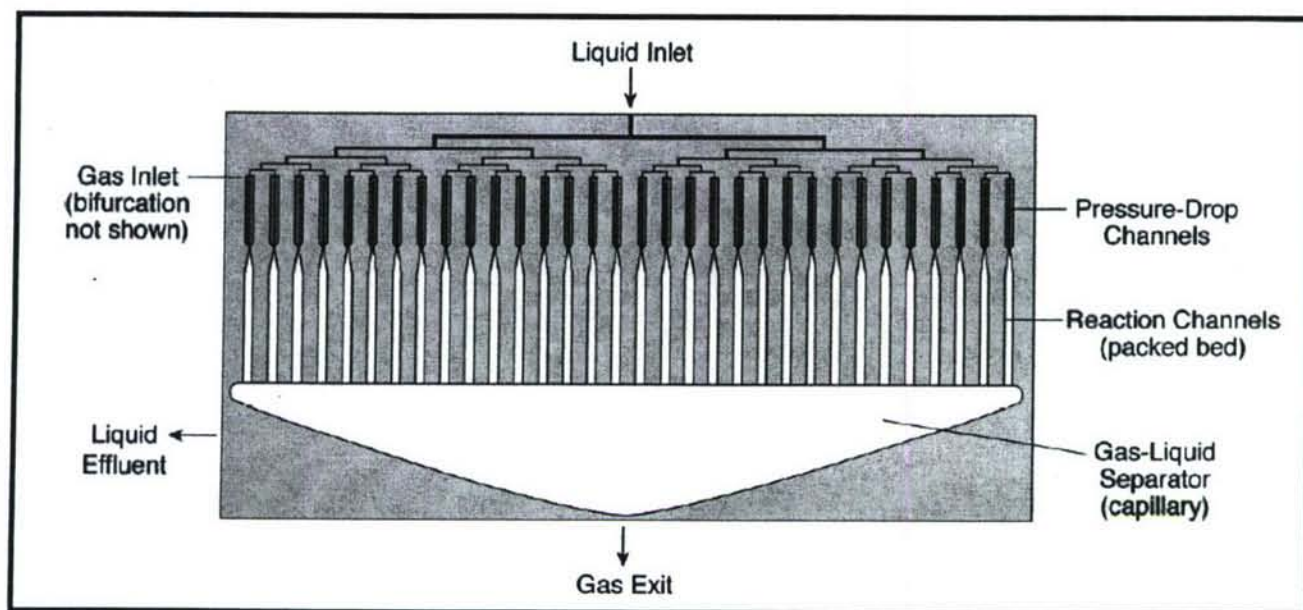


Figure 1. Schematic of the μ SOG. The system also has a micro-fabricated heat exchanger (not shown) directly below the reaction channels to control the chip temperature.

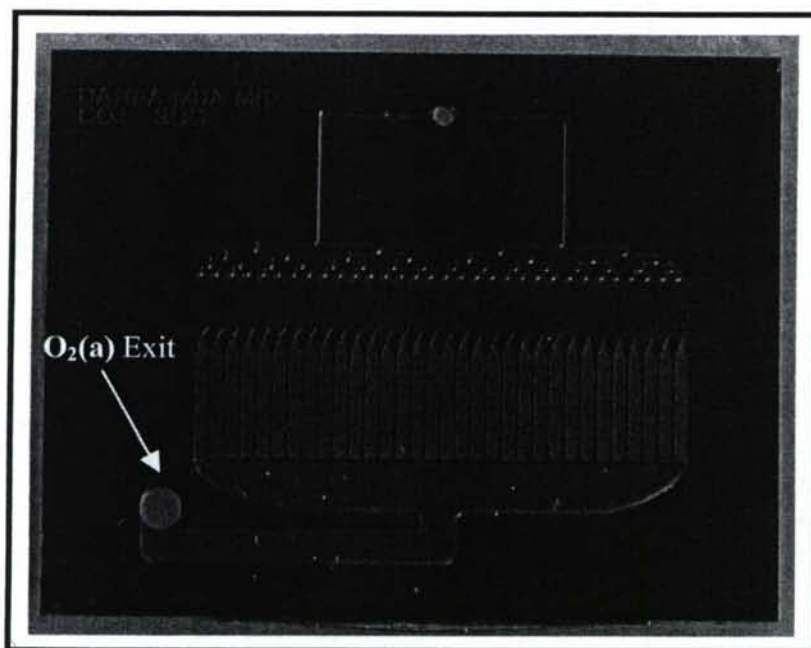


Figure 2. Photograph of a completed μ SOG chip, showing similar features to those represented in the schematic of Figure 1. The singlet delta oxygen exit port is at the lower left hand side of the chip.

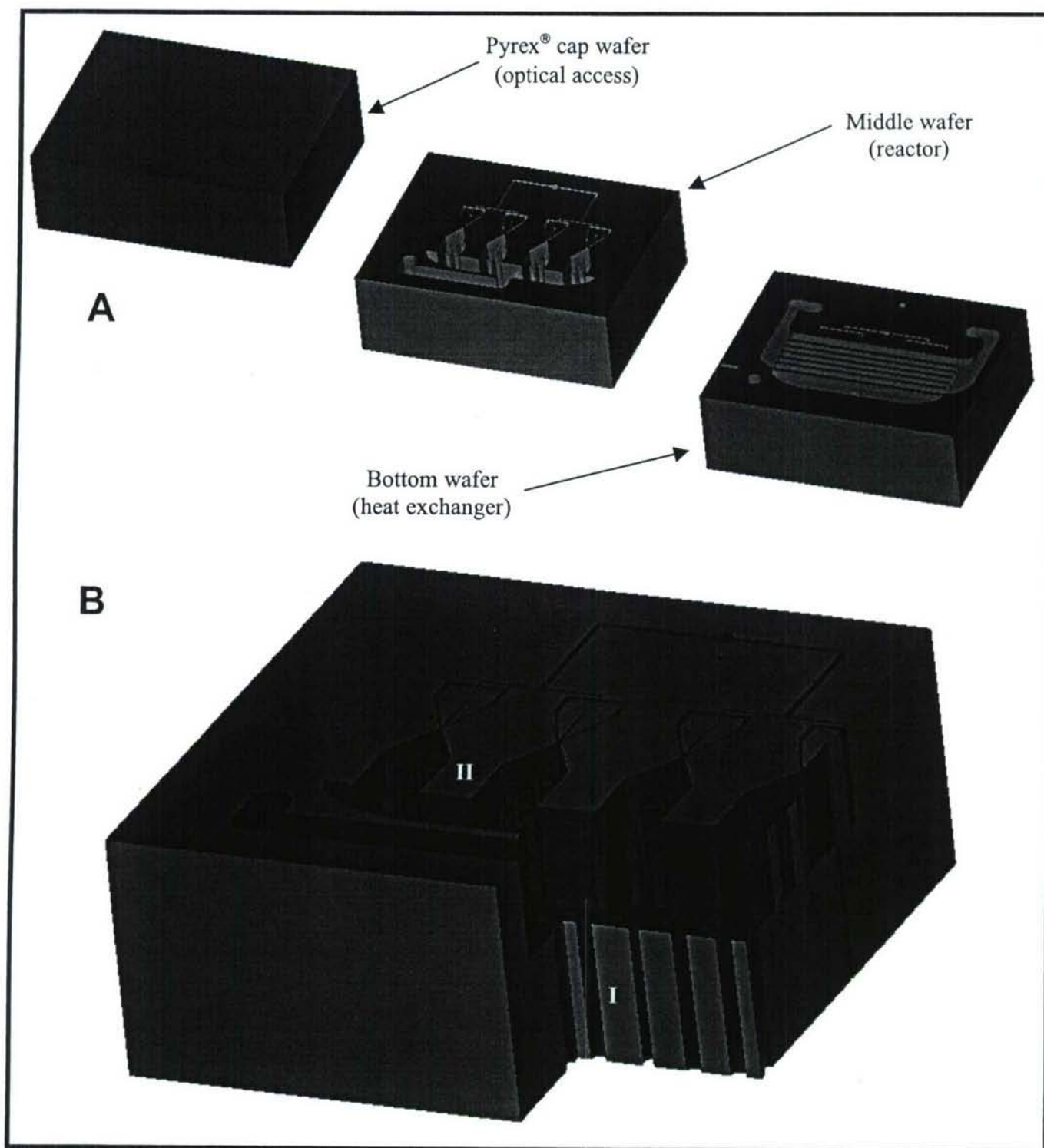


Figure 3. Simplified 3D model of the μ SOG chip with its constitutive layers (A), and Cross-section of the middle wafer (B). The middle wafer contains both the capillary separator (I) and the packed bed reaction channels (II).

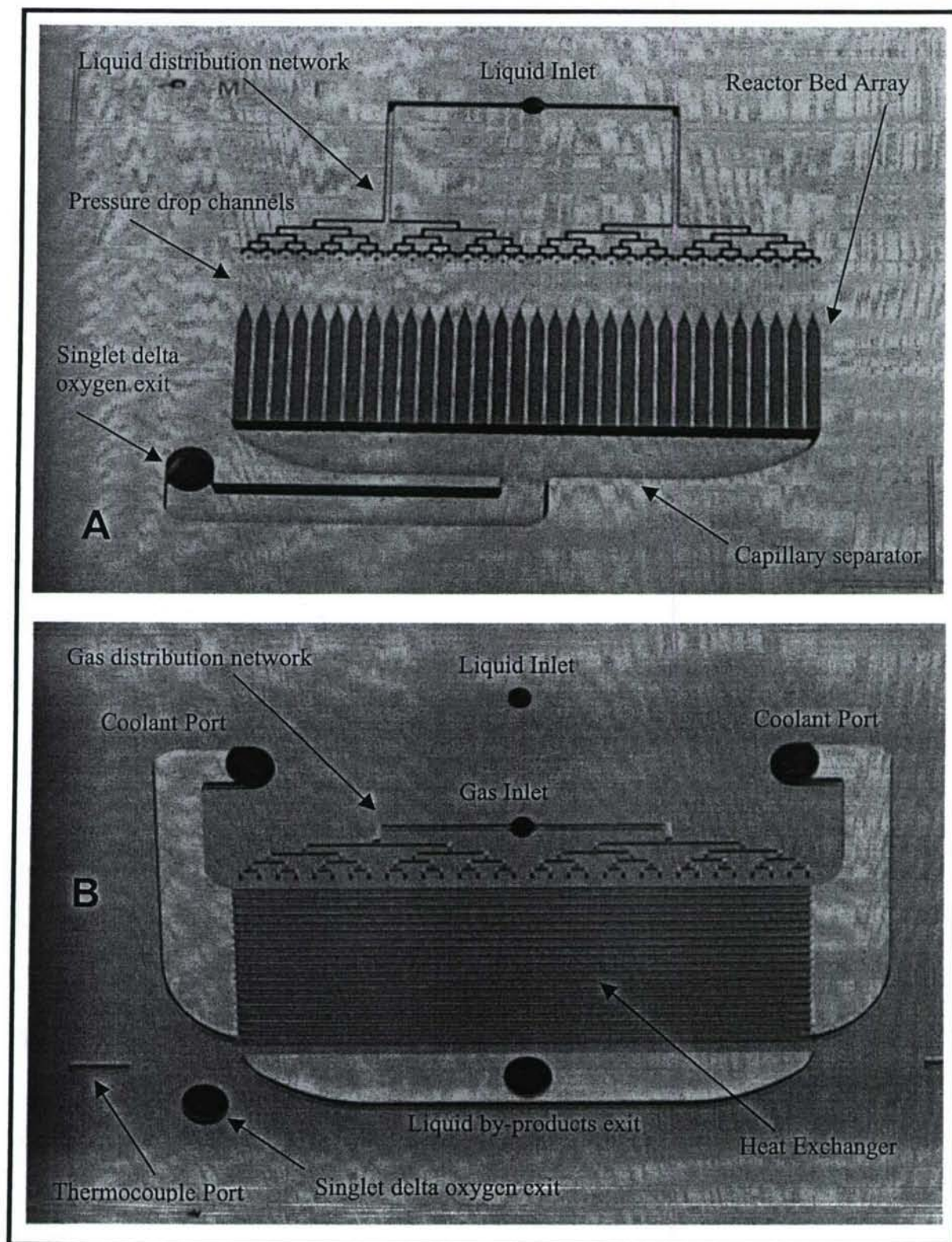


Figure 4. Photographs of the middle wafer (A), and the bottom wafer (B) of a μ SOG chip.

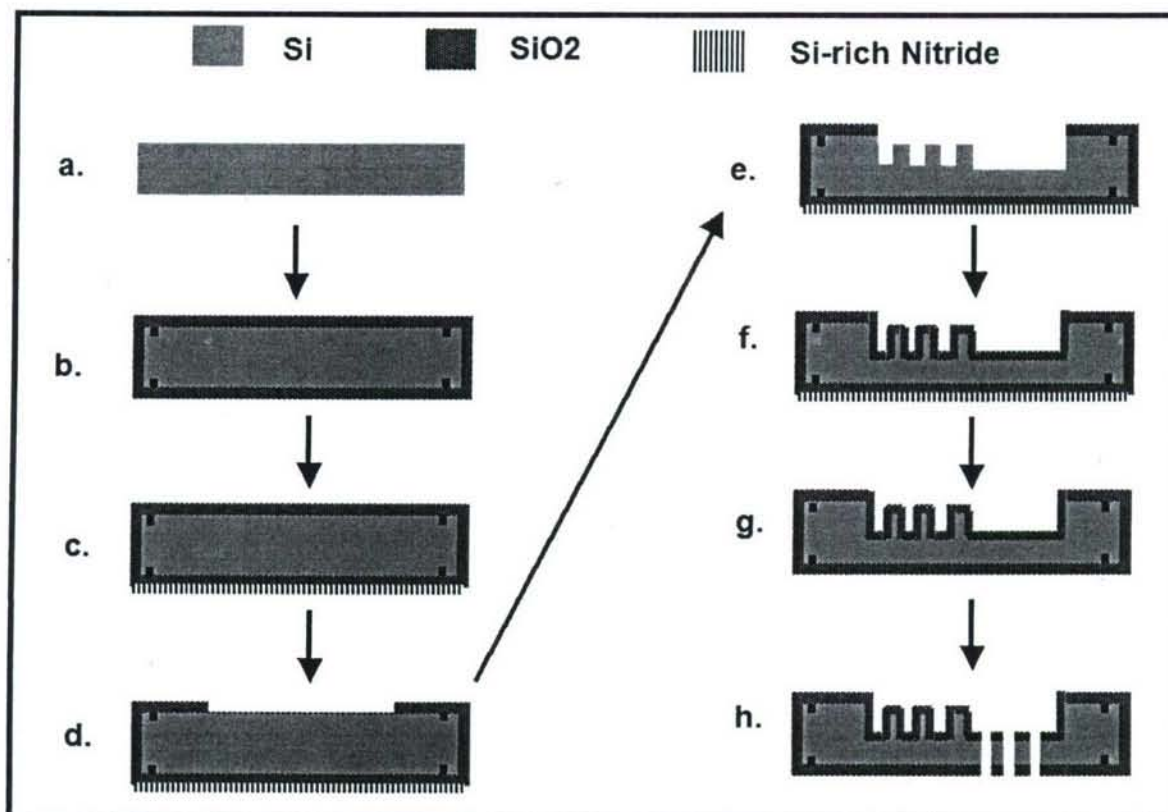


Figure 5. Process flow by which the middle wafer of the μ SOG is fabricated. The process flow starts with a DSP p-Si $\langle 100 \rangle$ wafer (a). The wafer is oxidized and alignment marks are transferred to both sides of the wafer (b). The wafer is then coated with $0.5 \mu\text{m}$ of LPCVD silicon-rich silicon nitride, and the film on the top of the wafer is stripped using an RIE step (c). The silicon oxide film on the top surface of the wafer is patterned with the layouts of the pressure drop channels, the liquid inlet manifold, the reaction channels without the packed beds, and the region occupied by the separator (d). The reactor packed beds and an opening in the region that the separator will eventually occupy are then patterned in resist and etched by DRIE (e). The photoresist film is stripped, and the features etched on the silicon oxide film on the top surface of the wafer are transferred to the silicon substrate using a DRIE step, while etching $20 \mu\text{m}$. The wafer is then oxidized (f), and the silicon-rich silicon nitride on the backside of the wafer is stripped using hot phosphoric acid (g). Finally, the layouts of the chip ports and the capillary separator are patterned in resist on the back side of the wafer, are transferred into the back side silicon oxide layer with BOE, and are transferred to the silicon with DRIE. The photoresist film is stripped (h).

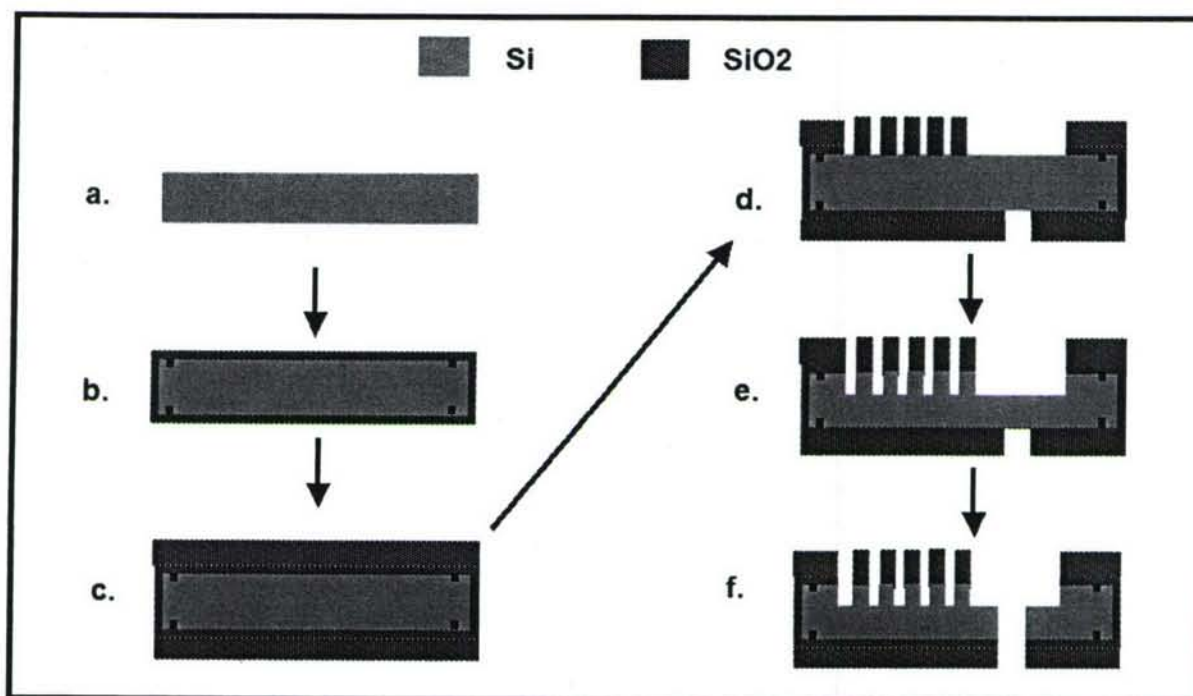


Figure 6. Process flow that fabricates the bottom wafer of the μ SOG. The process flow starts with a DSP p-Si <100> wafer (a). The wafer is oxidized, and alignment marks are transferred to both sides of the wafer (b). The wafer is then coated with 4 μ m of PECVD silicon oxide on both sides of the wafer and annealed at 950 °C in a nitrogen atmosphere (c). Resist is applied to both sides of the wafer. The resist film on the top of the wafer is patterned photolithographically with the layouts of the heat exchanger and the gas inlet manifold, while the bottom film is patterned with the layouts of the chip ports. The layouts of both resist films are transferred to the silicon oxide films using a cycled RIE plasma recipe (d). The top of the wafer is then etched with DRIE to a depth of 325 μ m (e). Finally, the wafer is flipped over and mounted on top of a quartz wafer, and the chip ports are etched with DRIE (f).

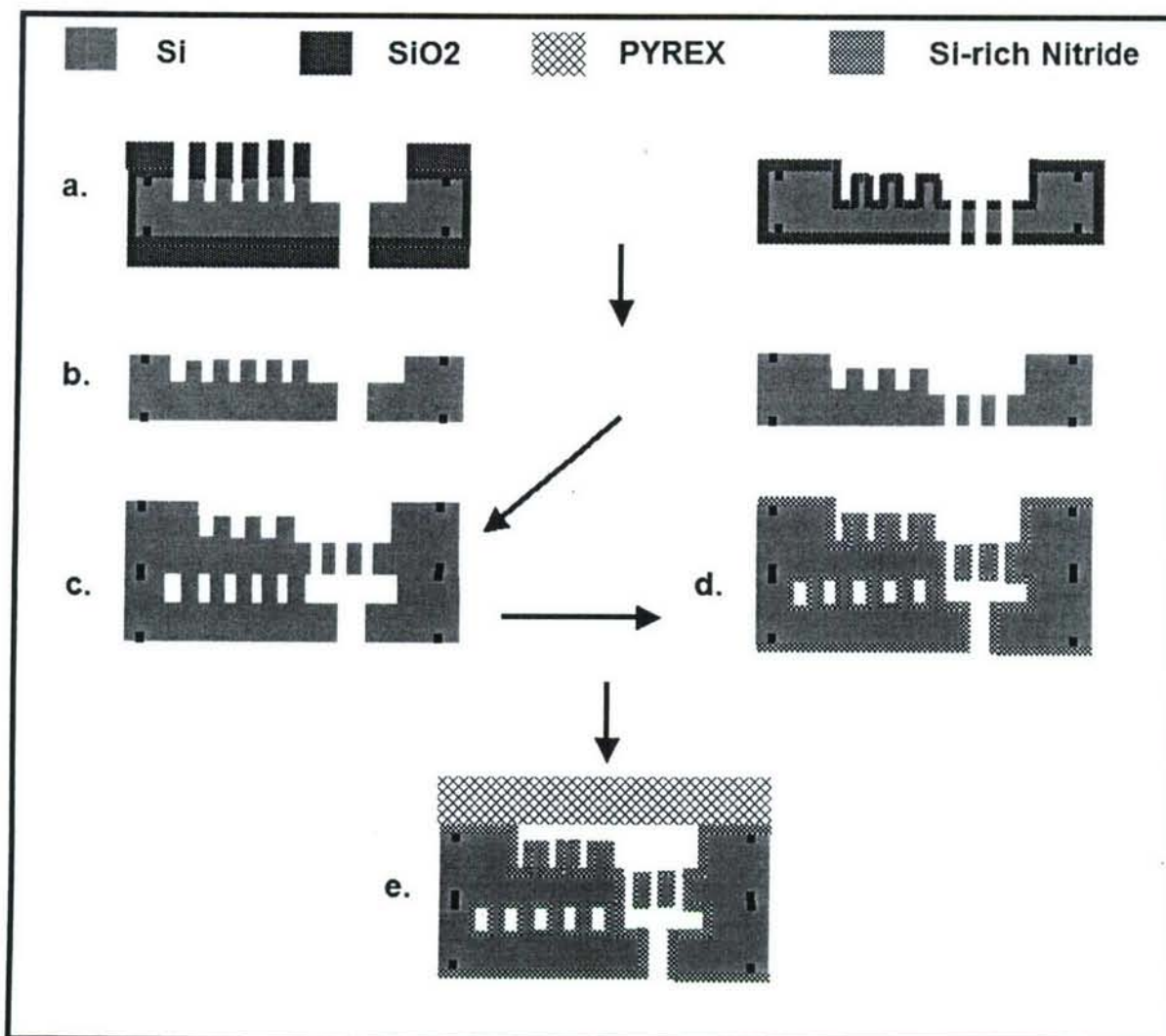


Figure 7. Process flow to finalize the fabrication of the μ SOG. The microfabricated middle and bottom wafers (a) are immersed in a 49% HF bath to strip the silicon oxide films (b). The two silicon wafers are fusion bonded (c). Then, a 0.4 μ m thick LPCVD silicon-rich nitride is conformally deposited on the silicon wafer stack (d). Next, the silicon wafer stack is anodically bonded to an unpatterned Pyrex® wafer (e). The wafer stack is then die-sawed to extract the SOG chips.

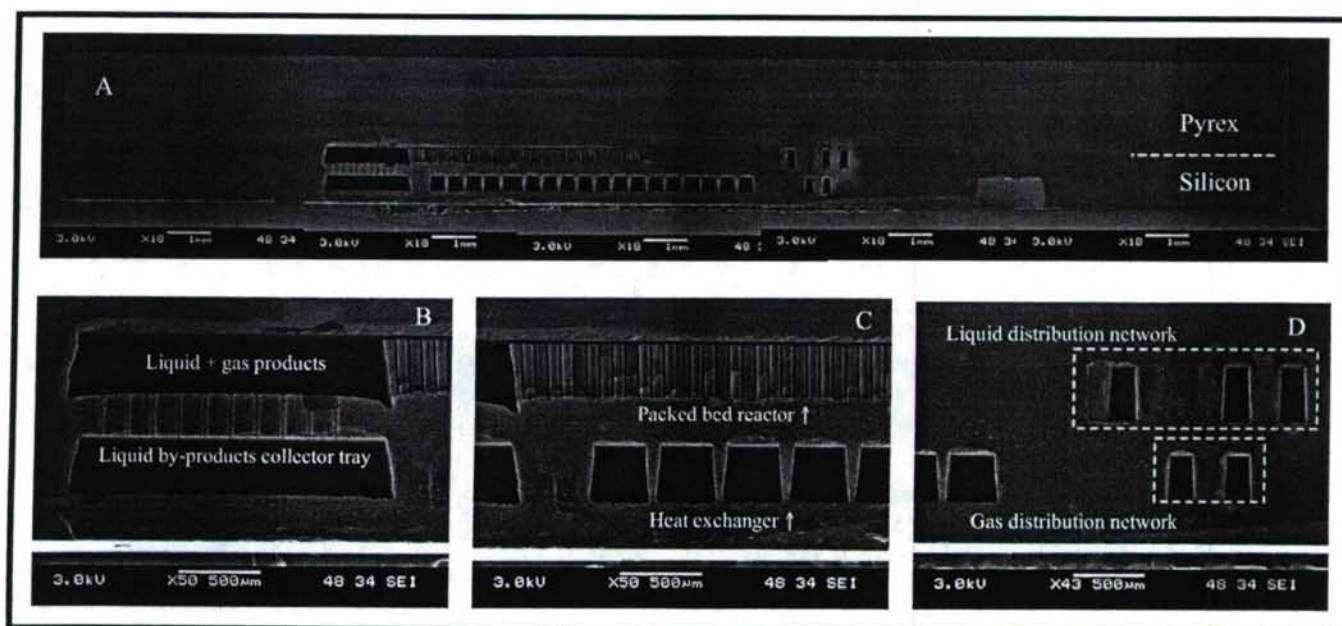


Figure 8. Set of SEM pictures that shows the cross section of a μ SOG chip (A), with several key features highlighted: separator (B), packed bed reactor and heat exchanger (C), and reactant distribution network (D).

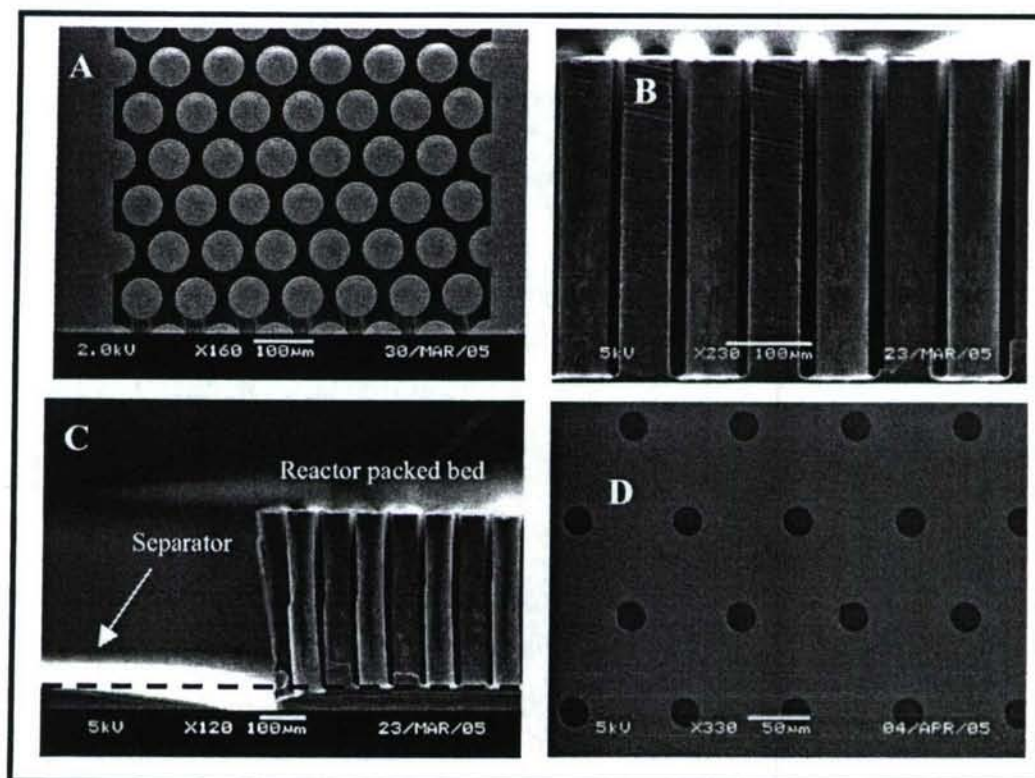


Figure 9. SEMs of the top view of a reactor packed bed channel (A), and its cross-section (B); cross-section of the separator near the end of the reactor array (C), and top view of the capillary separator (D).

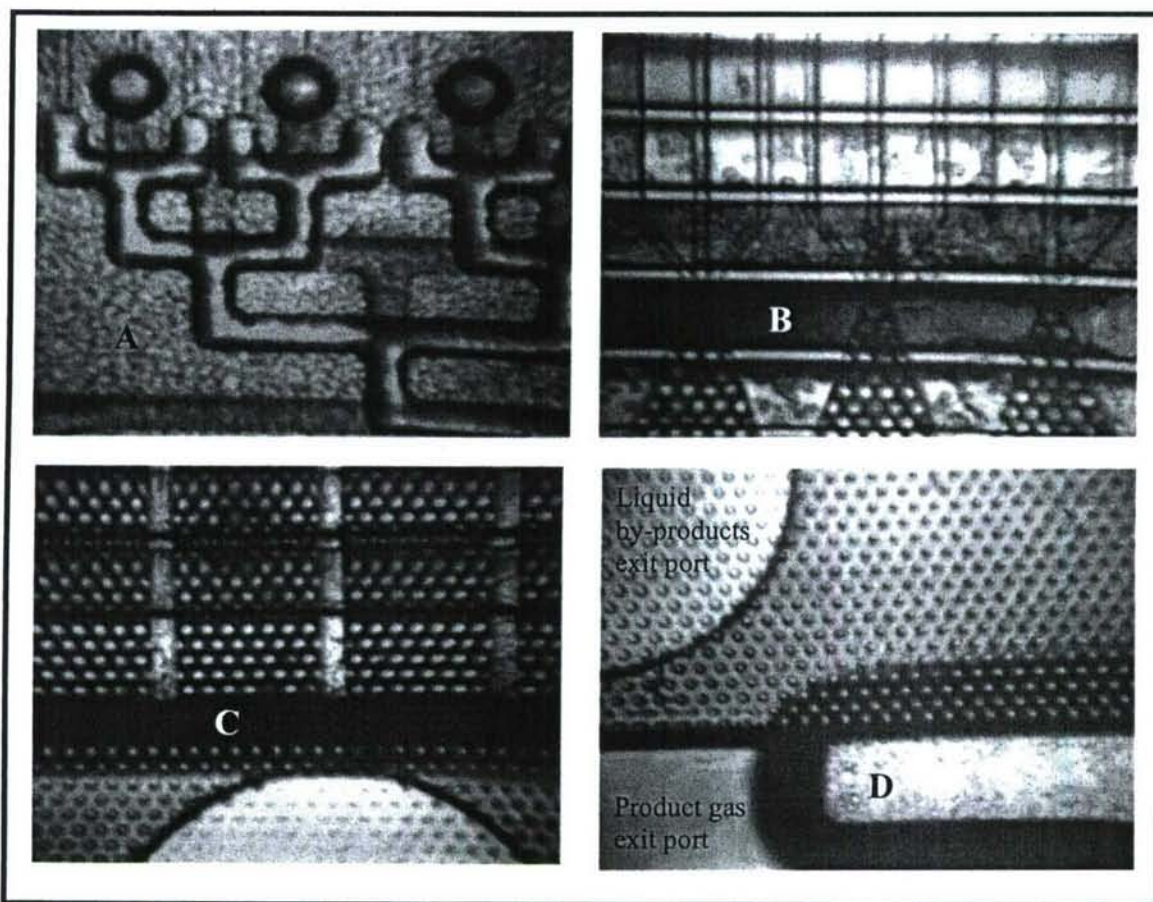


Figure 10. Set of IR microscope images that show the structure of the μ SOG chip. Liquid and gas reactant manifolds (A); reactant injectors (B); reactor packed bed on top of the heat exchanger (C); capillary separator (D).

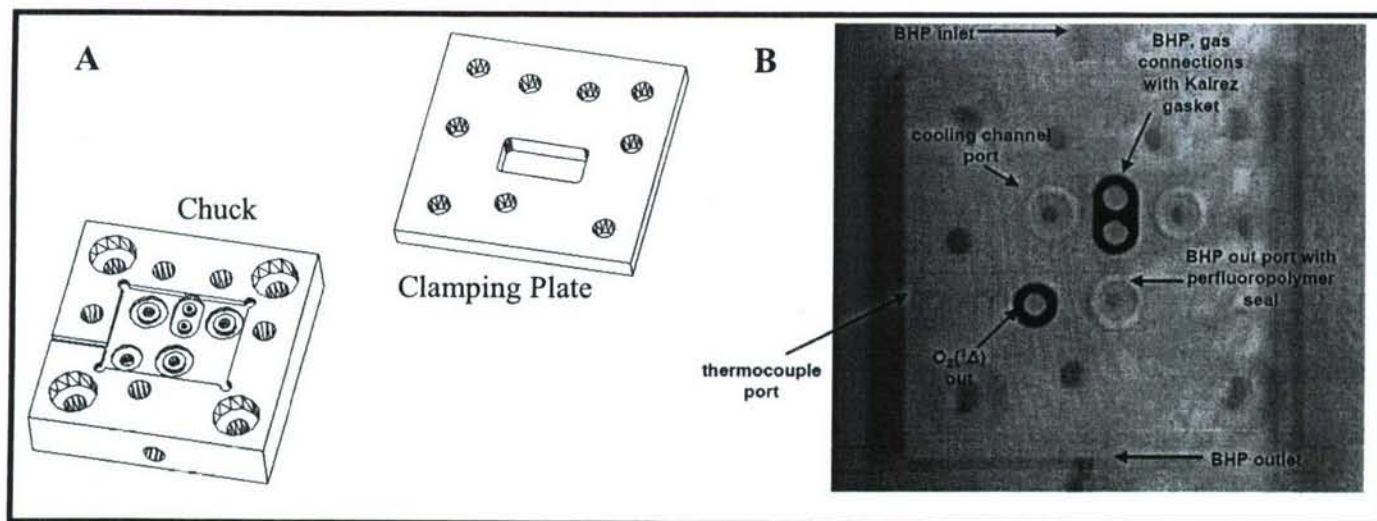


Figure 11. 3D drawing of the improved μ SOG package (A), and photograph of the package chuck with the o-ring and gaskets installed (B).

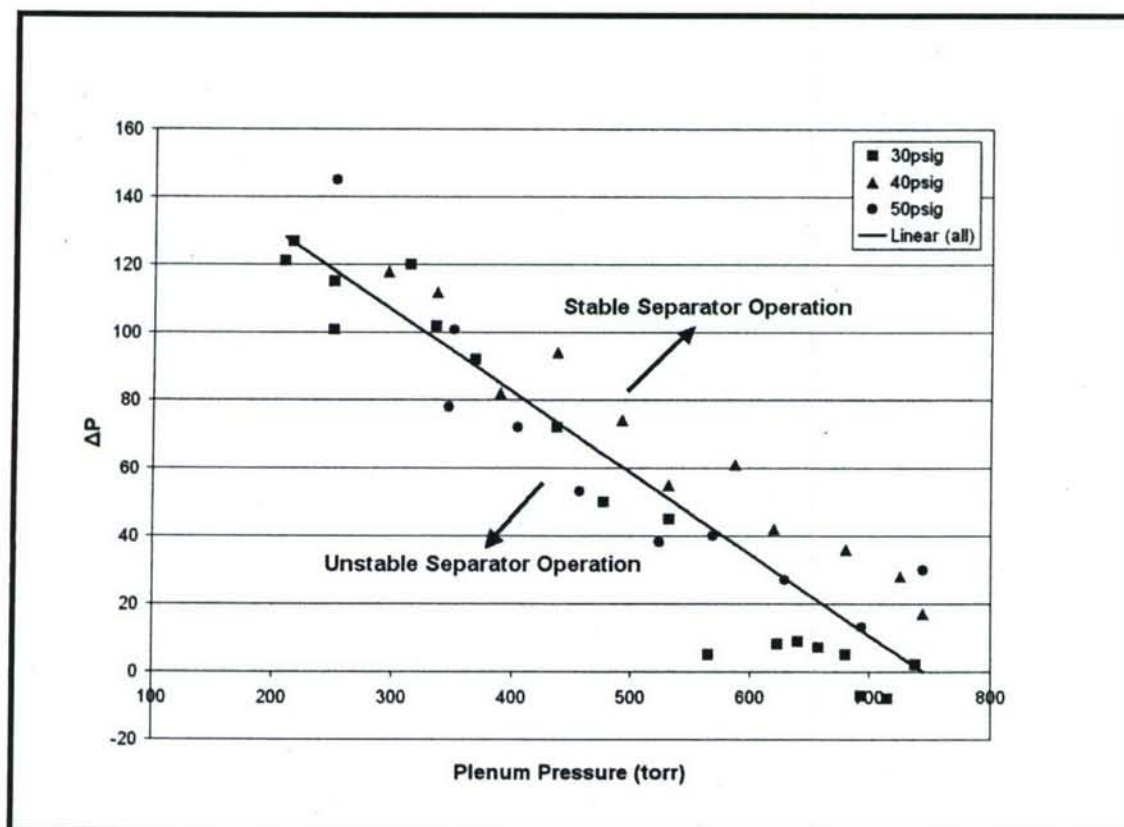


Figure 12. Minimum applied pressure drop across the capillary pores necessary to ensure proper separator functionality plotted vs plenum pressure for three liquid delivery pressures.

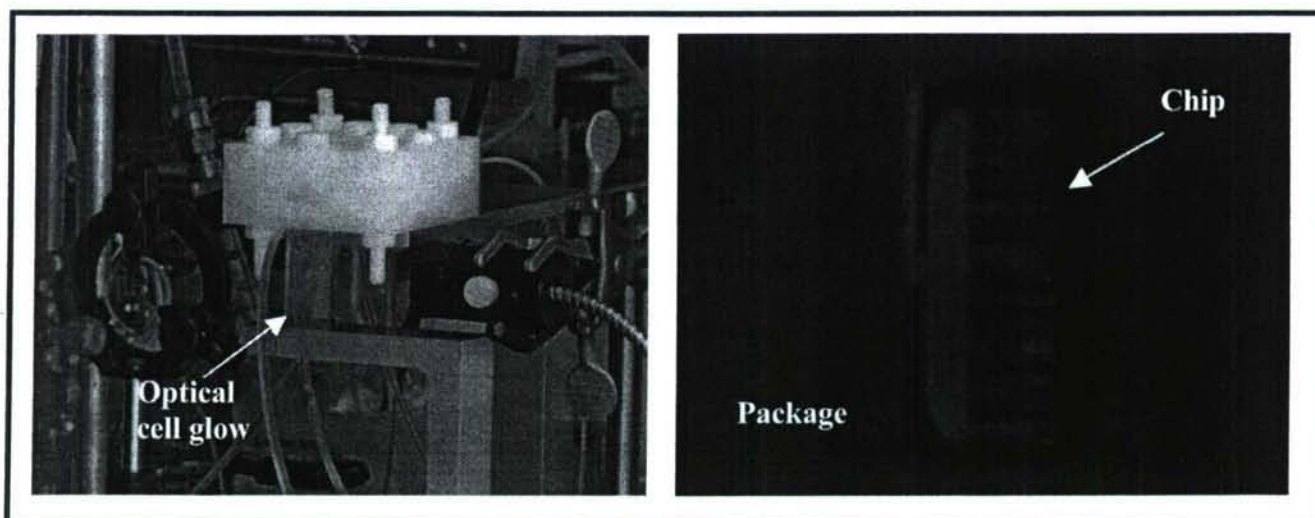


Figure 13. Photographs of the dimol emission (red glow) from the μ SOG in operation. Dimol emission seen in the quartz optical cell (A); top view of the dimol emission from the chip while producing singlet delta oxygen (B).

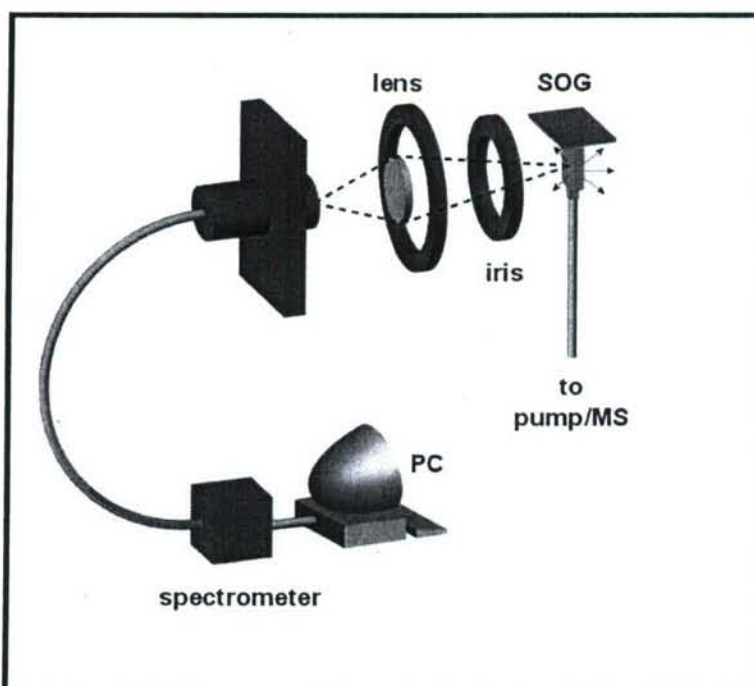


Figure 14. Schematic of the system used to obtain IR spectra from the optical cell.

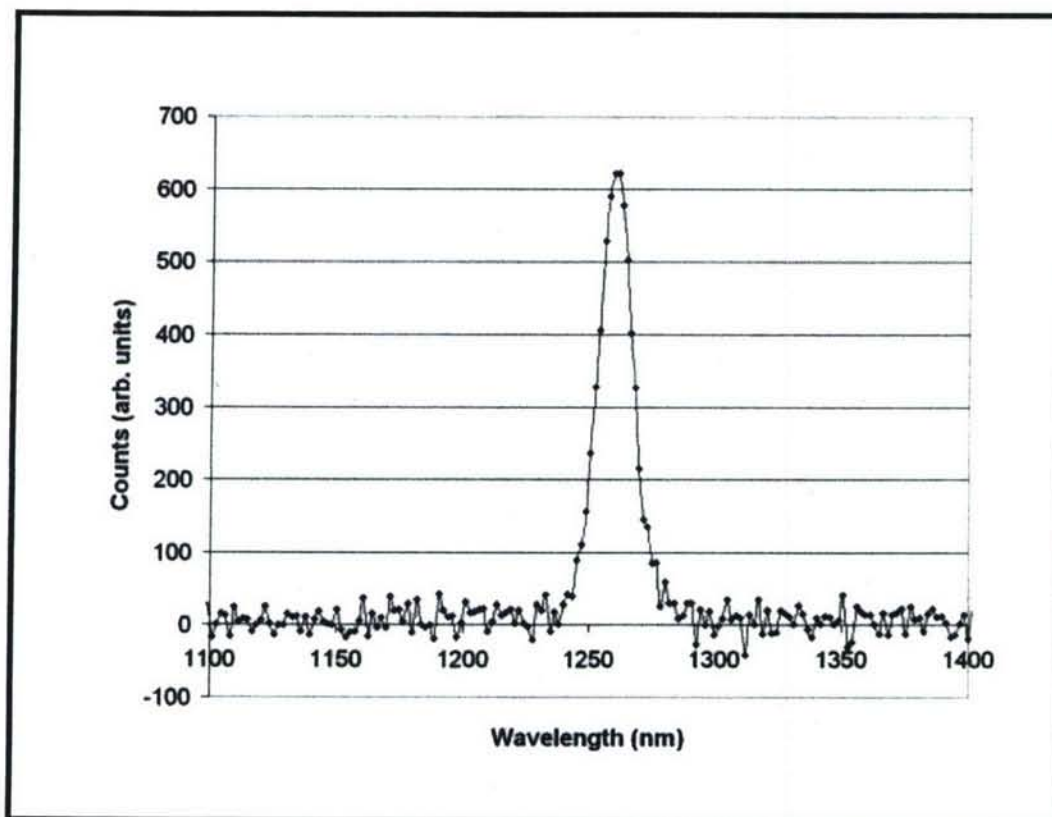


Figure 15. Typical IR spectra of the emission coming out of the μ SOG chip's quartz optical cell. The spectrum is mainly composed of photons from the $O_2(a)$ to $O_2(X)$ transition.

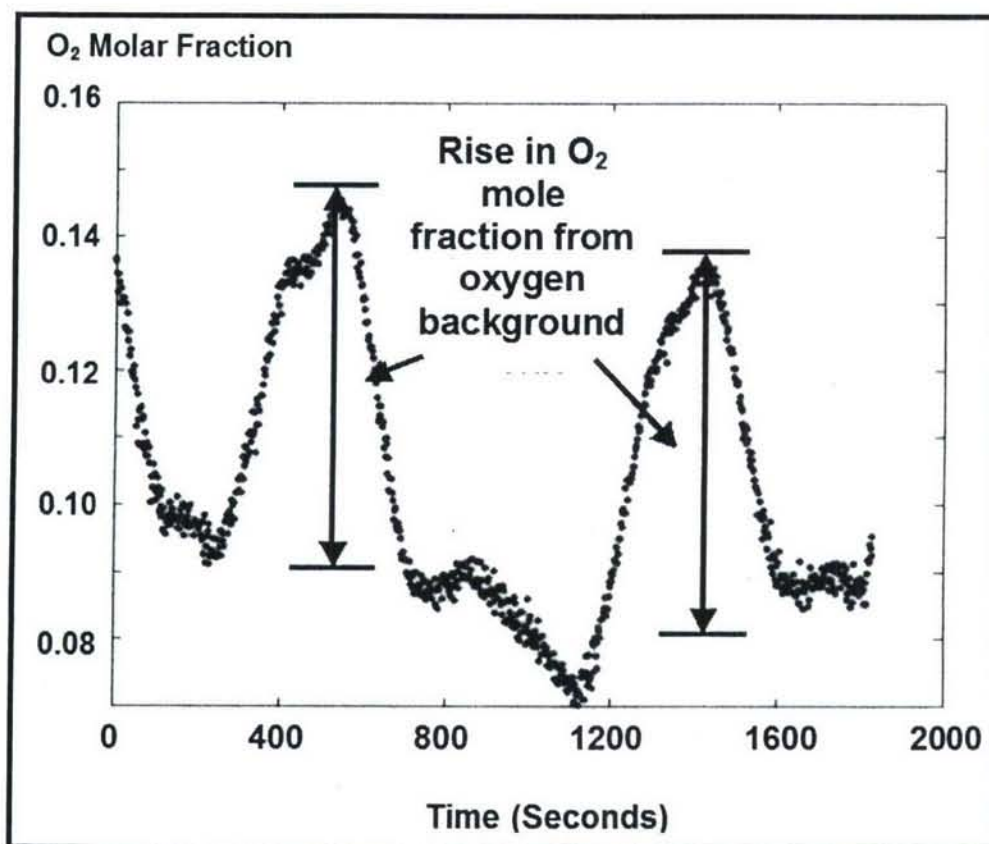


Figure 16. Mass spectrometer signal indicating an increase in O_2 , which coincides with the Cl_2 pulses.

Parameter	Value
He Flowrate	37 <u>sccm</u>
Cl_2 Flowrate	13 <u>sccm</u>
BHP Flowrate	1 ml/min
BHP Delivery Pressure	40 <u>psig</u>
Plenum Pressure	100 <u>torr</u>
Separator Pressure	20 <u>torr</u>
Chip Temperature	3 C
BHP Supply Temperature	-10 C

Table 1. Experimental conditions under which the μ SOG chip operated for the proof of concept demonstration. These particular operating conditions correspond to the spectrum shown in Fig. 20.

A MEMS Singlet Oxygen Generator – Part II: Experimental Exploration of the Performance Space

Tyrone F. Hill¹, Luis F. Velásquez-García¹, Benjamin A. Wilhite², W. Terry Rawlins³,
Seonkyung Lee³, Steven J. Davis³, Klavs F. Jensen¹, Alan H. Epstein¹, and Carol
Livermore¹

¹ Massachusetts Institute of Technology, Cambridge, MA 02139 USA

²Department of Chemical Engineering, University of Connecticut, Storrs, CT 06269 USA

³Physical Sciences Inc, Andover, MA 01800 USA

Corresponding Author:

Tyrone Hill, Massachusetts Institute of Technology
77 Massachusetts Avenue Building 31-231 Cambridge, MA 02139 USA
Phone (617) 258-8513 FAX (617) 258-6666 tfill@mit.edu

Abstract— This paper reports the quantitative experimental exploration of the performance space of a micro-fabricated singlet oxygen generator (μ SOG). SOGs are multi-phase reactors that mix H_2O_2 , KOH, and Cl_2 to produce singlet delta oxygen or $\text{O}_2(\text{a})$. A scaled down SOG is being developed as the pump source for a micro-fabricated Chemical Oxygen-Iodine Laser (COIL) system because scaling down a SOG yields improved performance compared to the macro-scaled versions. The performance of the μ SOG was characterized using $\text{O}_2(\text{a})$ yield, chlorine utilization, power in the flow, molar flowrate per unit of reactor volume, and steady state operation as metrics. The performance of the μ SOG is measured through a series of optical diagnostics and mass spectrometry. The test rig, which enables the monitoring of temperatures, pressures, and the molar flow rate of $\text{O}_2(\text{a})$, is described in detail. Infrared spectra and mass spectrometry confirm the steady state operation of the device. Experimental results reveal $\text{O}_2(\text{a})$ concentrations in excess of 10^{17} cm^{-3} , $\text{O}_2(\text{a})$ yield at the chip outlet approaching 80%, and molar flowrates of $\text{O}_2(\text{a})$ per unit of reactor volume exceeding $600 \times 10^{-4} \text{ moles/l/sec}$.

Index Terms— singlet delta oxygen, singlet oxygen generator, Chemical Oxygen Iodine Laser (COIL), microfluidics, IR diagnostics

I. INTRODUCTION

Singlet delta oxygen ($O_2(a^1\Delta_g)$ or $O_2(a)$) is a spin-excited molecule that is useful for many different applications. It differs from ground-state (triplet, $O_2(X^3\Sigma^-)$, or $O_2(X)$) oxygen in that the number of valence of electrons in each spin-state is balanced, resulting in an energy difference of 22.5 kcal/mol between the two states [1]. Chemical Oxygen Iodine Lasers (COIL) are flowing gas lasers that use $O_2(a)$ as a pump source for $I(^2P_{3/2})$ that subsequently lases to the lower $I(^2P_{1/2})$ state at 1.315 μ m. COIL lasers are scalable to high powers, making them an attractive alternative to CO_2 , HF, and DF lasers for applications requiring high power and a wavelength that can be transmitted through conventional glass optics. The wavelength also results in a smaller spot size than that of the 10.6 μ m wavelength CO_2 system, leading to better resolution and accuracy at higher powers. Since the gain medium is continually and rapidly pumped through the system, the power is not limited by cooling of the lasing medium as it is in solid state laser systems such as the Nd:YAG [2]. The COIL system is scalable to an average power output in excess of 1 MW [3]. As discussed in Part I of this work [4] and in [5], singlet oxygen generators (SOGs) produce $O_2(a)$ through a chemical reaction between gaseous Cl_2 and an aqueous mixture of concentrated H_2O_2 and KOH, also known as basic hydrogen peroxide (BHP).

This paper extends the experimental proof of concept provided in Part I (dimol emission, IR spectra, and correlation of chlorine injection with oxygen generation) by systematically exploring the operational space of the μ SOG to address whether the device reaches steady state and whether the chlorine is fully reacted, and to determine the highest yield, concentration, and molar flowrate of $O_2(a)$. It was expected that μ SOGs would perform better than their macro-scale counterparts because reducing the dimensions of the reactor both increases the reaction efficiency (as surface-to-volume ratio increases) and reduces the $O_2(a)$ losses (as residence time in the auxiliary flow paths decreases). The set of measurements described here is intended

to confirm this hypothesis. The experimental characterization is made using spectroscopy of the $O_2(a)$ dimol emission, spectroscopy of the spontaneous emission of the $O_2(a \rightarrow X)$ system, and mass spectrometry of the gaseous byproducts. This experimental characterization of the singlet oxygen generator for a COIL system utilizes a direct approach to measure $O_2(a)$ production. It is typical in the COIL field to benchmark the performance of the full COIL by metrics such as small signal gain of the laser, and then extract the SOG performance from models that incorporate the complex internal reactions of the COIL subsystems. In contrast, this work employs a direct, rigorous experimental benchmarking of the pump reactor for a COIL system as an independent entity.

II. PERFORMANCE CRITERIA AND TESTING METHODOLOGY

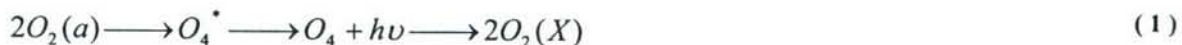
Beyond simply producing $O_2(a)$, there are several other requirements for the SOG for a COIL system, and several metrics by which SOGs are judged in the COIL community. First, the SOG must ensure that as much of the product O_2 as possible is in the $O_2(a)$ state. This is measured by the yield, or the fraction of O_2 in the singlet delta state at a given point in the system. A positive gain COIL system was first demonstrated by McDermott in 1978, with a yield of about 40% [6]. Second, the percentage of Cl_2 converted into O_2 (also called the chlorine utilization) should approach 100%, as any unreacted Cl_2 can deactivate the excited I atoms and impede laser operation. Third, the SOG hardware must be as compact as possible for a given output flow of $O_2(a)$. The authors propose that an appropriate performance metric for compactness is the molar flowrate of $O_2(a)$ per unit of reactor volume; a high value of this metric in this case would indicate that an array of MEMS-based SOGs could produce a total output of $O_2(a)$ that exceeds that of a comparably-sized macro-scaled SOG. Fourth, the SOG must operate at a low temperature to minimize the amount of water vapor in the output gas flow; water vapor can also deactivate excited I atoms. Fifth, and as described in Part I, the SOG must effectively separate out the liquid byproducts from the gaseous output flow. Finally, the SOG should operate in the steady state given steady state inputs (pressures, flow rates, and temperatures).

The values of the SOG performance metrics described above have a complex dependence on the flow rates, pressures, and temperatures at different points in the system, because these parameters in turn impact residence times, the rate of deactivation of $O_2(a)$ by various mechanisms, and whether the KCl reaction products are at sufficient concentration to crystallize and clog the reactor. Precise control and measurement of the operating conditions are necessary in order to fully characterize the SOG's performance over the parameter range of interest. The testing apparatus that enables the measurement and control of these parameters is described in section III of this paper, along with the apparatus for measurement of oxygen populations.

A range of diagnostics is required to measure the resulting SOG performance. The simplest of these diagnostics is flow visualization using a microscope and camera. The flow is visualized in the flow distribution channels, the reaction channels, and the capillary separator.

Although it is relatively straightforward to confirm $O_2(a)$ generation [4], quantitatively measuring the $O_2(a)$ concentration and yield are significant challenges. Typically SOG performance is determined in the context of a complete COIL system; heuristics are used to estimate yield from small signal gain and laser output along with various losses and efficiencies in the system [7]. In this work, a suite of more direct diagnostics are instead employed to obtain both qualitative and quantitative information on the $O_2(a)$ population.

Production of $O_2(a)$ can be confirmed by observing the red glow of the $O_2(a)$ dimol emission, either visually as described in Part I or through spectroscopy. The exact mechanism is unknown but has been postulated as



This emission produces photons of wavelengths 634 and 703 nm, depending on the vibrational state of the resulting $O_2(X)$ molecules, thus falling into the visible range [8]. However, since the dimol emission rate varies with pressure and other factors, drawing quantitative conclusions from it is difficult [9]. In contrast, the decay of solitary $O_2(a)$ molecules into the triplet state, which produces photons in a

molecular band centered at 1268 nm, can be used to determine $O_2(a)$ concentration because there is a one-to-one relationship between the photon emission rate and the number of $O_2(a)$ molecules in the field of view. By normalizing the $O_2(a)$ concentration by the initial Cl_2 concentration, the product of the $O_2(a)$ yield and the chlorine utilization can be determined. One method of determining chlorine utilization is to analyze the gaseous by-products of the SOG, for example by mass spectrometry, to determine the total oxygen in the flow. Comparing the total oxygen output to the chlorine input yields the chlorine utilization. Alternatively, the $O_2(a)$ concentration and yield-utilization product just after $O_2(a)$ production can be estimated from the concentration and yield-utilization product at the measurement point and models of the deactivation of $O_2(a)$ en route to the measurement point. This estimated value of the yield-utilization product is a lower bound on the value of the chlorine utilization.

One final aspect of the test methodology for this work is the use of detailed, quantitative models of the SOG to better understand and describe its performance. These include models of the reaction channels, models of the $O_2(a)$ loss mechanisms in the outlet flow paths, and models of the supporting subsystems such as the heat exchangers and the capillary separator. These models are described in detail in section IV of this paper, and their application to the analysis of the results is presented in section VII.

III. TESTING APPARATUS

A. Packaging

The completed devices were packaged using a Tefzel[®] chuck and Telfon[®] tubing. The plates have machined ports that allow for the reactants and products to enter and exit the chip. Kalrez o-rings enable leak free operation of the chip over a range of pressures and easy chip assembly to the testing facility. The package materials were chosen for their chemical resistance to BHP and chlorine. For the connection to the chip's gas outlet port, quartz surfaces were chosen in part to minimize $O_2(a)$ deactivation. The packaging scheme is described in greater detail in Part I [4].

B. Testing Rig

All experiments were performed inside a ventilated cabinet because of the toxic and corrosive nature of chlorine gas and BHP. The BHP is stored in a glass-lined, stainless steel pressurized reservoir. The BHP is pressure fed to the chip by introducing He into the vessel that contains the BHP. The helium pressure (and thus the BHP flowrate) is regulated by a pressure controller (MKS Instruments, Wilmington, MA). The BHP reservoir and μ SOG package are connected using Teflon[®] tubing and Upchurch PEEK connectors. The liquid by-products coming out of the chip are collected in a second reservoir. Both reservoirs were maintained at temperatures between -20°C and -10°C to minimize BHP decomposition. Ensuring that the BHP is properly cooled is critical for safety; at temperatures above 50°C , H_2O_2 decomposition is accelerated, and the solution can be explosive. Temperatures throughout the testing rig are monitored using thermocouples. Compressed tanks of Cl_2 and He are stored in a cabinet below the experiment, and gas flow to the chip is controlled by mass flow controllers and manual valves. The majority of gas connections preceding the chip use stainless steel tubing and Swagelok connectors. The connections immediately preceding and following the μ SOG package are made with Teflon[®] tubing, which was chosen for its flexibility and low reactivity with BHP. Before reaching the vacuum pump, both μ SOG exit lines (one for gaseous products and one for liquid by-products) pass through liquid nitrogen cooling traps in order to condense water vapor and unreacted chlorine. The gas outlet is then connected to a mass spectrometer through a glass capillary line, allowing sampling of a portion of the plenum stream. The entire setup is served by an external chiller (Julabo, Allentown, PA), which delivers a silicone-based cooling fluid to the system through Tygon Tubing. Figure 1 illustrates the main features of the testing rig.

C. Oxygen Diagnostics

Singlet delta oxygen concentration measurements were taken using quantitative spectroscopic techniques developed at Physical Sciences Inc. (Andover, MA) and also described in [10]. The test cell was a rectangular quartz cuvette (Starna, Atascadero, CA) that was connected to the μ SOG plenum by a 0.2 cm diameter quartz tube. Collimated optics sampled a cylindrical cross section of the cuvette, yielding a 1.1

cm field of view. The cuvette and collimator are depicted in Figure 2. In addition to the uncalibrated spectroscopy of the spontaneous $O_2(a)$ decay described in Part I, a liquid-nitrogen cooled InGaAs array spectrometer (Roper Scientific, Trenton, NJ) was used to analyze photons from the spontaneous emission. The intensity of the spectrometer signal was calibrated to the spectral radiance of a blackbody source at 1000 K. This setup is capable of acquiring a sequence of spectral scans separated by a predetermined integration time. Additionally, a third spectrometer was used to qualitatively measure the intensity of the dimol emission.

Finally, mass spectrometry measurements were made on samples taken from the gas exit line with the intent of using the rise in O_2 mole fraction to determine the degree of chlorine utilization as described above. To this end, sample gas from the gas outlet flow path was collected by a silica capillary after passing through a liquid nitrogen trap. The mass spectrometer, which had its intensity calibrated with an 80%/20% He/O_2 mixture, is able to detect constituent elements of the gas stream by first ionizing the molecules and then scanning for certain masses using a quadrupole mass filter.

IV. SOG DESIGN AND MODEL

The $O_2(a)$ production model originates in a series of chemical reactions, given in Table I, that describe the interactions between reactants, products, and intermediate compounds. The reaction between Cl_2 and the BHP solution can be described by reactions R1b-R1e. There is significant uncertainty in the rate of the reaction between Cl_2 and BHP [11][12][13]. However, reaction R1b is generally considered to be the rate limiting step. The mass transfer coefficient can therefore be described by

$$k_L = \sqrt{k_1 \cdot D'_{Cl_2} \cdot [O_2H^-]}, \quad (2)$$

where k_1 is the R1b reaction coefficient, D'_{Cl_2} is the diffusivity of Cl_2 in BHP, and $[O_2H^-]$ is the peroxide ion concentration. Taking D'_{Cl_2} to be $9 \times 10^{-6} \text{ cm}^2/\text{s}$ [3] and k_1 to be $2.7 \times 10^{10} \text{ cm}^3/\text{mol/s}$ [14], the thickness of the BHP surface layer in which the chlorine reaction occurs is estimated to be about 10 nm. One

quantity of interest is the rate of Cl_2 consumption $r_{\text{Cl}_2}^-$, expressed as

$$r_{\text{Cl}_2}^- = k_L \cdot a \cdot [\text{Cl}_2]_g, \quad (3)$$

where k_L is the mass transfer coefficient, a is the surface area per unit volume, and $[\text{Cl}_2]_g$ is the chlorine concentration in the gas. This expression assumes that the reaction at the liquid interface is so rapid that the rate is mass transfer limited and the interfacial concentration of chlorine is very small. This equation can be further simplified by applying the ideal gas law for the chlorine, which yields

$$r_{\text{Cl}_2}^- = k_L \cdot a \cdot y_{\text{Cl}_2} \frac{P}{RT}. \quad (4)$$

where P is the total pressure, y_{Cl_2} is the chlorine molar fraction, R is the universal gas constant, and T is the temperature of the gas. After the $\text{O}_2(\text{a})$ is produced, it diffuses out of the BHP and into the gas phase. The rate of increase of $\text{O}_2(\text{a})$ in the gas phase is given by

$$r_{\text{O}_2(\text{a})} = k_L \cdot a \cdot \chi_{\text{detach}} \cdot \frac{y_{\text{Cl}_2} \cdot P}{RT} + B \left(\frac{P}{n_t RT} \right)^2 \quad (5)$$

where n_t is the total number of moles of the gas. The first term of Equation 5 represents the liquid phase processes, including Cl_2 conversion, while the second term reflects the gas phase deactivation mechanisms described in Table I. The first term is similar to the chlorine consumption described in Equation 4, but with the addition of the factor χ_{detach} that describes the percentage of generated $\text{O}_2(\text{a})$ that appears in the gas phase. Some of the $\text{O}_2(\text{a})$ molecules are deactivated according to reaction R1e as they diffuse back across the 10 nm reaction depth to the liquid/gas interface; additionally, a small portion of the $\text{O}_2(\text{a})$ molecules that reach the liquid/gas interface diffuse back into the bulk liquid and are quenched. Several approaches to determining the detachment yield have been described in the literature [11][12][15][16][17]. These approaches produce similar but not identical estimates of detachment yield by describing similar mechanisms in various levels of detail. In all of these approaches, uncertainties in the physical constants (for example as reported in [13][15][18][19][20][21]) can result in significant uncertainties in the calculated detachment yields. In the present work, an initial estimate of the $\text{O}_2(\text{a})$ loss due to liquid phase deactivation

was made by comparing the timescale for $O_2(a)$ quenching in the liquid to the timescale for $O_2(a)$ diffusion back through the reaction layer [15]. Assuming that the diffusivities of oxygen and chlorine in BHP are $10^{-5} \text{ cm}^2/\text{s}$, the deactivation timescale is 40 times greater than the diffusion time, suggesting a loss of about 2.5% of the $O_2(a)$ en route to the liquid/gas interface. A more detailed approximation of χ_{detach} was obtained using the method of [11]. This approach takes into account both the deactivation by R1e and the surface detachment processes [11][16][17]. Using the same values for the diffusivities that are used above, this produces a χ_{detach} of 94%; alternatively, using the parameter values given in [11] would produce a χ_{detach} of 90%. These methods suggest that the detachment yield is in the range of 90% to 97.5%. Although a 5% to 10% yield loss corresponds to a large difference in $O_2(a)$ concentration in the reaction channels themselves, the change in concentration at the measurement point is only on the order of 10^{14} cm^{-3} because of gas phase deactivation. This difference is well below the detection limit of the optical emission diagnostic. As a result the model used here approximates $\chi_{detach} = 1$. The coefficient B in the second term can be expressed as

$$\begin{aligned} B = & -2k_2 y_{O_2(a)}^2 - 2k_3 y_{O_2(a)}^2 + k_4 y_{O_2(b)} y_{O_2(a)} \\ & + k_5 y_{O_2(b)} y_{H_2O} + k_6 y_{Cl_2} y_{O_2(b)} + k_7 y_{Cl_2} y_{O_2(b)} \\ & + k_8 y_{O_2(b)} y_{He} - k_9 y_{O_2(a)} y_{O_2(b)} - k_{10} y_{O_2(b)} y_{H_2O} \\ & - k_{11} y_{Cl_2} y_{O_2(a)} - k_{12} y_{O_2(a)} y_{He} \end{aligned} \quad (6)$$

where y_x is the molar fraction of the species x and each k coefficient is the particular reaction constant between two certain species as given in Table I. The pressure drop across the reaction channels is modeled using the Ergun equation [22], written as

$$\begin{aligned} \left. \frac{dP}{dz} \right|_g = & - \frac{F_t \cdot RT}{D_p \cdot P \cdot a_c} \cdot \left(\frac{1-\varepsilon}{\varepsilon^3} \right) \cdot \\ & \left[\frac{150 \cdot (1-\varepsilon) \cdot \mu_g}{D_p} + 1.75 \cdot MW_g \cdot \frac{F_t^2 \cdot RT}{P \cdot a_c} \right], \end{aligned} \quad (7)$$

where z is the distance along the reaction channel, F_t is the total molar flow rate (constant), D_p is the packing diameter in the channels, a_c is the cross sectional area of the reaction channels, ε is the void fraction, μ_g is the viscosity of the gas, and MW_g is the molecular weight of the gas. Assuming ideal plug

flow in the channels, the relationship between molar flow rate (F_i) and species production (r_i) for a species i is

$$\frac{1}{\varepsilon_g \cdot a_c} \cdot \frac{d(F_i)}{dz} = r_i, \quad (8)$$

where ε_g is the fraction of the volume in the reaction channels that is occupied by the gas phase.

Substituting Equation 5 into Equation 8 yields

$$\begin{aligned} \frac{dF_{O_2(a)}}{dz} = & \varepsilon_g \cdot a_c \cdot a \cdot k_L \cdot \chi_{\text{detach}} \cdot \frac{y_{Cl_2} \cdot P}{RT} \\ & + \varepsilon_g \cdot a_c \cdot B \left(\frac{P}{F_i RT} \right)^2. \end{aligned} \quad (9)$$

Similar expressions were obtained for the other reactants and reaction products. The kinetic model is discussed in more detail in [3].

Several modifications to the original model were made to analyze the data collected by the testing rig. The reactant properties, which were initially assumed to be similar to those of air and H_2O , were modified to more accurately represent BHP and Cl_2 [23]. Additionally, the μSOG dimensions were changed to reflect the fabricated device. Table II illustrates these changes.

A. Capillary Separator Region

The model was updated to reflect the dynamics of the capillary separator region. The separator, first described in [24] and [25], relies on capillary action to remove the liquid waste while allowing the gas to pass freely. The wetting front of the liquid by-products gets sucked in due to surface tension effects, thus filling in the capillary. The liquid will wet the capillary with a certain wetting angle θ (Figure 3, left). In a steady state flow configuration the capillaries are fully filled-in and thus, the separator is pressure driven (Figure 3, right). The maximum pressure drop that can exist across a capillary given a zero wetting angle is

$$\Delta P = \frac{4\Sigma}{\phi}, \quad (10)$$

where Σ is the surface tension of the liquid and ϕ is the diameter of the capillary. This value is also the

maximum pressure that surface tension effects can provide to pump the liquid byproducts without the need for an external pressure signal. For 20 μm wide capillaries and given the surface tension of water (72 dynes/cm), the maximum pressure drop that the meniscus can withstand is 108 Torr. A second expression for pressure can be obtained from the Hagen-Poiseuille equation if steady state, fully developed flow is assumed and the liquid is Newtonian, with pressure losses produced by viscosity. In this case the volumetric flowrate Q through each capillary is given by [26]

$$Q = \frac{\pi \Delta P \phi^4}{128 \mu L_c}, \quad (11)$$

where μ is the viscosity of the fluid and L_c is the channel length. For a given pressure drop across the separator, the number of pores needed to transport the liquid by-products can be found by dividing the total liquid molar flowrate Q_t by Q . Q_t is expressed as

$$Q_t = \frac{\gamma \phi y_{Cl_2}}{[O_2H]}, \quad (12)$$

where ϕ is the total gas molar flowrate, γ is the desired ratio of peroxide ions to Cl_2 , and y_{Cl_2} is the chlorine fraction of the entering gas stream. The original design called for a 10:1 peroxide ion to Cl_2 ratio and a peroxide ion concentration $[O_2H]$ of $6.5 \times 10^{-3} \text{ mol/cm}^3$. For a gas flow rate of 50 sccm, around 430 capillaries would be necessary; for a gas flow rate of 250 sccm, the number of capillaries necessary rises to about 2200. However, more than 7000 were included in the actual devices due to concerns about how many functioning pores would be produced in the DRIE steps. Also, it was desired to have some redundancy in the separator in case clogging occurred during testing of the chip.

B. Heat Exchanger

Because of the high enthalpy associated with the reaction, any $\text{O}_2(\text{a})$ generation system must include a heat removal mechanism. In the μSOG this task is accomplished using a heat exchanger composed of 19 parallel cooling channels that are situated directly beneath the reaction area. The lower silicon layer of the MEMS chip contains the micro-fabricated heat exchanger. The heat exchanger channels are filled with a

silicone-based coolant and are connected to an external chiller. Given an enthalpy of reaction of -110kJ/mol and a maximum Cl_2 molar flow rate of $3 \times 10^{-5} \text{ mol/sec}$ in these experiments, the heat exchanger needs to be capable of removing at least 3.5 W of heat in order to remove the excess heat of reaction. In addition, in order to maintain the chip at a temperature that lies within BHP safety limits and restricts the amount of water vapor in the exit flow, which is important for overall COIL performance, the heat exchangers must also remove the heat that enters the chip from the ambient, estimated to be about 10 W for the present experimental set up and an operating temperature of -5°C . In order to handle this task, the channels were sized at 23.9 mm in length and $300 \mu\text{m}$ wide. The heat removal capacity of the micro-fabricated heat exchanger was empirically verified before attempting to produce $\text{O}_2(\text{a})$. Using thermocouples to monitor the coolant and silicon temperatures, the specific heat equation was used to calculate the total heat removed. Figure 4 illustrates the measured heat removal capacity of the channels as a function of the silicon temperature. The heat removal capacity Ξ was calculated using the expression

$$\Xi = \dot{m} \cdot C_p \cdot \Delta T \quad (13)$$

where \dot{m} is the mass flowrate of coolant, C_p is its heat capacity, and ΔT is the temperature difference across the heat exchanger.

C. Singlet Delta Oxygen Deactivation

Once $\text{O}_2(\text{a})$ has been created, it can be deactivated both inside the μSOG chip and in the external flow paths by collisions with other $\text{O}_2(\text{a})$ molecules (pooling reactions) and collisions with the walls of the flow path. The rates of the pooling reactions and the wall deactivation reactions depend as described below on the geometry and material composition of the chip's internal gas exit path and the external flow path. The chip's internal exit flow path has a length of 1.8 cm and a width of 2 mm , and its surface is silicon-rich silicon nitride as described in Part I. Upon exiting the chip, the gas mixture flows into a quartz cuvette. The cuvette's inlet is a 1 cm long tube with an inner diameter of 2 mm , and it is connected by a 0.5 cm long transition region to a diagnostic region that has a $1 \times 1 \text{ cm}$ square cross-section. The rectangular portion

features 1 mm thick walls.

The mole fraction $y_{O_2(a)}$ of $O_2(a)$ in a rectangular volume as a function of flow length can be described as

$$\frac{dy_{O_2(a)}}{dl} = \frac{-(2k_3 + k_2)P}{RTv_{gas}} y_{O_2(a)}^2 - \psi_w \frac{(W + H)}{2WH} \sqrt{\frac{8RT}{\pi(MW_{O_2})}} y_{O_2(a)}, \quad (14)$$

where P is the total pressure of the gas, R is the universal gas constant, T is the gas temperature, v_{gas} is the flow velocity, W is the width of the flow path, H is the height of the flow path, (MW_{O_2}) is the molecular weight of oxygen, ψ_w is the $O_2(a)$ deactivation coefficient for the particular wall material, and l is the dimension along the flow axis. The first term of Equation 14 derives from the reactions described in Equation 6; only the dominant terms are kept, and the rate of reaction 5 is taken to be large enough to make the net effect of reaction 2 be the deactivation of a single $O_2(a)$ molecule. Equation 13 is the well-known Ricatti equation [27]

$$\frac{du(l)}{dl} + \Lambda(l) \cdot u(l) + \Theta(l) \cdot u^2(l) = \Omega(l) \quad (15)$$

where $u(l)$ is the function and l is the independent variable. The transformation

$$u(l) = \frac{dw(l)}{dl} / [\Theta(l) \cdot w(l)] \quad (16)$$

converts the non-linear differential equation into the homogeneous, linear, second order ordinary differential equation

$$\frac{d^2w(l)}{dl^2} + \left[\Lambda(l) - \frac{d\Theta(l)}{dl} / \Theta(l) \right] \cdot \frac{dw(l)}{dl} + \Omega(l) \cdot \Theta(l) \cdot w(l) = 0 \quad (17)$$

For the particular case of Equation 14,

$$\Lambda(l) = \Lambda = \psi_w \frac{(W + H)}{2WH} \sqrt{\frac{8RT}{\pi MW_i}} \quad (18)$$

$$\Theta(l) = \frac{(2k_3 + k_2)P}{RTv_{gas}}, \quad \frac{d\Theta(l)}{dl} = 0, \quad \Omega(l) = 0. \quad (19)$$

Therefore, Equation 17 simplifies to

$$\frac{d^2 w(l)}{dl^2} + \Lambda \cdot \frac{dw(l)}{dl} = 0. \quad (20)$$

The solution of Equation 20 is

$$w(l) = C_1 e^{-\Lambda l} + C_2 \quad (21)$$

where C_1 and C_2 are integration constants. Substituting Equation 21 into Equation 16, and applying the initial condition that $y_{O_2(a)}(l=0) = y_0$, the initial mole fraction of $O_2(a)$, the solution of Equation 14 is

$$y_{O_2(a)}(l) = \frac{y_0}{\left[y_0 \cdot \frac{\Theta}{\Lambda} + 1 \right] \cdot e^{\Lambda l} - y_0 \cdot \frac{\Theta}{\Lambda}} \quad (22)$$

It can be quickly verified that $y_{O_2(a)}(l \rightarrow \infty) = 0$ and that $y_{O_2(a)}(l \geq 0) > 0$. For a very small wall deactivation coefficient $\Lambda \ll 1$ so that $e^{\Lambda l} \cong 1 + \Lambda \cdot l$, Equation 22 simplifies to

$$y_i(l) = \frac{y_0}{1 + y_0 \Theta l}, \quad (23)$$

Equation 23 was used to determine the $O_2(a)$ concentration and yield-utilization product at the chip's $O_2(a)$ gas outlet from the measured values in the diagnostic region of the quartz cuvette.

According to Equation 23, most of the $O_2(a)$ is expected to have returned to the ground state by the time it reaches the measurement point, with pooling losses expected to dominate. In a real MEMS-based COIL laser, however, the mole fraction of $O_2(a)$ is expected to be much higher at the point at which the iodine flow is injected in order to produce the lasing effect. In the present experiments, the significant deactivation that takes place before the measurements are made is a function of the scale mismatch between the μ SOG and the macroscale diagnostic region, which results in a small value for v_{gas} . In a scaled-up system of many arrayed μ SOGs, the higher $O_2(a)$ flow rates will increase v_{gas} and greatly reduce the deactivation as compared with the present experiments. Although some deactivation will still occur, it is expected that the amount of deactivation between the point of $O_2(a)$ production and the chip's exit port in the present experiments will be a better predictor of the deactivation that will occur in the internal flow

paths that will ultimately connect the μ SOGs to the rest of the MEMS COIL system.

V. EXPERIMENTAL PROCEDURE

The first step in the experiment is to prepare the BHP solution, which consists of equal parts 50 wt% aqueous KOH solution and 50 wt% H_2O_2 . The external chiller is set at -20°C , with the aim of the coolant reaching the rig at a temperature of -15°C . The KOH solution is prepared by dissolving KOH pellets (Mallinckrodt, Phillipsburg, NJ) in de-ionized water. The KOH and H_2O_2 were mixed together slowly, to ensure that the temperature never exceeded 25°C . BHP and He flow were first initiated in the chip at atmospheric pressures. Gas and liquid flow were immediately visible in the reaction channels, and the capillary separator functioned correctly at the outset. The set points of the pressure controllers were then gradually lowered until the desired operating points were reached. The coolant flow was then started and increased until it reached its set point at around -5°C . Once the set points of pressure and temperature had been reached, the chlorine, flowing concurrently with helium with a 3:1 ratio of He to Cl_2 , was injected into the chip in pulses that were typically one minute in length. The photonic emission coming out of the exit flow was measured using the spectrometric setup previously described, and the gas products were analyzed using a commercial mass spectrometer. After a number of runs, the remaining BHP was collected, and then the chip was warmed up (the coolant flow was stopped) while flowing de-ionized water to ensure chip reutilization. After a few minutes of water flow, the chip was dismounted from the package, dried out using an oven, and stored for future use. Data were taken at 15 different operating points. The plenum pressure ranged from 50 – 200 Torr, and the total gas flow rate was varied between 50-200 sccm. Crystals of KCl were observed to form in the device channels after a number of runs (and in particular after runs with very high ratios of chlorine gas to BHP) and eventually led to clogging in the device channels. The clogging in turn lessened the intensity of the spectral peaks with successive chlorine pulses. The implications of the observed clogging for the μ SOG's utility and for the analysis of the results are discussed further in section VII. It was also observed that very little of the capillary separator area appeared to be used in removing

waste products, as expected from the considerable over-sizing of the separator as described earlier. This experimental fact will be important when discussing the $O_2(a)$ yield and will also be discussed further in section VII.

VI. STEADY STATE VALIDATION AND DIMOL EMISSION CHARACTERIZATION

Confirmation of the steady state operation of the chip was achieved using two different diagnostics. The first diagnostic was measurement of the infrared spectra. The IR spectra were recorded to monitor the $O_2(a \rightarrow X)$ transition, starting from the moment the chlorine plug was delivered to the chip. A typical set of IR spectra is shown in Figure 5. Each spectral curve is obtained with a 5-second integration time. It is clear from Figure 5 that the device quickly reaches steady state operation after the chlorine pulse is started. It can also be seen that there is some minor production of $O_2(a)$ after stopping the chlorine delivery, probably due to the non-idealities of the testing setup (dead volume within the pipes, non-perfect seal of the mass flow meters, etc.). The increase in intensity after scan 20 is due to a reduction in the He flow rate, which in turn increased the Cl_2 residence time in the inlet lines. Each of the IR spectra (Figure 6) shows the characteristic molecular band structure of the emission transition from $O_2(a^1\Delta_g, v=0)$ to $O_2(X^3\Sigma_g^-, v=0)$, with a prominent Q-branch at the band center and weaker rotational branches on each side. Spectroscopic analysis of the detailed band shape gives the rotational temperature of the $O_2(a)$, which is the same as the gas temperature for these conditions [10]. It is interesting to observe that even though the chip is kept at sub-zero temperature, the $O_2(a)$ at the detection point is at temperatures above 300 K. It is likely that the gas is warmed by a combination of conduction from the room-temperature optical measurement cell and energy released from the $O_2(a)$ pooling reactions.

Figure 7 shows the dimol spectra of multiple runs. It can be seen that the spectrum is centered around two peaks (one each at 634 nm and at 703 nm), as expected from the known behavior of the dimol emission.

The second approach to determining the steady state operation of the device used the mass spectrometer

data (Figure 8). The figure clearly shows a rise in the O_2 partial pressure roughly corresponding to the Cl_2 pulse. The increase in O_2 partial pressure appears approximately constant during the Cl_2 pulse, given the time-averaging effects of the long time constant for transport through the sampling capillary, thus indicating steady state operation. Attempts at quantitatively measuring the increase in O_2 mole fraction with mass spectrometry were hampered by limitations in the testing rig. Specifically, the low temperature of the LN_2 traps condensed out much of the O_2 in the gas stream along with the Cl_2 . The mass spectrometry therefore substantially underestimated the O_2 production, as evidenced by the fact that the amount of $O_2(a)$ detected by IR spectrometry at the measurement point (even without taking into account deactivation losses) sometimes exceeded the amount of total O_2 detected in the outlet flow by mass spectrometry.

The steady state production of $O_2(a)$ masks an intricate fluid dynamics process, shown in Figure 9, where trickling rather than plug flow was observed in the reaction channels.

VII. DATA ANALYSIS: $O_2(a)$ YIELD, CHLORINE UTILIZATION AND FLOW POWER

The $O_2(a)$ emission spectra were corrected for instrumental baseline and for the absolute spectral responsivity using the blackbody calibration results. The corrected spectra were integrated over the entire molecular band to determine the volumetric photon emission rate within the field of view. When this value is divided by the Einstein coefficient, which represents the rate at which $O_2(a)$ molecules decay into the $O_2(X)$ state ([28], [29]), the concentration of $O_2(a)$ is determined [10]. This concentration is an average over the field of view. The μ SOG emission measurements were taken near the center of the quartz cuvette attached to the package, at a distance of approximately 3.05 cm from the gas outlet of the chip. Table III summarizes the conditions for each run, along with the measured concentrations at each point. The error in the measurements, around 13% for each run, results from uncertainty in the Einstein coefficient (10%) as well as from small uncertainties in the geometry of the setup. The measured $O_2(a)$ concentrations range from 5×10^{16} to $1 \times 10^{17} \text{ cm}^{-3}$. The yield-utilization product, or the amount of O_2 in the $O_2(a)$ state assuming 100% Cl_2 utilization, is also given in Table III. Ideally, the $O_2(a)$ concentration would be measured at the

gas outlet, since that is the point at which the next stage of the laser system would be connected. Measurements are made further down the cuvette in this case in order to ensure that the field of view of the collimated optics is not obscured by the package or other parts of the test apparatus. Fortunately, Equation 23 can be used to extrapolate the $O_2(a)$ concentration and yield-utilization product anywhere along the flow path given a concentration value downstream from that point, albeit with increasingly larger error bars. In this analysis, Equation 23 is used to extrapolate the measured concentration and yield utilization product up to the chip's gas outlet. As was mentioned above, the values at the chip's outlet are expected to be a better predictor of the performance of the μ SOG chip in a complete MEMS COIL system than the value at the current measurement point is. The scale mismatch between the μ SOG and the external diagnostic region in this case leads to low flow velocities and much greater $O_2(a)$ losses than would occur in a MEMS COIL system in which the components were integrated at the MEMS scale. When the measured values are extrapolated to the chip's outlet using Equation 23, the resulting values are substantially higher, with yield-utilization products approaching 80% and with the concentrations in most runs in excess of 10^{17} cm^{-3} .

When the yield-utilization products extrapolated from the raw data were compared with those predicted by the baseline kinetics model described above, it became evident that some modification to the baseline model would be necessary in order to adequately explain the results. In most of the experimental runs, the extrapolation of the measured data produced higher but plausible values of the concentration and yield-utilization product; however, in four of the runs, the extrapolation produced values of concentration and yield-utilization product that were not possible. In those four cases, the extrapolation indicated that there was more than one $O_2(a)$ appearing at the chip's gas outlet for each Cl_2 that entered at the input, which is not possible. In some of these cases, even extrapolating the lower error bar for the measurement point produced unphysically high values for $O_2(a)$ concentration at the chip's outlet.

Three sources of error were identified as possible contributors to the discrepancy. The first is clogging in the pressure drop and reaction channels, caused by KOH crystal precipitation and KCl salting respectively.

The second is the possibility that some of the output gas was sucked through open pores in the capillary separator rather than exiting through the gas outlet. The third is the documented uncertainty in the kinetics rate coefficients k_2 and k_3 that appear in the Θ coefficient in Equation 23 [30]. Each of these three error mechanisms is discussed below; it will be seen that only the uncertainty in the pooling rate coefficients provides an adequate explanation of the discrepancy between the baseline model and the results.

Clogging of the flow channels was observed under two general conditions: when the chip had been operated for long periods of time with moderately high ratios of chlorine to BHP, and when the chip had been operated even for short times with particularly high ratios of chlorine to BHP. During operation, clogging was evidenced by a pressure rise on the gas feed lines for a given mass flow rate of feed gas. It is not surprising that clogging occurred in some of the runs. The μ SOG was designed to operate with a ratio of BHP to chlorine that corresponds to a 10:1 ratio of peroxide ions to chlorine as compared with a many tens to one ratio that is used to prevent clogging in macroscale SOGs; a lower ratio corresponds to more efficient reactant usage. In practice, in these experiments the chip was usually operated with a ratio of peroxide ions to chlorine in the range of approximately 3.7 to 13. It is reasonable to expect that some clogging would occur under these conditions, and to expect that increasing the BHP flow rate by a factor of two for a given chlorine flow rate would reduce or eliminate the clogging. The occurrence of clogging in some conditions and not in others also means that some of the runs may be considered to be a better indication of clog-free operation than others. In general, the data that are taken towards the beginning of a given day's measurements, that are not accompanied by a rise in gas feed pressure for given mass flow rate, and that are taken at higher ratios of peroxide ion to chlorine are considered to be the most reliable data. When the fifteen runs were judged according to these criteria, the four runs that yielded unphysically high extrapolated values of $O_2(a)$ at the chip's outlet were found to suffer from minimal clogging. It is therefore expected that clogging will not provide an explanation for the observed discrepancy. In addition, the expected effect of clogging is not to increase the concentration of $O_2(a)$ at the chip's outlet, but rather to

decrease it. For a given mass flow rate set by the mass flow controllers, the effect of clogged channels like those shown in Figure 10 is to increase the gas and liquid velocities within the remaining channels. This reduces the reactants' residence time in the channels so that less $O_2(a)$ would be produced. Since the observed discrepancy is in the other direction (anomalously high concentrations), and since the runs with anomalously high concentrations are relatively free of clogging, clogging is rejected as an explanation for the observed discrepancy.

The second two potential sources of error (loss of $O_2(a)$ through the capillary separator and error in the pooling rate coefficients) were assessed by including them in a revised μ SOG model and assessing whether including these effects could remove the discrepancy. In order to ensure that clogging was not affecting the comparison between model and experiments, the comparison was made for the four runs that were deemed to be most free of clogging and for which the discrepancy was largest. Two revisions to the baseline model were necessary. A fluidic circuit analogy was used to estimate the percentage of gas that was sucked through the separator holes along with the liquid waste. The fluidic circuit assumes incompressible, fully developed flow in both the liquid and gas phases with a variable number of open holes N . The resulting loss of gas through the liquid separator is then accounted for in the calculation of the flow rates in the gas exit flow path. The model was also modified to account for the uncertainty of the pooling rate coefficients by making the effective pooling rate coefficient $2k_3+k_2$ (or equivalently, Θ) a variable parameter. In order to determine the best values for Θ and N , both parameters were varied independently and the sum of squared errors between the model's predicted concentrations at the measurement point and the measurements themselves were calculated for the four highest confidence runs. The best agreement between the kinetics model and the measured data, shown in Figure 11, occurred when $2k_3+k_2$ was set at 84.5% of the published value and gas leakage through the capillary separator was negligible. These corrected values for the rate coefficients fall within the error bars of the cited source reference for the kinetic constants [30]. Figure 12 shows a pronounced drop in the error as the scalar multiplier of Θ is

varied. This is not a unique minimization in the two dimensional (Θ , N) space. Similar minima are obtained for nonzero values of N , but they correspond to still smaller values of the pooling rate coefficient. The best agreement occurs (and minimum modification to $2k_3+k_2$ is necessary) when N approaches zero, suggesting that the occasional gas bubbles that were observed flowing through the separator's liquid outlet line had a negligible effect on the measurement. In other words, if significant $O_2(a)$ flow were sucked in by the separator, the flow velocity in the gas outlet would be still smaller. As a result, k_2 and k_3 would also need to be even smaller to give physically meaningful predictions at the chip's $O_2(a)$ outlet. However, it is possible to have a small $O_2(a)$ separator leak and still have pooling rate coefficient values that fall within the error bars of the reference and yield essentially the same minimum error.

As was described before, only a small fraction of the separator seems to be covered by the wetting front of the liquid by-products. Given the pressure difference applied across the capillary separator, even a small number of capillaries (5% of the total number) that were not filled with liquid would have been enough to suck in all the $O_2(a)$ and prevent any observation of $O_2(a)$ at the measurement point. The experimental performance suggests that the separator worked as designed, and the capillaries that didn't appear to be used during operation were nonetheless plugged with a stationary film of BHP that was put in place when BHP was first flowed through the chip. In all cases, the pressure difference across the separator is not enough to overcome the surface tension effects and clear the capillaries of liquid to allow for penetration of gas into the liquid exit flow.

The adjusted values for the pooling rate coefficients were used to calculate molar flow rates per unit of reactor volume and power in the $O_2(a)$ flow as well as yield-utilization product and $O_2(a)$ concentration at the chip's gas outlet. These values are also shown in Table III. The maximum yield-utilization product at the chip's gas outlet is determined to be 78% (+21% -43%). This is theoretically consistent with a chlorine utilization of 100% and a yield of 78%, a chlorine utilization of 78% and a yield of 100%, or anywhere between. The lack of quantitative mass spectrometer data makes independent determination of the yield

and chlorine utilization impossible. However, given that some pooling losses must have taken place between the end of the reaction channels and the chip's gas outlet, it is reasonable to conclude that this corresponds to a chlorine utilization of near 100% and a yield of about 78%. This yield is in line with state-of-the-art jet SOG generators, which have been reported to perform with yields as high as 73% [31][32]. High yield is particularly important in COIL reactors because some $O_2(a)$ is consumed in the dissociation of I_2 and, of the remainder, only $O_2(a)$ above the threshold yield of about 7% can contribute at all to laser output in a COIL system; incremental increases above the onset of lasing offer significant increases in power because of the dynamics of the COIL system.

A comparison of $O_2(a)$ molar flow rate per unit volume between the μ SOG and other technologies is given in Table IV. The maximum molar flow rate of $O_2(a)$ per unit reactor volume is about 670×10^{-4} mol/L/s. This value includes that part of the volume of the MEMS chip that hosts the manifolds, reaction channels, and capillary separator; it does not include any volume that is devoted solely to single-chip packaging or the volume that is devoted to chip cooling. This compares favorably with the molar flow rate of $O_2(a)$ per unit of internal reactor volume as reported for various types of published SOGs as reported in the literature. The molar flow rate per unit of internal reactor volume for modern jet SOGs is about 1300 - 1700×10^{-4} mol/l/sec [33][31], nearly three times as large as the molar flow rate per unit of reactor hardware volume reported here for the μ SOG chip. However, it should be noted that the μ SOG volume includes the bifurcated BHP inlet as well as some of the surrounding silicon, while the jet SOG values only take the internal reaction volume into account.

The power carried by the flow of $O_2(a)$ at the μ SOG's gas outlet may be estimated from the molar flow rate extrapolated to the gas outlet and the energy of the $O_2(a \rightarrow X)$ transition. The resulting values for power in the flow are reported in Table III. The maximum per chip power in the output flow is 1.37 W. However, only part of the power in the $O_2(a)$ flow would be converted to laser output power if μ SOG chips were used to drive a COIL system. Assuming a threshold yield of 7% and a typical COIL power extraction efficiency

of 80% [34], the power in each μ SOG's $O_2(a)$ flow is predicted to source about 1 W of laser output power when integrated into an appropriate COIL system. The original μ SOG study [3] proposed using arrays of microdevices to construct COIL systems with power levels ranging from several kW to 100 kW. In that study, each μ SOG chip was predicted to drive 2.3 W of this power output. The maximum power capability of 1.37 W per chip demonstrated in the present experiments is in agreement with the model predictions but is somewhat less than the optimum of 2.3 W per chip as identified in the initial modeling study. The difference between the predicted optimum performance and the performance demonstrated in the first μ SOG chips is not surprising given that the chips have not yet been operated at their optimum operating point because of flow limitations in the initial test rig. It is expected that the performance of the μ SOG chips will approach the predicted optimum performance more closely as they are demonstrated closer to their optimum operating point. In particular, it is expected that the output of $O_2(a)$ per chip will increase and that clogging will decrease when the chips are operated at higher BHP and chlorine flow rates and at higher BHP to chlorine ratios.

VIII. CONCLUSIONS

Generation of $O_2(a)$ using a MEMS singlet oxygen generator has been successfully demonstrated. The devices were tested over a range of operating points, resulting in $O_2(a)$ molar flow rates in excess of 600 mol/l/s and a yield-utilization product approaching 80%. On both of these crucial metrics, the μ SOG showed performance that compares favorably with the macro-scaled SOGs that are described in the published literature. Future work includes testing multiple μ SOGs in tandem at their optimal operating conditions and using arrays of μ SOGs to drive a MEMS COIL system.

IX. ACKNOWLEDGEMENTS

The authors acknowledge J. Letendre for his expertise in building the experimental apparatus and D. Park for help with the images. The Tactical Technology Office at DARPA, the Missile Defense Agency (MDA),

and the Air Force Research Laboratory (AFRL) generously provided funding for this research (DARPA Order No. T171/00, Program Code: 4G10; Issued by DARPA/CMO under Contract No. MDA972-04-C-0140). The views and conclusions contained in this document are those of the authors and should not be interpreted as representing the official policies, either expressed or implied, of the Defense Advanced Research Projects Agency or the U.S. Government.

REFERENCES

- [1] G. Ruiz-Ibanez and O. Sandall, "Kinetics for Reactions between Chlorine and Basic Hydrogen Peroxide," *Ind. Eng. Chem. Res.*, 1991, 30, 1105-1110.
- [2] S. C. Tidwell et al., "Scaling CW Diode-End-Pumped Nd:YAG Lasers to High Average Powers," *IEEE J. Quantum Electronics*, vol. 24(4), 1992.
- [3] B. A. Wilhite et al., "Design of a MEMS-Based microChemical Oxygen-Iodine Laser (μ COIL) System," *IEEE J. Quantum Electronics*, vol. 40(8), pp. 1041-1055, 2004.
- [4] L. F. Velásquez-García, T. F. Hill, B. A. Wilhite, K. F. Jensen, A. H. Epstein, and C. Livermore, "A MEMS Singlet Oxygen Generator – Part I: Device Fabrication and Proof of Concept Demonstration", submitted to the *Journal of MicroElectroMechanical Systems*
- [5] T. F. Hill, L. F. Velasquez-Garcia, B. A. Wilhite, A. H. Epstein, K. F. Jensen, and C. Livermore, "A MEMS Singlet Oxygen Generator", Technical Digest of the Solid-State Sensor, Actuator and Microsystems Workshop, pp 114 – 119, Hilton Head Island, South Carolina, June 4 – 8th 2006
- [6] W. E. McDermott et al., "An electronic transition chemical laser," *Appl. Phys. Lett.*, 32(8), 1978.
- [7] J. F. Hon, D. N. Plummer, P. G. Crowell, J. Erkkila, G. D. Hager, C. Helms, and K. Truesdell, "A Heuristic Method for Evaluating COIL Performance," *AIAA Journal*, vol.34 no.8, pp 1595-1603, 1996.
- [8] S. J. Arnold et al., "Some New Emission Bands of Molecular Oxygen," *Journal of Chemical Physics*, 40(6), pp 1769-1770, 1964.
- [9] D.J. Bernard and N.R. Pchelkin, "Measurement of $O_2(^1\Delta)$ content in the gaseous effluents of a chemical generator," *Rev. Sci. Instrum.* 49, 794 (1978).
- [10] W. T. Rawlins, S. Lee, W.J. Kessler, and S. J. Davis, "Observations of Gain on the $I(^2P_{1/2} \rightarrow ^2P_{3/2})$ Transition by Energy Transfer from $O_2(a^1\Delta_g)$ Generated by a Microwave Discharge in a Subsonic Flow Reactor," *Appl. Phys. Lett.* 86, 051105 (2005).
- [11] G. Watanabe et al., "Modeling of crossflow jet-type singlet oxygen generator," *Journal of Applied Physics* 97, 114905 (2005).
- [12] D. A. Copeland et al., "Two-Phase Model of $O_2(^1\Delta)$ Production with Application to Rotating Disk Generators," In *Proc. SPIE*, vol 1871, pp. 203-228.
- [13] M. V. Zagidullin et al., "Highly efficient jet $O_2(^1\Delta)$ generator," *Sov. J. Quantum Elecron.*, 21 (7), 1991.
- [14] P. V. Avizonis and K. A. Truesdell, "The Chemical Oxygen-Iodine Laser (COIL)," In *Proc. SPIE*, vol. 2502.

- [15] W. J. Thayer, A. K. Cousins, R. D. Romea, "Modeling of Uniform Droplet Singlet Oxygen Generators," SPIE vol. 2117, 1994.
- [16] B. D. Barmashenko and S. Rosenwaks, "Theoretical modeling of chemical generators producing $O_2(^1\Delta)$ at high pressure for chemically pumped iodine lasers," *J. Appl. Phys.*, 73 (4), 1993.
- [17] D. A. Copeland et al., "Exact and Approximate Solutions of the Utilization and Yield Equations for $O_2(^1\Delta)$ Generators," SPIE vol. 2119.
- [18] R. J. Richardson, C. E. Wiswall, P. A. G. Carr, F. E. Hovis, and H. V. Lilenfeld, *J. Appl. Phys.*, 52, 4962 (1981).
- [19] G. Ruiz-Ibanez et al., *J. Chem. Eng. Data.*, 36, 459 (1991).
- [20] N. G. Basov, M. V. Zagidullin, V. I. Igoshin, V. A. Katulin, and N. L. Kupriyanov, *Chemical Lasers* (Springer, Berlin, 1990).
- [21] O. Aharon, A. Elior, M. Herskowitz, E. Lebiush, and S. Rosenwaks, *J. Appl. Phys.* 70, 5211 (1991).
- [22] Ergun, S., "Fluid Flow Through Packed Columns," *Chem. Eng. Progress*, 48, 89-94 (1952).
- [23] V. V. Bashkin et al., "Investigation of physical properties of basic hydrogen peroxide solutions for use in singlet oxygen generators," SPIE vol. 3574.
- [24] A. Gunther et al., "Micromixing of Miscible Liquids in Segmented Gas-Liquid Flow," *Langmuir*, 21 (4), 1547-1555, 2005.
- [25] J. G. Kralj, H. R. Sahoo, and K. F. Jensen, "Integrated continuous microfluidic liquid-liquid extraction," *Lab on a Chip*, 2007, DOI:10.1039/b610888a.
- [26] V. L. Streeter, E. B. Wylie, and K. W. Bedford, "Fluid Mechanics", Ninth Edition, McGraw-Hill, 1998.
- [27] C. M. Bender and S. A. Orszag, "Advanced Mathematical Methods for Scientists and Engineers", Springer, 1999.
- [28] S.M. Newman et al., "Integrated absorption intensity and Einstein coefficients for the $O_2(a^1\Delta_g) - (X^3\Sigma_g^-) (0,0)$ transition: A comparison of cavity ringdown and high resolution Fourier transform spectroscopy with a long-path absorption cell," *J. Chem. Phys.* 110, 10749 (1999).
- [29] W.J. Lafferty et al., "Rotational line strengths and self-pressure-broadening coefficients for the 1.27- μm , $a^1\Delta_g-X^3\Sigma_g^-$, $v = 0-0$ band of O_2 " *Appl. Opt.* 37, 2264 (1998).
- [30] H. V. Lilenfeld, "Oxygen-iodine laser kinetics," AFWL-TR-83-01, Air. Force Research Laboratory, Kirtland Air Force Base, NM, 1983.
- [31] V. Rybalkin et al., "Parametric study of a highly efficient chemical oxygen-iodine laser with supersonic mixing of iodine and oxygen," *Journal of Applied Physics*, 98, 0213106 (2005).
- [32] S. C. Hurlock, "COIL technology development at Boeing," SPIE vol. 4631.
- [33] M. V. Zagidullin et al., "Highly efficient supersonic chemical oxygen-iodine laser with a chlorine flow rate of 10 mmol s^{-1} ," *Soviet Journal of Quantum Electronics*, 27(3), 1997.
- [34] G.P. Perram and G.D. Hager, "The Standard Chemical Oxygen-Iodine Laser Kinetic Package," AFWL-TR-88-50 (1988).
- [35] K. R. Kendrick et al., "Determination of Singlet-Oxygen Generator Efficiency on a 10-kW Class Supersonic Chemical Oxygen-Iodine Laser (RADICL)," *IEEE J. Quantum Electronics*, vol. 35(12), 1999.
- [36] G. R. Kwirandt and W. O. Schall, "Basic experiments on the production of $O_2(^1\Delta)$," In *Proc. SPIE*, vol. 2502, 1995, pp. 331-337.

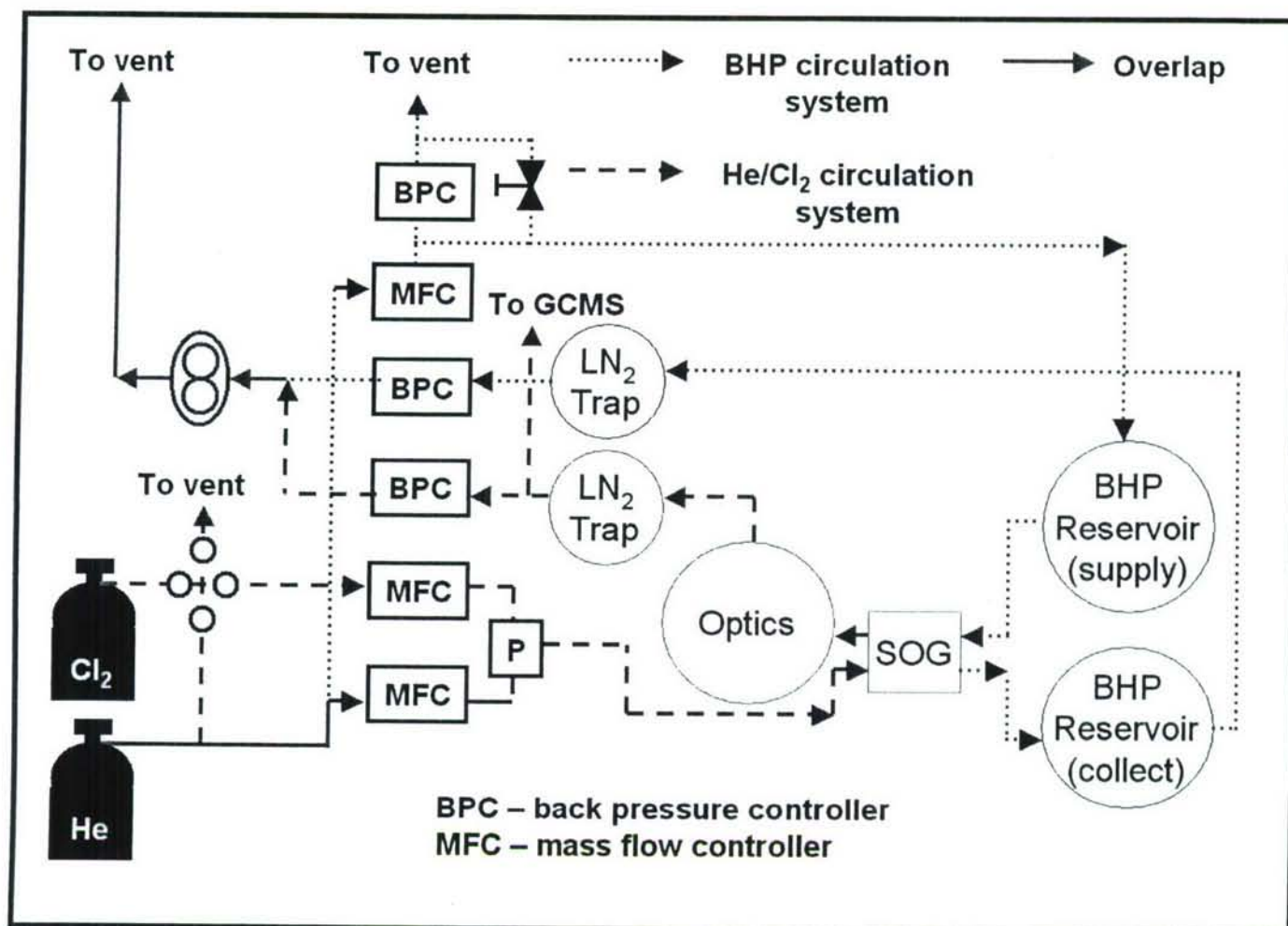


Figure 1 – Schematic diagram of μSOG testing rig.

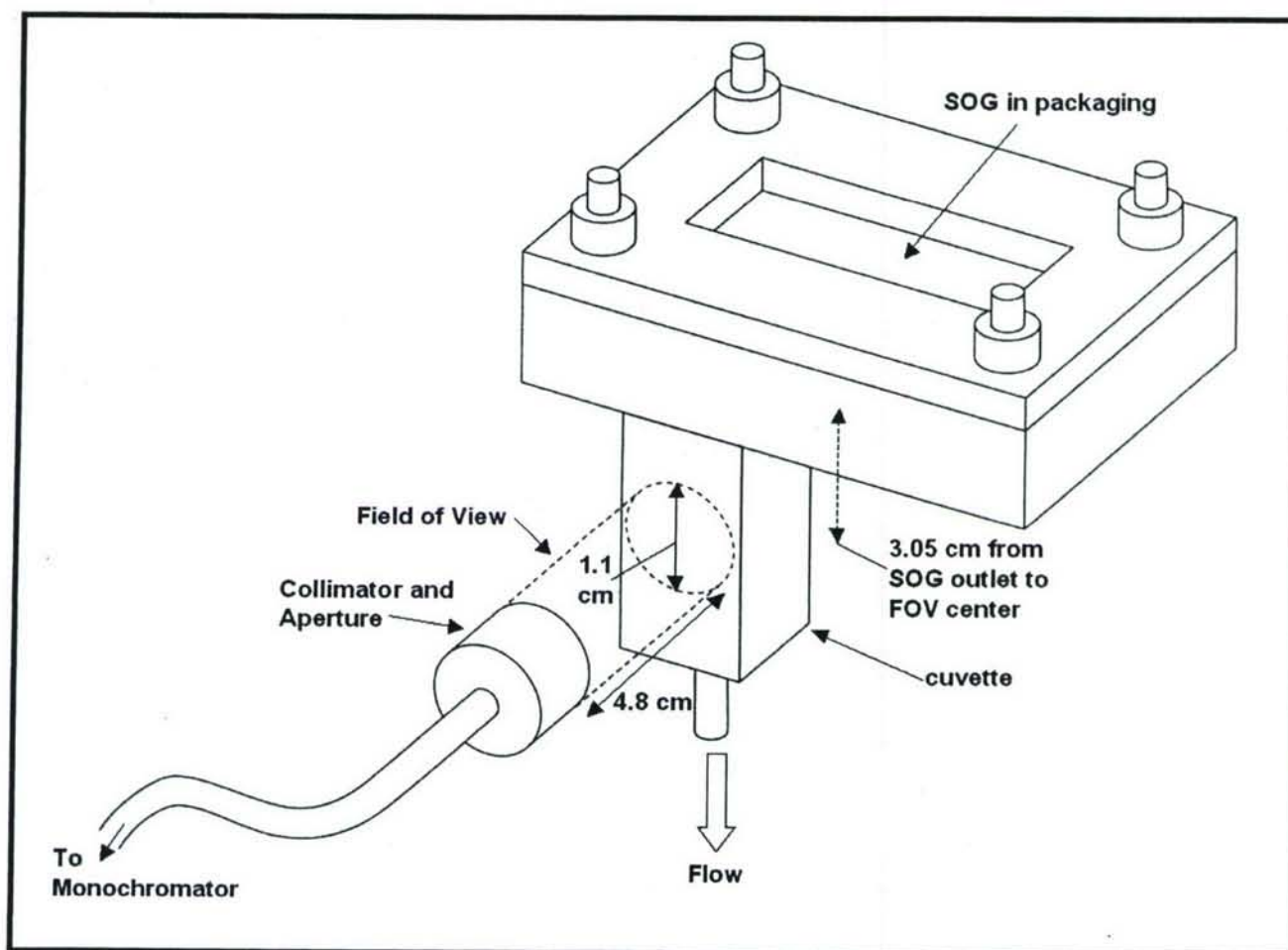


Figure 2 – Schematic of emission measurement set up.

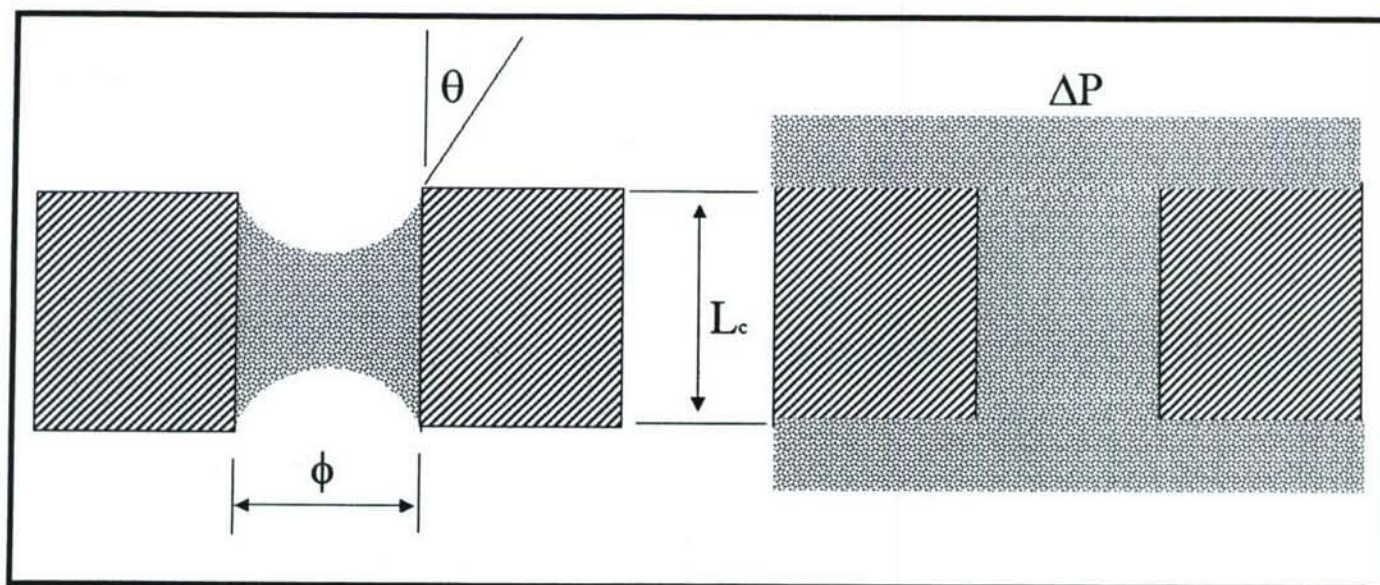


Figure 3 – Illustration of capillary pores with non-zero (left) and zero wetting angles (right). When fully filled-in, the capillaries are not surface tension driven, but pressure driven.

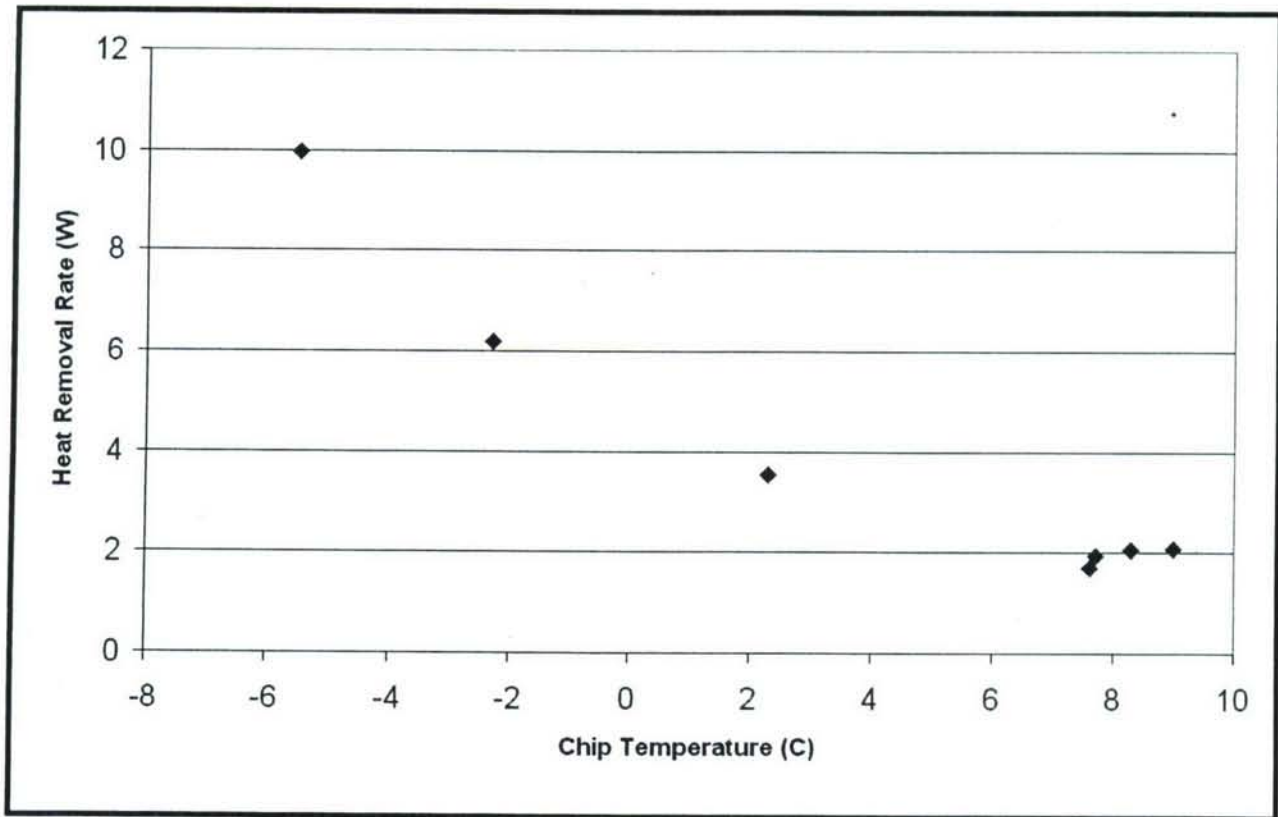


Figure 4 – Measured heat removal capacity of the micro-fabricated heat exchanger vs. internal chip temperature. For these data, the heat source was provided by the ambient surrounding the chip package.

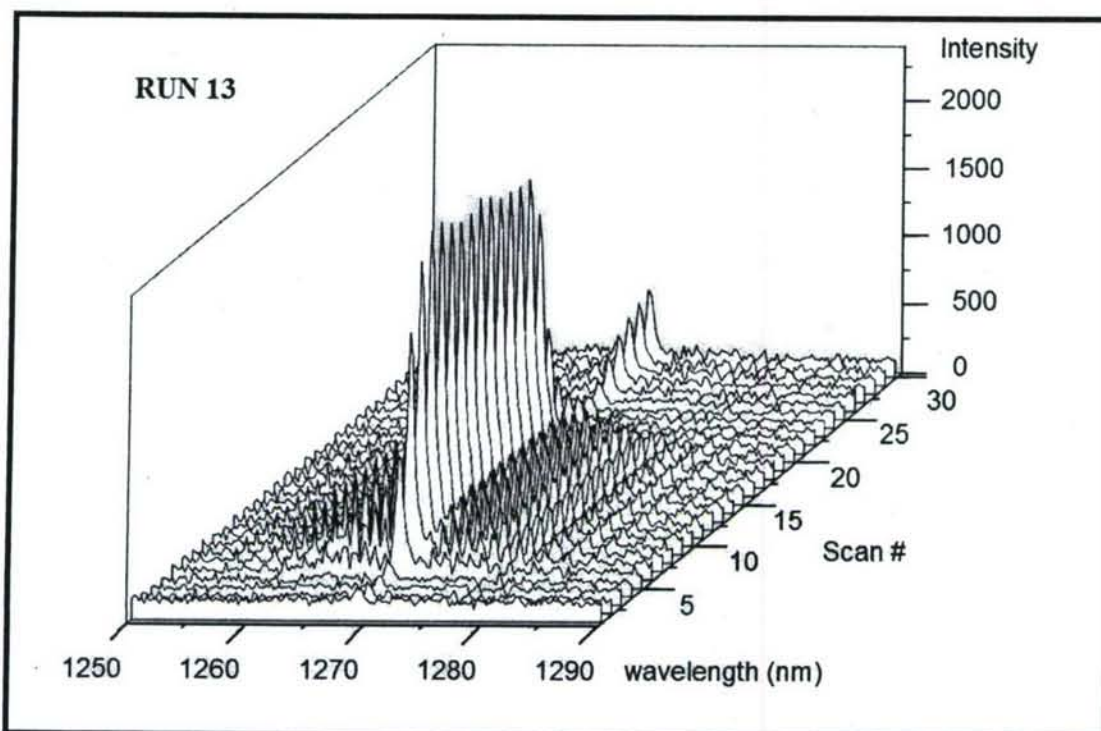


Figure 5 – IR Emission spectra from the μ SOG versus time for a single 1-min chlorine pulse.

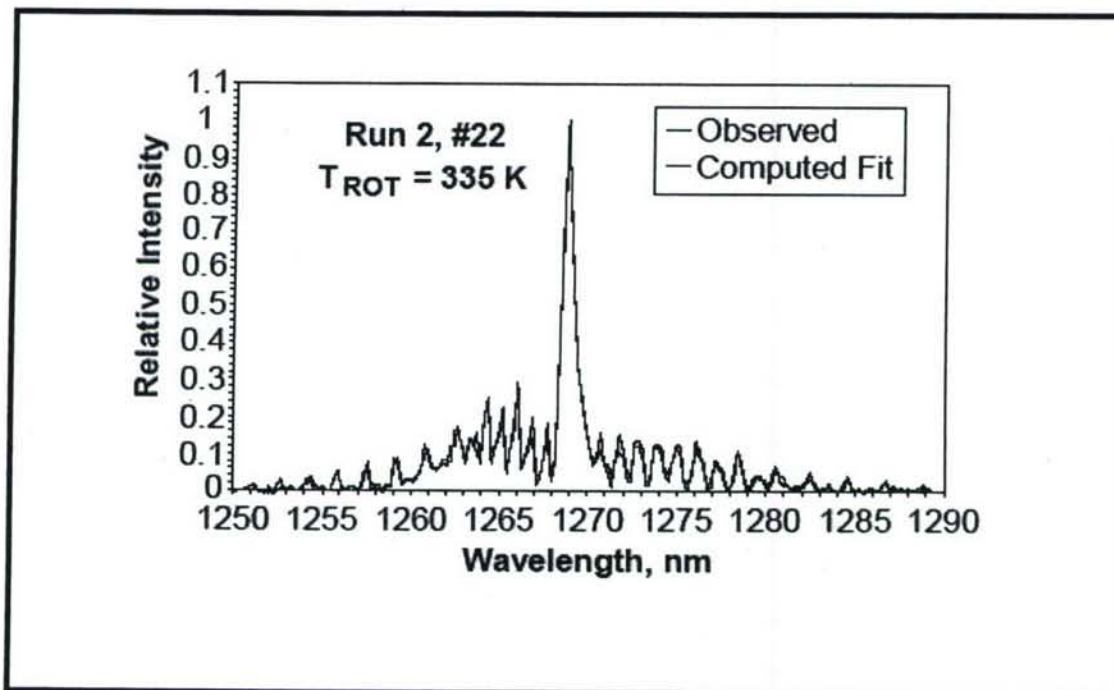


Figure 6 – Typical IR spectra for a 5-second integration time. A least-squares fit was used to calculate the $O_2(a)$ temperature. The typical temperature falls in the 295 to 335 K range, in contrast with the sub-zero temperature of the chip.

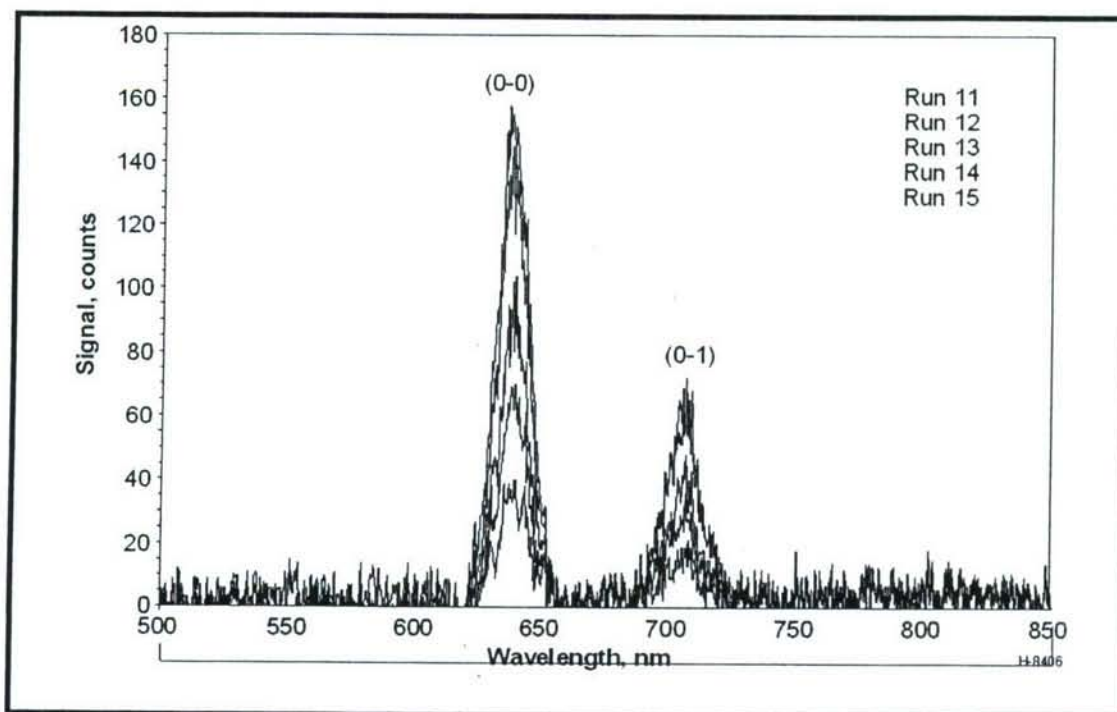


Figure 7 – Spectra resulting from dimol emission

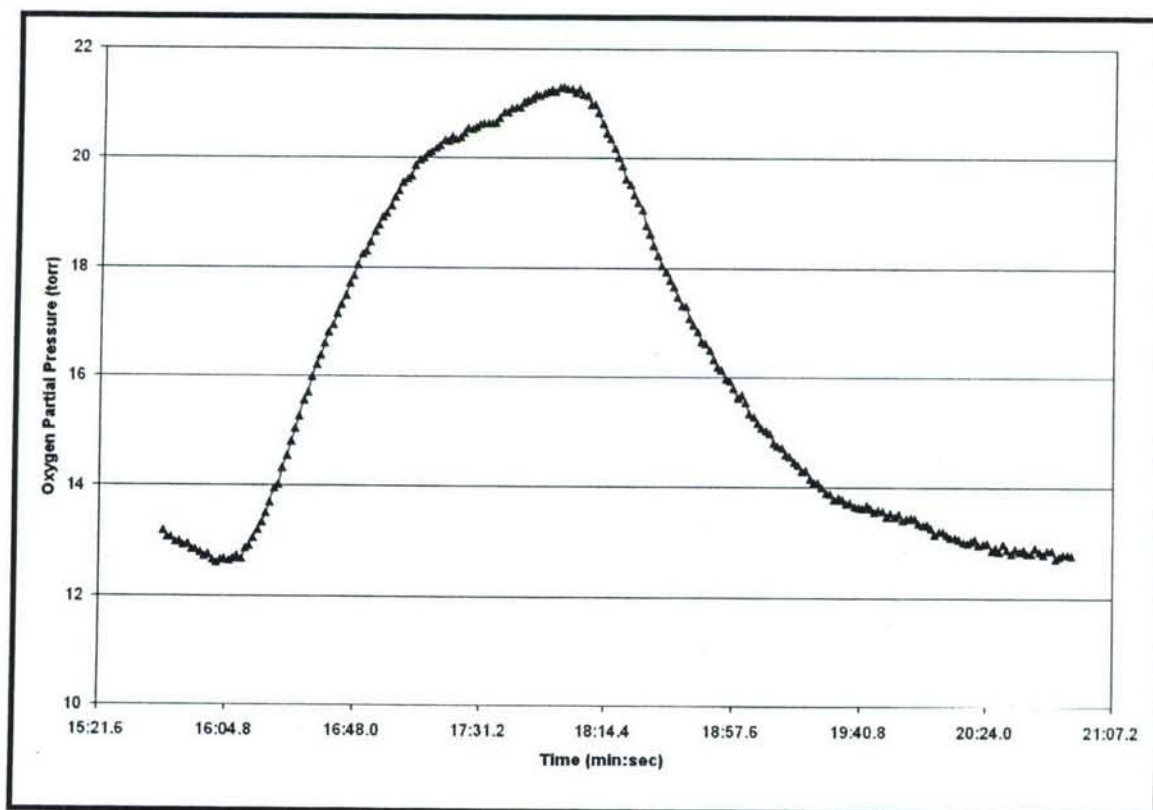


Figure 8 – Typical mass spectrometer data for a 2 minute chlorine pulse run.

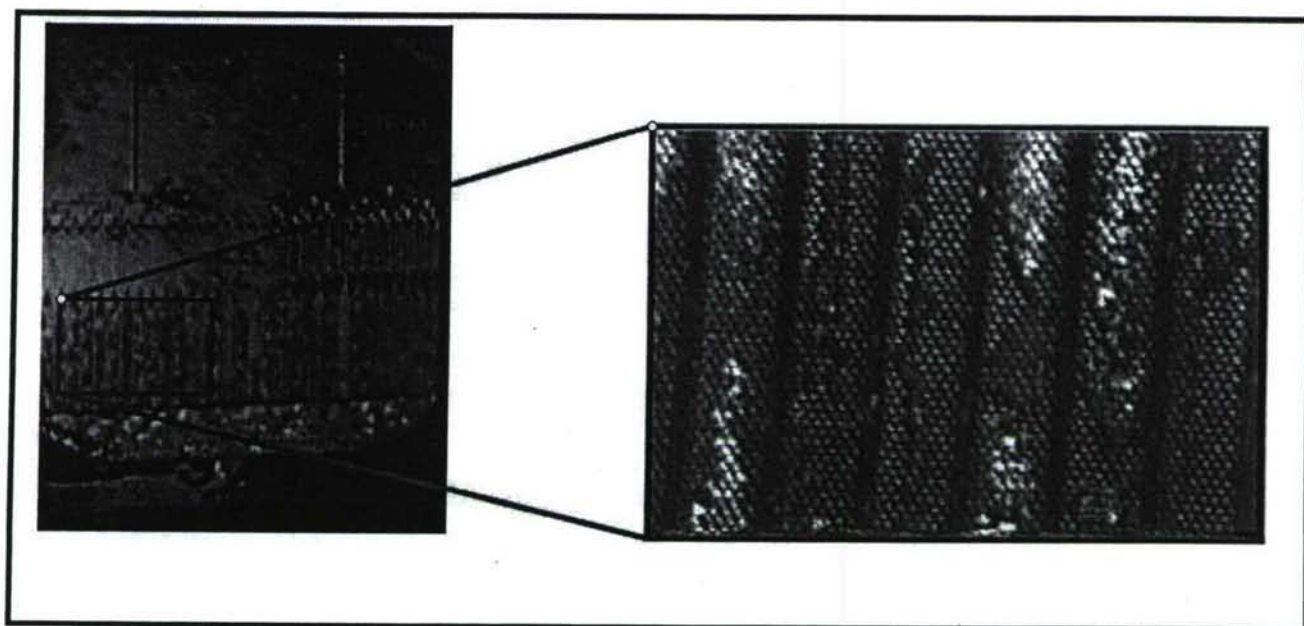


Figure 9 – Trickling flow was observed in the reaction channels.

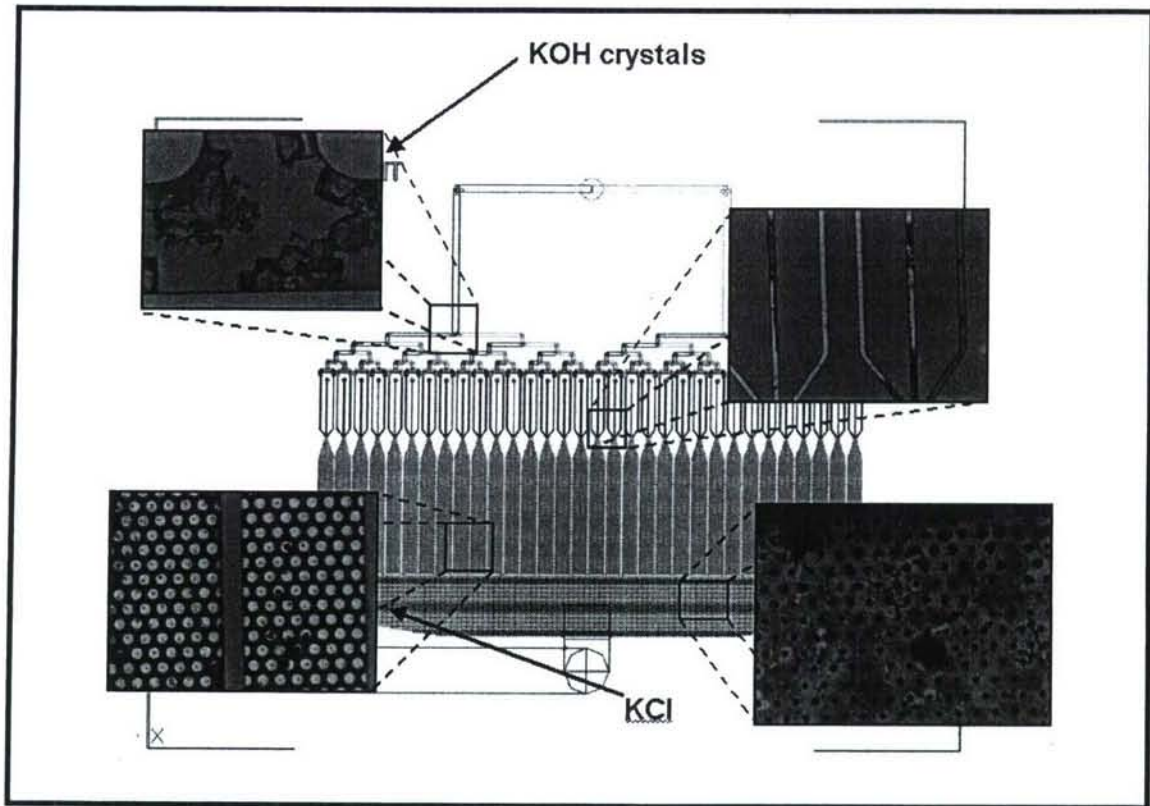


Figure 10 – SOG diagram overlaid with optical microscope images showing clogging due to KOH precipitation (top) and KCl clogging (bottom).

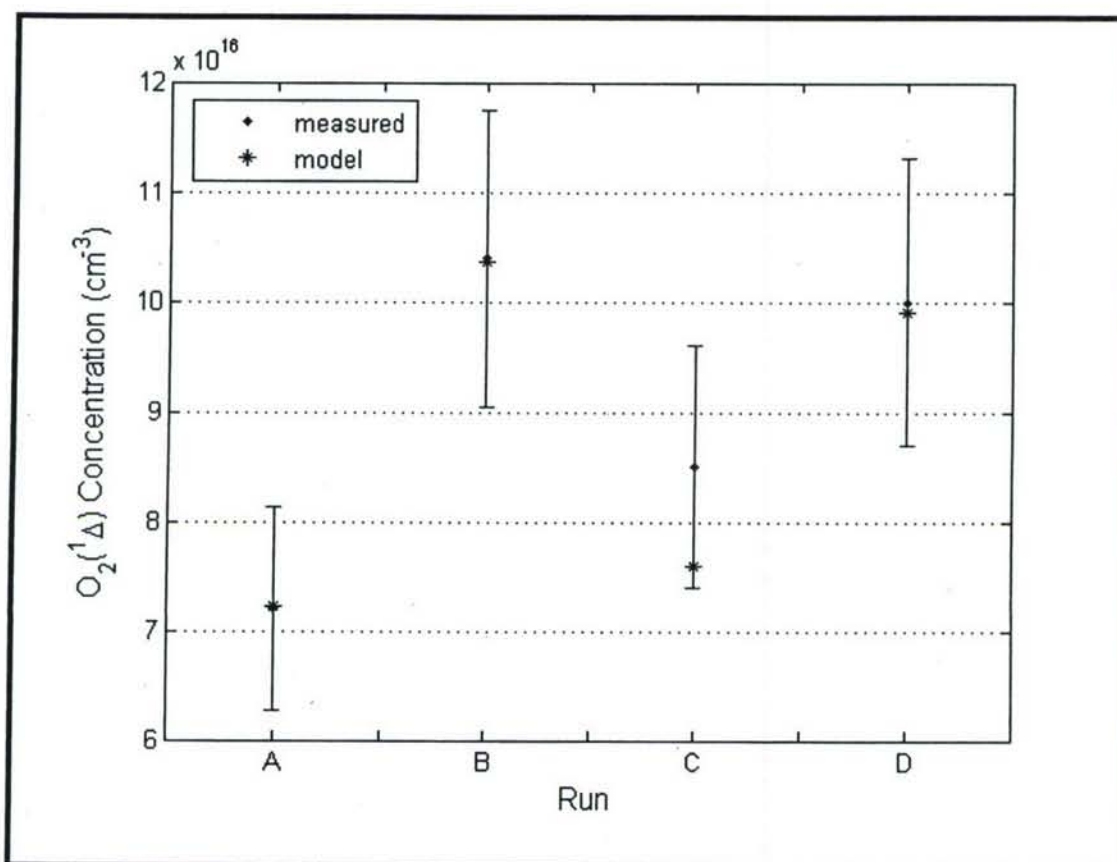


Figure 11 – Model fit for highest confidence runs. Best agreement between measured and predicted yield-utilization product at measurement point occurs when the pooling coefficient is scaled by 0.845.

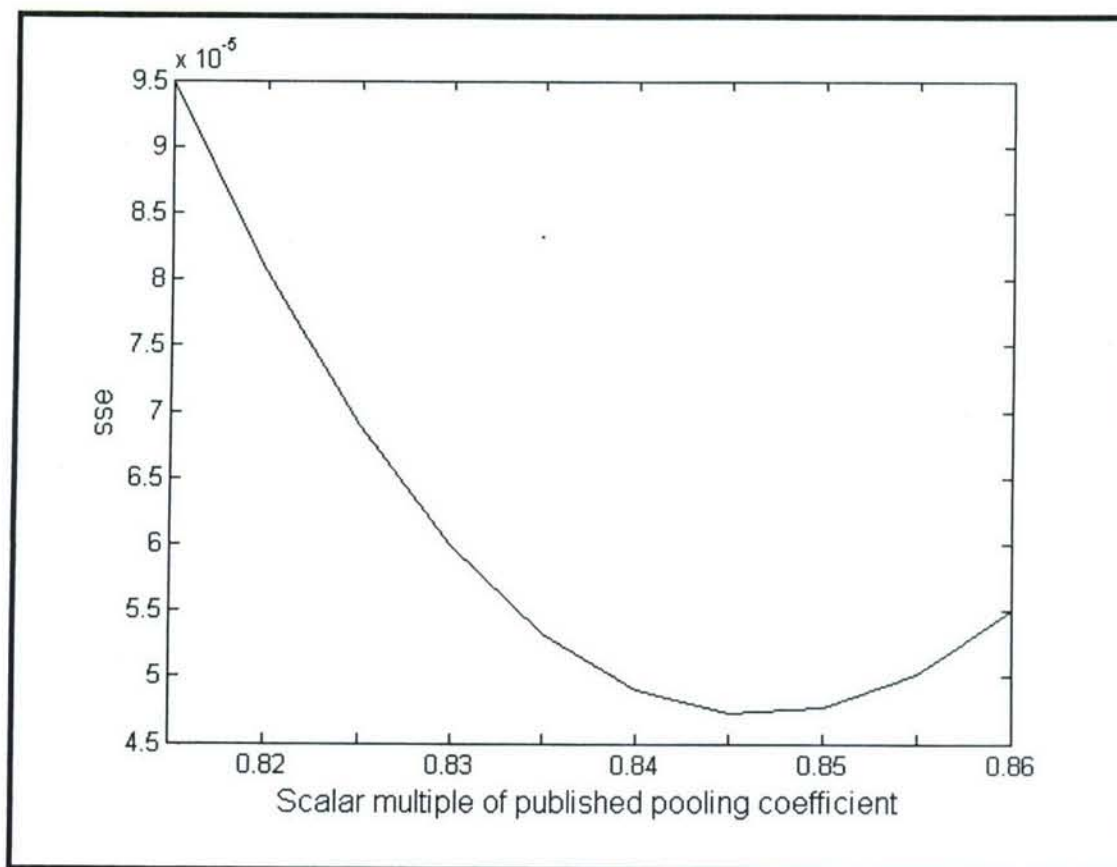


Figure 12 – Minimum square error sum vs. scalar multiple of Θ for the data set with the highest confidence level. There is a range of possible kinetic constants and $O_2(a)$ separator leak that yield equivalent minimum error, but all combinations point towards small $O_2(a)$ bleed.

#	Expression	Rate Coefficient
R1	$\text{H}_2\text{O}_{2(l)} + 2\text{KOH}_{(l)} + \text{Cl}_{2(g)} \longrightarrow 2\text{H}_2\text{O}_{2(l)} + 2\text{KCl}_{(l)} + \text{O}_2(^1\Delta)_{(g)}$	n.a.
R1a	$\text{OH}^\cdot + \text{H}_2\text{O}_2 \longrightarrow \text{O}_2\text{H}^\cdot + \text{H}_2\text{O}$	$K_{eq} > 10^4$
R1b	$\text{O}_2\text{H}^\cdot + \text{Cl}_2 \longrightarrow \text{HOOCI} + \text{Cl}^\cdot$	$k_1 = 2.7 \times 10^{10} \text{ cm}^3/\text{mol/s}$
R1c	$\text{O}_2\text{H}^\cdot + \text{HOOCI} \longrightarrow \text{ClO}_2^\cdot + \text{H}_2\text{O}_2$	$K = \text{infinity}$
R1d	$\text{ClO}_2^\cdot \longrightarrow \text{Cl}^\cdot + \text{O}_2(a)$	$K = \text{infinity}$
R1e	$\text{O}_2(a) \longrightarrow \text{O}_2(X)$	$K = 5 \times 10^5 \text{ s}^{-1}$
R2	$\text{O}_2(a) + \text{O}_2(a) \longrightarrow \text{O}_2(b) + \text{O}_2(X)$	$k_2 = 1.63 \times 10^7 \text{ cm}^3/\text{mol/s}$
R3	$\text{O}_2(a) + \text{O}_2(a) \longrightarrow \text{O}_2(X) + \text{O}_2(X)$	$k_3 = 1.02 \times 10^7 \text{ cm}^3/\text{mol/s}$
R4	$\text{O}_2(a) + \text{O}_2(X) \longrightarrow \text{O}_2(a) + \text{O}_2(X)$	$k_4 = 2.35 \times 10^7 \text{ cm}^3/\text{mol/s}$
R5	$\text{O}_2(b) + \text{H}_2\text{O} \longrightarrow \text{O}_2(a) + \text{H}_2\text{O}$	$k_5 = 4.03 \times 10^{12} \text{ cm}^3/\text{mol/s}$
R6	$\text{O}_2(b) + \text{Cl}_2 \longrightarrow \text{O}_2(a) + \text{Cl}_2$	$k_6 = 9.03 \times 10^8 \text{ cm}^3/\text{mol/s}$
R7	$\text{O}_2(b) + \text{H}_2\text{O}_2 \longrightarrow \text{O}_2(a) + \text{H}_2\text{O}_2$	$k_7 = 1.99 \times 10^{11} \text{ cm}^3/\text{mol/s}$
R8	$\text{O}_2(b) + \text{He} \longrightarrow \text{O}_2(a) + \text{He}$	$k_8 = 6.02 \times 10^6 \text{ cm}^3/\text{mol/s}$
R9	$\text{O}_2(a) + \text{O}_2(X) \longrightarrow \text{O}_2(X) + \text{O}_2(X)$	$k_9 = 9.64 \times 10^5 \text{ cm}^3/\text{mol/s}$
R10	$\text{O}_2(a) + \text{H}_2\text{O} \longrightarrow \text{O}_2(X) + \text{H}_2\text{O}$	$k_{10} = 2.41 \times 10^6 \text{ cm}^3/\text{mol/s}$
R11	$\text{O}_2(a) + \text{Cl}_2 \longrightarrow \text{O}_2(X) + \text{Cl}_2$	$k_{11} = 3.61 \times 10^6 \text{ cm}^3/\text{mol/s}$
R12	$\text{O}_2(a) + \text{He} \longrightarrow \text{O}_2(X) + \text{He}$	$k_{12} = 4.82 \times 10^3 \text{ cm}^3/\text{mol/s}$

Table I – Chemical reactions describing the μSOG dynamics

	SOG Parameters used in Willhite et al.	Updated SOG Parameters
Cl ₂ Viscosity (g/cm/s)	$2 \times 10^{-4} \text{ g/cm/s}$	$2 \times 10^{-4} \text{ g/cm/s}$
BHP Viscosity (g/cm/s)	$1 \times 10^{-2} \text{ g/cm/s}$	$1.8 \times 10^{-2} \text{ g/cm/s}$
BHP Density (g/cm ³)	1.373 g/cm^3	0.983 g/cm^3
Packing Diameter (cm)	$7 \times 10^{-3} \text{ cm}$	$7 \times 10^{-3} \text{ cm}$
Void fraction of packed-bed	0.40	0.45
Reaction Length (cm)	0.516	0.6

Table II – Changes between original model and actual μSOG geometry

Table III - Summary of μ SOG Measurements

Run	He, (sccm)	Cl ₂ , (sccm)	BHP Flow Rate (cm ³ /s ec)	P _{plenum} , (torr)	O ₂ (¹ Δ) Tem p., (K)	Measur ed conc., ($\times 10^{17}$ cm ⁻³) (+/- 13%)	Meas ured yield- utiliz ation prod uct	Extrapolate d initial conc., ($\times 10^{17}$ cm ⁻³)	Extrapolate d initial yield- utilization product	Predict ed initial yield- utilizati on product	Extrapolate d Power, (W)	Molar Flow rate, ($\times 10^{-4}$ mol s ⁻¹ L ⁻¹)
1	37	13	0.95	100	330	0.72	0.095	5.13 +2.19/-2.65	0.7011 +0.3/-0.36	0.7057	0.615 +0.3/-0.32	299 +144.7/- 154
2	56.75	18.7 5	1.32	100	335	1.04	0.144	5.64 +1.57/-2.52	0.78 +0.22/-0.35	0.7674	1.02 +0.29/-0.46	500 +140/- 224
3	75	25	1.31	100	335	0.95	0.132	2.15 +0.76/-0.54	0.2987 +0.105/- 0.08	0.7991	0.52 +0.19/- 0.132	255 +90/- 64
4	37	13	0.95	100	330	0.76	0.10	≥ 3.14	> 0.4292	0.7057	≥ 0.376	> 183
5	56.75	18.7 5	1.32	100	320	0.72	0.096	1.76 +0.69/-0.47	0.23 +0.091/- 0.062	0.7628	0.306 +0.12/-0.08	149 +58/- 40
6	75	25	1.29	200	325	0.85	0.057	≥ 7.14	> 0.4809	0.6295	≥ 0.843	> 410
7	75	25	1.30	150	335	1	0.091	8.48 +2.33/-4.74	0.7845 +0.2155/- 0.4385	0.7225	1.37 +0.379/- 0.769	669 +184/- 374
8	93.75	31.2 5	1.30	100	333	0.92	0.126	1.63 +0.42/-0.34	0.2248 +0.0575/- 0.0470	0.8154	0.494 +0.125/- 0.102	240 +61/- 50
9	112.5	37.5	1.29	100	310	0.77	0.099	1.14 +0.24/-0.21	0.1468 +0.0302/- 0.0266	0.8185	0.387 +0.08/-0.07	188 +39/- 34
10	131.25	43.7 5	1.29	100	305	0.77	0.097	1.08 +0.21/-0.19	0.1359 +0.0260/- 0.0235	0.82	0.418 +0.08/- 0.072	203 +39/- 35
11	125	25	1.29	100	300	0.86	0.159	1.38 +0.31/-0.27	0.2566 +0.0581/- 0.0496	0.8568	0.451 +0.102/- 0.09	219 +50/- 42
12	175	25	1.28	100	285	0.7	0.167	0.92 +0.17/-0.15	0.2180 +0.039/- 0.0359	0.8771	0.383 +0.067/- 0.064	186 +33/- 31
13	75	25	1.32	50	300	0.9	0.225	1.28 +0.25/-0.22	0.3175 +0.062/- 0.056	0.8487	0.558 +0.109/- 0.097	271 +53/- 47
14	75	25	1.32	50	298	0.95	0.232	1.39 +0.28/-0.25	0.342 +0.068/- 0.061	0.8485	0.601 +0.121/- 0.107	292 +59/- 52
15	37	13	1.34	50	295	0.5	0.116	0.75 +0.16/-0.14	0.1835 +0.383/- 0.034	0.8039	0.160 +0.32/-0.03	78 +16/-14

SOG Type	Molar Flowrate (mol s ⁻¹ L ⁻¹) $\times 10^{-4}$
Sparger	2.3
Disk-Type	87
Jet-Type [Zagidullin]	1670
Jet-Type [Rybalkin]	1323
μ SOG (this work)	669

Table IV – Comparison of present work with other reported SOG technologies ([31],[33],[35],[36]).

Design of a Silicon-Based Microscale Trickle-Bed System for Singlet-Oxygen Production

Benjamin A. Wilhite^{1*#}, Tyrone F. Hill², Luis Fernando Velasquez-Garcia³, Alan H. Epstein⁴,
Klavs F. Jensen^{1*}, and Carol Livermore^{5*}

¹Department of Chemical Engineering,

²Department of Electrical Engineering and Computer Science,

³Microsystems Technologies Laboratories,

⁴Department of Aeronautics and Astronautics,

⁵Department of Mechanical Engineering,

Massachusetts Institute of Technology, Cambridge, MA 02139

*Authors to whom correspondence should be addressed

#present address: Department of Chemical, Materials and Biomolecular Engineering,

University of Connecticut, Storrs, CT 06269-3222

Keywords: Microreactor; Gas-Liquid Reactor; Trickle-Bed; Singlet-Oxygen

ABSTRACT

Design methodology and flow characterization of a miniaturized trickle-bed system for singlet-oxygen production via exothermic reaction of chlorine gas and basic hydrogen peroxide (BHP) aqueous solution are reported. Miniaturized singlet oxygen production is accomplished by integration of several components developed for microsystems (uniform phase distributors, integrated on-chip cooling, and capillary-based phase separation) within a single device. Macroscale design equations for pressure-drop and heat-transfer rates are verified experimentally in the miniature trickle-bed reactor. Flow regime data from the present study are summarized with previous reports in microdevices and compared to conventional multiphase flow maps; these maps are found to be incapable of accurately predicting flow regime trends within the miniaturized trickle-bed system. Operation of the silicon-based miniaturized trickle-bed reactor achieved estimated singlet-oxygen yields of 78%, comparing well with reactor model predictions.

Topical Heading: **5. Reactors, Kinetics, and Catalysis**

INTRODUCTION

Microchemical systems have emerged as promising alternatives to conventional, macroscale systems for applications ranging from chemical analysis [1,2] and biological assays [3] to portable power systems [4] and small scale [5-8] and industrial-scale manufacture [9,10]. Process miniaturization, and the resulting reduction of characteristic length scales (e.g. hydraulic diameter, wall thickness, catalyst size), yields order-of-magnitude increases in momentum, heat and mass transport rates, alongside equivalent gains in system safety, redundancy and efficiency.

Fabrication of microchemical reactors via techniques developed for the integrated circuit (IC) and microelectromechanical systems (MEMS) industries allows the use of silicon-based materials for high-temperature applications and handling of aggressive chemistries. [11] Single crystal silicon is a strong, low-density material with a thermal conductivity comparable to that of brass, allowing production of low-weight, rapidly cooled or heated chemical reactors capable of operating under isothermal conditions. The chemical resistance of silicon can be easily augmented via thermally-grown coatings of silicon dioxide [12], chemical-vapor deposition of silicon nitride [13] or physical deposition of silicon carbide or nickel [14,15].

The precision and complexity enabled by 2-D photolithography methods has been employed for integration of (i) several parallel microfluidic networks [16], (ii) in-situ flow sensing with chemical reaction [17], and (iii) multiple separate yet coupled reacting fluids for heat-integration [18]. Additionally, microdevices combining chemical reaction with subsequent phase separations have been recently demonstrated for gas-liquid and liquid-liquid systems [19]. Recently, we completed the design and demonstration of a silicon-based micromachined device integrating (i) gas-liquid packed-bed microreactors with (ii) subsequent gas-liquid product separation and (iii) on-chip cooling, for producing singlet-delta oxygen [$\text{O}_2(^1\Delta)$] via exothermic

reaction of concentrated alkaline hydrogen peroxide solution and chlorine gas. The corrosive and unstable nature of the reagents, reaction exothermicity and required interfacial areas made this transport-limited multiphase reaction an ideal candidate for complete process miniaturization. The resulting microdevice represents a fully miniaturized, self-contained, industrial trickle-bed reactor, requiring only external fluidic connections for operation.

This manuscript reports the design methodology employed to realize the first fully-integrated miniaturized trickle-bed reactor system, including discussion of design equations selected to specify dimensions of each device component (inlet bifurcation and distributor, packed-bed channels, gas-liquid separator and cooling system) and subsequent characterization of the fabricated device components to verify the design methodology. In doing so, we expand upon previous reports on the microscale singlet-oxygen generator, which focused upon modeling analysis of the packed-bed reaction microchannels [20], device fabrication and packaging [13] and IR-spectroscopic analysis of singlet-oxygen production over a range of operating conditions [21]. The case study for integrated gas-liquid microreactor design presented here demonstrates a useful design methodology for creating integrated microreactor systems for multiphase chemical applications.

Applications for Singlet-Delta Oxygen

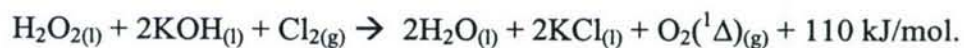
Singlet-delta oxygen is a spin-excited molecule in which the number of valence electrons in each spin-state is balanced, resulting in an energy difference of 94.1 kJ/mol between the excited singlet-delta and ground states [22]. This additional energy content of singlet-delta oxygen makes it a valuable reagent for multiple chemical processes, including endoperoxide formation for organic synthesis [23] and photodynamic cancer therapies [24]. The most demanding use of singlet-delta oxygen is as a pumping medium for iodine-based flowing gas

lasers, where high-energy laser outputs necessitate efficient generation of singlet-delta oxygen at maximum yields.

The Chemical-Oxygen Iodine Laser (COIL) has emerged as a promising alternative to carbon dioxide lasers [25,26] for applications ranging from automobile manufacture [27] to automated decontamination and decommissioning (D&D) of nuclear reactors [28], owing to its improved power outputs, wavelength characteristics, compatibility with glass optics and scalability from outputs of 1 kW to in excess of 1 MW [29, 30]. The COIL system is comprised of a chemical reactor for generating singlet-delta oxygen, followed by a supersonic nozzle for rapid introduction and cooling of the iodine lasing medium, followed by the optical cavity and downstream pressure recovery (pumping) system. Complete details of a proposed fully miniaturized COIL system (the MIT μ COIL) are given elsewhere [20]. The primary challenge in the design and operation of the overall COIL system is the safe and reliable production of singlet-delta oxygen in sufficient quantity and quality in a compact, lightweight reactor.

Challenges to Singlet-Delta Oxygen Production

While a variety of reaction schemes for chemical generation of singlet-delta oxygen exist [31-33], the two-phase reaction of basic hydrogen peroxide (BHP) and chlorine gas is still the preferred technology for COIL systems, owing to its capability for generating large amounts of singlet-delta oxygen with short reaction times. BHP is prepared from equal parts 50 wt % H_2O_2 and 50 wt% KOH; the resulting solution is an effervescent, viscous fluid that decomposes rapidly at temperatures above 30°C. The overall reaction of BHP with chlorine to produce singlet-delta oxygen and heat is



The kinetics of the liquid-phase reactions are rapid, resulting in an overall reaction limited by mass transfer of chlorine across the gas-liquid interface, necessitating large interfacial areas within the reactor. Existing singlet-oxygen generator designs have achieved large gas-liquid contacting areas using wetted wall [34], gas-sparger [35] and liquid-spray reactors [36].

In addition to realizing large interfacial areas for chlorine mass transport, SOG designs must be capable of high rates of heat removal for safe and efficient operation. A primary safety challenge to COIL systems is preventing BHP overheating, which leads to rapid decomposition at temperatures above 30°C. During operation, reaction temperatures are maintained at 268 K to 258 K for safety and to minimize water vapor content in the gas product stream, which leads to deactivation of excited-state species [37]. These challenges are exacerbated by the high heat of reaction for singlet-delta oxygen generation. The increased surface area-to-volume ratios achievable in microchemical systems offer the superior heat and mass transport required by this reaction, as compared to macroscale counterparts [38].

In light of the highly toxic, corrosive and unstable reagents involved in this reaction network, the additional safety and redundancy of microchemical systems are a welcome alternative to conventional systems with reaction volumes equivalent to 1-10kW output. Perhaps most importantly, miniaturization of the entire COIL system is expected to result in significant reduction in overall system weight and volume necessary for next-generation transportable systems [20].

Silicon-based microchemical systems appear perfectly suited for high-capacity singlet-delta oxygen production, for use either by COIL systems or for organic synthesis processes [11]. Silicon construction and micrometer-scale heat transport lengths allow isothermal operation even at high reaction rates; gas and liquid distributors allow scale-out of individual reaction channels

while minimizing variations in distribution uniformity (common to conventional system scale-up) for greater design flexibility [39]; and capillary-based gas-liquid separators [40] allow disengagement of the gas product from the liquid phase immediately after reaction to minimize deactivation losses. A modeling study of the microscale singlet-oxygen generator predicted superior performance of the microreactor and the μ COIL system, as compared to state-of-the-art macroscale systems [20]. The present manuscript details the design of a prototype singlet-oxygen generator (including structured reaction channels, distributors, gas-liquid separator, cooling channels and packaging), with an emphasis upon verifying design models/expressions employed for each microsystem component. Overall system performance is also presented, with emphasis upon comparing observed, multiphase hydrodynamics within structured microscale packed-beds with conventional predictive maps. Complete details of microfabrication methods and IR-spectroscopic analysis of overall singlet-oxygen production by the resulting microdevice are provided by the authors elsewhere [13, 21].

DESIGN OF MICROSCALE JACKETED TRICKLE-BED SYSTEM

Conventional gas-liquid reactor systems are comprised of (i) a fluidic distributor for achieving uniform mixed inlet flow, (ii) a randomly or structured packed bed to provide maximum interfacial contact area, (iii) cooling or heating jacket for temperature control, and (iv) a disengagement volume for splitting reactor effluent into separate product phase(s). While each of these individual tasks has been demonstrated previously in silicon-based microsystems [38-41], this manuscript presented the first bottom-up design of an *integrated* microscale trickle-bed *system*, combining all of these tasks into a single, compact and efficient microdevice, illustrated conceptually in Figure 1 and by design in Figure 2.

The design methodology illustrated in Figure 2 centers around an isothermal model of the chemical reactor. In this manner, all subsequent component designs are based upon an optimal reactor design, independent of arbitrary device size constraints. Optimal bed properties obtained from the reactor model dictate post (structured packing) diameters and spacing, while individual reaction channel capacities dictate the number of identical channels necessary to meet overall target flow capacities. Spacing between reaction channels is selected based upon ease of microfabrication; nominally a spacing of 100 μm represents a reasonable balance between device compactness and fabrication reproducibility. The number of parallel reaction channels along with individual channel capacities dictate inlet bifurcation design, while the reaction channel pressure drop dictates the design of pressure-drop constrictions. Downstream of the reaction region, net gas and liquid effluent and target outlet (plenum) pressure guide the design of the gas-liquid disengagement region. Once dimensions and necessary design parameters for the packed-bed reaction channels, distribution region and disengagement region are determined, individual region blueprints, or lithography masks, can be developed which in turn dictate the footprints of each region. When combined, these three regions define the overall die size for an integrated microdevice where all three regions are placed on the frontside of the microdevice. Lastly, cooling channels are designed for placement on the backside of the microdevice, to ensure isothermal operation and adequate heat removal.

Trickle-Bed Reactor Model

A one-dimensional plug-flow reactor model (neglecting axial dispersion) was formulated to describe gas-liquid reaction and gas-phase deactivation in a single, microscale packed-bed. Owing to rapid liquid-phase kinetics, the overall rate of reaction can be assumed to be equal to

the rate of gas-liquid mass transport, and the mass transfer coefficient estimated from the limiting liquid-phase kinetics. The model assumed a liquid-fraction $\varepsilon_l = 0.08$ (with total void fraction of $\varepsilon = 0.40$). Gas-liquid interfacial area was estimated at $a = 5000 \text{ m}^{-1}$ based upon previously reported values in similar structured microscale packed beds by Losey et al. [38]. This model was originally developed as part of a larger design study of a microscale Chemical-Oxygen Iodine Laser (μCOIL) system, and complete details of the model formulation are provided elsewhere [20]. Results of this modeling analysis are summarized in Table I.

Reactor Bed Design

The bed geometry was selected to match the modeling results summarized in Table I. In order to achieve overall device capacities in excess of 1 mL/min (for effective fluid handling and product analysis), each integrated device is designed to contain 32 parallel packed-bed channels. Individual packed bed dimensions were 650 μm in width by 300 μm in depth, with structured posts serving as the packing media. Structured two-dimensional packing elements were chosen over randomly dumped beds for greater ease of manufacture and operation. Each bed was packed with $\sim 5 \times 10^3$ identical, 70 μm diameter posts placed in a regular hexagonal pattern with identical pore throats of 20 μm , corresponding to an overall bed porosity of 0.40 (Figure 1b). Post diameters correspond to a bed width-to-packing diameter ratio of $\sim 8:1$, generally considered the minimum for uniform flow distribution in conventional packed-bed systems [42]. Larger bed-to-packing diameter ratios were not implemented to maximize device yield and decrease fabrication complexity.

Design of Gas and Liquid Distribution

A critical challenge to the scale-up of microchemical systems is appropriate design of fluidic distributors [38,39,43] to ensure consistent reagent supply to each microchannel. While

simple bifurcated gas and liquid inlets split individual external feeds amongst multiple reaction channels (Figure 1a), minor fluctuations in pressure drop associated with each flow path may still result in significant distribution non-uniformity [38]. To ensure uniform gas and liquid distribution to each reaction channel, individual reaction channels are connected to the inlet bifurcation arrays via two shallow-pressure drop channels for gas reagent and a single shallow pressure drop channel for liquid reagent, following Wada and coworkers [39] (Figure 1a).

Pressure-drop channels were designed to achieve a 3-fold greater pressure drop than downstream reaction channel pressure drops. Further pressurization of the BHP supply was not considered feasible in light of safety considerations. Pressure-drop was determined from the Hagen-Poiseuille equation for an incompressible fluid,

$$\Delta P_{pdc} = \frac{128\mu_l \cdot L_{pdc} Q_{pdc}}{\pi \cdot d_{pdc}^4} \quad (1a)$$

where μ_l is the fluid viscosity, L_{pdc} is the length the pressure-drop channel, Q_{pdc} is the capacity of a single pressure-drop channel, and d_{pdc} is the hydraulic diameter of a single pressure-drop channel. Pressure-drop channel widths of 25 μm and depths of 20 μm were selected as minimum feature sizes without affecting overall device yield or introducing plugging challenges during operation. Optimum operating conditions predicted from the design optimization study corresponded to a pressure drop of 360 torr across the reaction channel (Table I). For a target pressure drop of 1200 torr across the pressure-drop channel at optimal operating conditions, a length of 2.5 mm is obtained from Equation 1a.

Design of Capillary Gas-Liquid Separator

Macroscale gas-liquid reactors employ downstream phase separation by exploiting differences in density, primarily via gravity separation. In microscale systems, capillary forces

compete with or dominate gravity forces, limiting the use of conventional density-separation methods for gas-liquid disengagement. For this reason, a gas-liquid separator based upon capillary action, originally developed by Günther *et al.* [40], was employed to separate the effluent stream exiting the array of 32 packed-beds.

The separator consists of a collection conduit, the floor of which is patterned with an array of parallel capillary pores for selective removal of the liquid phase from the gas-liquid effluent (Figure 1d). Individual pores must be small enough to maintain sufficient capillary pressure to resist gas invasion, while remaining large enough to provide useful liquid removal rates (Figure 3). Separation is accomplished by applying a pressure drop across the capillary channels smaller than the maximum pressure that the meniscus can withstand before breakup, so the gas phase does not get through the capillary. The upper bound of this pressure calculated from the Laplace-Young Equation:

$$\Delta P_{cap} = \frac{4\sigma}{d_{cap}} \cos \theta \quad (2)$$

where σ is the liquid surface tension, θ is the wetting angle and d_{cap} is the diameter of a single capillary pore. The capacity of a single pore in the separator is then calculated from the Hagen-Poiseuille equation,

$$Q_{cap} = \frac{\pi \cdot d_{cap}^4 \cdot \Delta P_{sep}}{128 \mu_l \cdot L_{cap}} \quad (1b)$$

where ΔP_{sep} is the actual pressure drop applied across the capillary separator and L_{cap} is the pore length. A capillary pore length of 300 μm was selected to accommodate both the reactor bed and the separator on the same 625 μm thick silicon substrate. Capillary diameters were chosen to be 25 μm , corresponding to a maximum allowable pressure differential of 117 torr, assuming that

BHP's surface tension is equivalent to that of water (73 dynes/cm) and assuming negligible wetting angle (corresponding to water on silicon nitride). Actual surface tension and wetting angle data for BHP and silicon were unknown. In light of this potential source of error, the operating pressure drop across the separator was targeted for 25% of the predicted capillary pressure (30 torr), to ensure desired performance during operation. This corresponds to a single-pore liquid removal rate of $1.7 \times 10^{-5} \text{ cm}^3/\text{sec}$ (Equation 1b). Operation at the maximum planned liquid flowrate of $0.123 \text{ cm}^3/\text{sec}$ (determined from modeling analysis) requires ~ 7200 capillary pores. Operation at the optimum liquid flowrate of $0.0492 \text{ cm}^3/\text{sec}$ requires only ~ 2800 pores. However, pre-wetting of the separator device allows pores to remain liquid-filled while not in use, thereby preventing gas penetration into the liquid effluent (Figure 3). Pre-wetting of the separator is a crucial step to run the microscale reactor system. Analysis of the working conditions used to gather the IR data showed that only a small fraction of open pores ($<5\%$) are needed to suck the singlet oxygen to the liquid by-products outlet instead of the proper singlet exit port [21].

Design of Cooling Channels

Once the reaction channels, gas-liquid inlets and gas-liquid disengagement regions were designed, the overall die size of the microreactor was set to $3.6\text{cm} \times 2.8\text{cm}$ to accommodate these features and feed/outlet ports on device backside. The final design step was to specify the cooling channel geometry to maintain the desired chip temperatures of $273 \text{ K} - 283 \text{ K}$ in the presence of heat addition from both the ambient environment and singlet-oxygen production. At maximum design flowrates of $8 \times 10^{-5} \text{ mol Cl}_2/\text{s}$, the corresponding heat production via reaction is 8.8 W , while optimal operating conditions correspond to a heat release rate of 3.5 W . For a chip

design temperature of 268 K, heat losses from the microdevice via natural convection are estimated at ~ 0.50 W.

The Nusselt number corresponding to coolant flow through a single microchannel was estimated via the correlation of Sieder and Tate [44] for laminar flow (Reynolds number $N_{Re} < 2100$) through a cylindrical pipe, assuming constant coolant viscosity:

$$N_{Nu} = \frac{h_a D}{k} = 1.86 \left(N_{Re} \cdot N_{Pr} \cdot \frac{D}{L} \right)^{1/3} = 1.86 \left(\frac{4 \rho C_p Q}{k L_c \pi} \right)^{1/3} \quad (3)$$

Equating the maximum heat flow out of the chip with heat flow into the coolant (assuming steady-state operation) yields an expression which is solved for the coolant outlet temperature and the heat duty of the cooling channel:

$$q^- = h_a \pi D_c L_c \left(T_{wall} - \left(\frac{T_{c,in} + T_{c,out}}{2} \right) \right) \quad (4a)$$

$$q^+ = Q_c \rho_c C_p (T_{c,in} - T_{c,out}) \quad (4b)$$

$$\frac{2T_{wall} - T_{c,in}(1 - \alpha)}{(1 + \alpha)} = T_{c,out}, \text{ where } \alpha = \left(\frac{\rho_c Q_c C_p}{\pi L_c N_{Nu} k} \right) = \left(\frac{\rho_c^{2/3} Q_c^{2/3} C_p^{2/3}}{6.33 \cdot L_c^{2/3} k^{2/3}} \right) \quad (4)$$

The corresponding pressure drop for a given coolant capacity is given by the Hagen-Poiseuille equation,

$$\Delta P_c = \frac{128 \cdot L_c \mu_c Q_c}{\pi l_c^4} \quad (1c)$$

For a single cooling channel at fixed coolant flowrate, inspection of Equations 3, 4 and 1c illustrate that heat removal is not a direct function of hydraulic diameter, and that $q \propto (L_c)^{2/3}$ while $\Delta P \propto L_c$. Thus, as flow length is increased, the amount of energy required for pumping outpaces the rate of heat removal. The energy required to flow the coolant goes mainly to pay for

the viscous losses, which produce heating of the coolant, directly interfering with its heat removal capacity. Therefore, the design of an efficient heat exchanger should make provisions for its heat removal capacity to be substantially larger than the heating implied in flowing the coolant. The hydraulic diameter indirectly influences net heat removal by dictating the number of cooling channels that can be incorporated into the microdevice. For a fixed volume available for channel placement, geometry shows that $q \propto n_{channels} \propto (d_c)^{-2}$ while from equation 1c we see that $\Delta P \propto (d_c)^{-4}$. Thus, selection of hydraulic diameter represents an indirect balance between heat removal rates and pressure drop.

The established die size (3.6cm x 2.8cm) provides a 2.2cm x 8.5mm footprint for incorporation of cooling channels of 300 μ m depth (Figure 1d). Cross-flow operation of cooling channels (alignment of channels perpendicular to reaction channels) was selected to ensure maximum uniformity of reactor temperature along a given reaction channel, and to accommodate coolant port placement compatible with reactant and effluent port placements. Channel dimensions of 300 x 300 μ m ($D_c = 339 \mu$ m) x 22 mm allow placement of 19 separate cooling channel on-chip, with single-pass operation of coolant channels ($L_c = 22$ mm) to maintain low pressure drops.

Design calculations were performed for a target coolant inlet temperature of 258 K and chip temperature of 268 K. Design calculations assumed the use of Syltherm[®] XLT Fluid as a coolant. The physical properties of Syltherm[®] XLT Fluid are summarized in Table II. For a net coolant capacity of 137 cm³/min, $N_{Re} = 157.9$, and $N_{Nu} = 8.04$, the target heat removal rate of 4 W is achieved at a pressure drop of 21 kPa. For a net coolant capacity of 237 cm³/min, a heat removal rate of 10 W can be achieved at a pressure drop of 69 kPa, corresponding to the

maximum pressure drop achievable by the chiller/recirculator employed in the experimental procedure.

EXPERIMENTAL

Chip Fabrication

The integrated microscale trickle-bed system was fabricated from two individually micromachined silicon layers of thickness 625 μm each, capped with a 2mm Pyrex layer to enable optical access to packed-bed and capillary separator. A cross-sectional schematic of the microdevice is presented in Figure 4a, alongside optical images of the backside of the chip, the frontside of the chip, and the internal cooling channel features (Figure 4b-d). The fabrication process relies heavily on deep reactive ion etching (DRIE), fusion bonding and anodic bonding methods to construct the device in silicon. Subsequent deposition of a conformal layer of LPCVD-deposited silicon-rich nitride provided suitable protection from reactant and by-product corrosion. Complete details of the fabrication process are presented elsewhere [13].

Testing Apparatus

The testing apparatus is shown schematically in Figure 5. Gas delivery was provided via mass flow controllers, connected with a mixing tee and downstream pressure transducer for measuring delivery pressure. The gas outlet flow path included (i) an optical cuvette for measurement of singlet-oxygen emission via spectroscopy, (ii) a cryo-trap for chlorine and moisture removal, (iii) a sampling port for mass spectroscopy, (iv) a back-pressure valve for control of gas outlet pressure, and lastly (v) a corrosion resistant vacuum pump. The liquid supply reservoir was a glass-lined, jacketed, stainless steel pressurized reservoir (PARR), pumped to the chip/chuck assembly by constant-pressure helium gas displacement using separate

mass-flow and back-pressure controllers. The liquid outlet flow was collected in a jacketed three-neck glass flask, maintained at constant vacuum pressure via a back-pressure controller connected to the vacuum pump. In both the gas and liquid outlet vacuum lines, glass cryo-traps were employed to remove any moisture or chlorine vapor upstream of the vacuum components. Both the liquid inlet and outlet reservoirs were maintained at sub-ambient temperatures using a chiller/recirculator, which also supplied coolant flow to the chip. Coolant supply rates to the liquid reservoirs and chip were controlled using flowmeters. Thermocouples provided constant monitoring of chip and reservoir temperatures during experimentation. Fluidic connections to the glassware and the packaging chuck were made using PTFE tubing. Ultra-high purity gases (>99.999%) were used in the experiments. The entire experimental apparatus, with the exception of the coolant recirculator/chiller, was contained within a ventilated enclosure to minimize the hazard of chlorine exposure. Complete details of the testing apparatus are presented elsewhere [21].

Spectroscopic Measurement of Singlet-Delta Oxygen Yield and Chlorine Conversion

In all experiments, singlet-delta oxygen yield was measured via photon emission spectroscopy. Quantitative measurement of singlet-delta oxygen is obtained from monitoring the decay of solitary $O_2(^1\Delta)$ molecules into the triplet state, which produces photons at 1268 nm. Spectroscopic measurement of singlet-delta oxygen concentration was performed in collaboration with Physical Sciences Inc (Andover, MA). The test cell was a rectangular quartz cuvette connected to the gas outlet by a 0.4 cm diameter quartz tube. Collimated optics sampled a cylindrical cross section of the cuvette yielding a 1.1 cm field of view. A liquid-nitrogen cooled InGaAs array spectrometer was used to analyze photons from the spontaneous emission. The intensity of the spectrometer signal was calibrated to the spectral radiance of a blackbody source

at 1000 K. Complete discussion of this analysis technique is presented by Rawlins and coworkers [45]. Complete details of the implemented spectrometric oxygen diagnostics are presented elsewhere [21].

Packaging of Completed Microdevice

A consistent challenge to microchemical systems is providing fluidic and/or electronic connections to the microdevice via packaging. Packaging strategies include sealing fluidic connections to the microdevice surface with chemical-resistant epoxies [46] or metal-solder bonds [47], or by compression-sealing with a fluidic chuck containing chemically resistant o-rings or gaskets [39]. Both chlorine gas and BHP solution are incompatible with soldering materials, while epoxies proved unstable over long operating times. For these reasons, a packaging system consisting of a fluidic chuck and clamping plate was employed (Figure 5b,c).

Both the chuck and the clamping plate were machined from Tefzel®, and Kalrez o-rings and gaskets were used to connect the chip to Teflon tubing to meet the structural and chemical performance requirements. The clamping plate of the package has an opening for optical access to the reactor bed and separator during operation. In order to minimize deactivation of product singlet-oxygen via wall collisions, glass materials were employed for the gas outlet [37]. Complete details of the device package are presented elsewhere [13].

Experimental Procedure

For each experiment, a 1/32" O.D. thermocouple (Omega) was installed in the on-chip port for monitoring chip temperature, the microdevice was sealed within the chuck assembly, and all fluidic connections were attached. The chuck-chip assembly was then secured in place,

and the spectroscopy optics were aligned to the optical cuvette. The chiller/recirculator was then switched on, and coolant flow to both liquid reservoirs and the on-chip cooling channels were set to desired rates. Sufficient time was allowed for the chiller temperature to reach an operating temperature of 243 K. Owing to heat addition through insulated coolant lines and flowmeters, this corresponded to a coolant temperature of 258 K at the chip inlet. Basic hydrogen peroxide (BHP) solution was prepared as follows. First, 100 cm³ of 50 wt% aqueous solution of KOH was prepared from distilled water and 66 g KOH pellets (Fisher) in a volumetric flask. Meanwhile, 50 cm³ of 50 wt% hydrogen peroxide aqueous solution (Aldrich) was poured into the liquid feed reservoir and cooled to 258.15 K. KOH solution was added in 5 cm³ quantities, allowing sufficient time for solution temperature to return to 258 K between each addition, to a total of 50 cm³. The BHP feed reservoir was then sealed and pressurized with helium gas to the desired delivery pressure, thus initiating liquid flow to the cooled microchip. Gas flow was initiated by opening helium flow to a rate of 50 standard cm³/min. Liquid flow was maintained by delivering helium gas to the BHP reservoir at a constant displacement pressure of 200 – 400 kPa. Once both liquid and gas supply to the chip were verified, the vacuum pump was turned on and the vent valves were closed, allowing the system to pump down to operating pressures. Gas outlet pressures were typically between 10 and 20 kPa, with liquid outlet pressures nominally set to 5 kPa less than gas outlet pressure. During pump-down, care was taken to ensure that the gas outlet pressure remained greater than the liquid outlet pressure, to avoid suction of liquid reagent into the gas outlet and downstream optics. Once both gas and liquid outlets reached steady operating pressures, reaction was initiated by blending chlorine gas into the gas feed at a mole fraction of 25%. Prior to chlorine introduction, the ventilated enclosure was closed and sealed to protect

against chlorine exposure. Progress of the reaction was visually confirmed via red glow corresponding to $O_2(^1\Delta)$ dimol emission (Figures 1e and 1f) [13].

RESULTS

Pressure-Drop Measurements

Initial experiments employing helium and distilled water at ambient temperature and outlet pressure were performed to measure single and two-phase pressure drops across the miniaturized distributor and packed-bed to verify design equations. Single-phase pressure drops were obtained assuming a chip outlet pressure of 101.3 kPa while monitoring delivery pressures. A parity plot of predicted pressure drops calculated from the Ergun equation for single-phase flow [48] and employing the correlation of Larkins et al. [49] for two-phase flow verifies the accuracy of macroscale packed-bed pressure drop equations for describing the miniaturized packed-bed (Figure 6a).

Characterization of Cooling Channels

Preliminary experiments were also performed to estimate heat losses to ambient from the chip in the absence of chemical reaction and to estimate heat transfer coefficients within the microdevice. While experiments in the absence of chemical reaction limit the resolution of heat transfer measurements, they alleviate the greater uncertainty associated with estimating reaction heats. Two separate experiments were performed to capture (i) steady-state and (ii) transient cooling of the microdevice in the absence of reactant flow. In all experiments, thermocouples were placed approximately 4 mm upstream and downstream of the packaging to monitor coolant flow entering and exiting the chip, while a third thermocouple monitored chip temperature via

the chip's sensor port. Coolant flowmeters and thermocouples were calibrated to determine associated measurement uncertainties, $T_i = T_i \pm \Delta e_c$ and $Q_c = Q_c \pm \Delta e_v$.

In the first experiment, a constant coolant flowrate of 73.4 cm³/min at 277 K was supplied to the initially ambient-temperature chip, and temperatures were monitored at regular time intervals until the steady-state chip temperature of 278 K was reached. Temperature measurements combined with coolant flowrates allowed calculation of the net rate of heat addition to the coolant fluid from the relation:

$$q = Q_c \rho_c C_{p,c} (\Delta T_{coolant}) \text{ where } \Delta T_{coolant} = T_{c,in} - T_{c,out} \pm \sqrt{2} \cdot \Delta e_T \quad (5),$$

From error propagation theory, we may calculate the resulting uncertainty as

$$\Delta e_Q = \rho_c C_{p,c} \cdot \sqrt{(T_{c,in} - T_{c,out})^2 \cdot \Delta e_v^2 + Q_c^2 \cdot 2 \cdot \Delta e_T^2} \quad (5a)$$

Owing to the relatively small thermal mass of the silicon microdevice (7.6 g) and the insulating nature of the Tefzel© packaging assembly, calculated heat removal rates were the same order-of-magnitude as measurement uncertainty. Despite measurement uncertainty, the experimental data did follow the expected trendline (Figure 6b).

Multiple measurements of steady-state chip temperatures and cooling inlet/outlet temperatures were made as well. For each steady-state measurement, heat removal rate, q , was calculated from Equation (5) with its associated uncertainty estimated from Equation (5a). Assuming uniform chip temperature and a heat-transfer surface area of 2.35x10⁻⁵ m², the heat transfer coefficient can be estimated from the following relation,

$$h_a = \frac{q}{A_c (\Delta T_{chip})}, \text{ where } \Delta T_{chip} = T_{chip} - \left(\frac{T_{c,in} + T_{c,out}}{2} \right) \pm \sqrt{3} \cdot \Delta e_T \quad (6),$$

with the resulting error,

$$\Delta e_{h_a} = \frac{1}{A_c} \sqrt{\left(\frac{\Delta e_Q^2}{\Delta T_{chip}^2} \right) + \left(\frac{3 \cdot \Delta e_T^2 \cdot q^2}{\Delta T_{chip}^4} \right)} \quad (6a)$$

Again, propagation of error results in uncertainties of the same order-of-magnitude as calculated heat-transfer coefficients, as a dual result of low overall heat addition and low temperature gradients (Figure 6c).

Flow Regime Observations

During the preliminary two-phase experiments described above, two flow regimes were observed over the range of helium and water flow rates investigated. At low gas flows, the gas-liquid interface appeared static, with liquid preferentially flowing along and near the walls of the channel (Figure 7). Liquid appeared to flow through a network of wetted pore throats, in similar fashion to the macroscale “trickling-flow” regime, with few visible fluctuations. This regime was identical to the “annular flow” reported by Losey *et al.* [50] and Wada *et al.* [39] in similar post-bed microreactors. At elevated gas flows, the gas-liquid interface fluctuates rapidly, as pore throats oscillate between wetted and dry operation. This regime was similar to the “churn flow” regime reported by Wada *et al.* [39] and the “dispersed flow” reported by Losey [50]. In this flow regime, fluctuations in the gas-liquid interface spanned individual pore throats, but not the entire column diameter. It is important to note that under all singlet-oxygen generating conditions reported, only the “annular-flow” regime occurred.

One other flow regime has been reported in previous studies of microscale post-bed reactors, specifically the “slug flow” regime, characterized by channel-spanning gas plugs and observed by both Wada *et al.* [39] and Losey [50]. The presently obtained flow regime data is summarized with that of Wada *et al.* [39] and Losey [50], employing conventional flow regime maps (Figure 7). Three flow regime maps were employed; (i) the Baker coordinate map [51]

commonly employed for open pipe flow, (ii) the Charpentier-Favier coordinate map [52] which is popular for trickle-bed (packed pipe) flow, and (iii) the Talmor coordinate map [53], also employed for trickle-bed systems.

Singlet-Oxygen Production

The resulting miniaturized trickle-bed reactor system was investigated for singlet-delta oxygen production over a range of operating conditions, including outlet pressure, inlet flowrate and chlorine mole fraction. Singlet-delta oxygen yield was calculated from spectrometer data and chip effluent values extrapolated from singlet-delta oxygen deactivation models accounting for losses en route to the optical sensing region. Optimal performance corresponded to a singlet-delta oxygen yield of 78% at the chip's outlet, occurring at a total gas flowrate of 75 sccm and an outlet pressure of 13 kPa. This compares favorably with maximum yields of 73% reported to date for state-of-the-art macroscale singlet-oxygen generators. Complete details of the data analysis and determination of singlet-oxygen yields over a broad range of gas flows, compositions and pressures, are presented in a separate report [21].

DISCUSSION

Preliminary measurements for pressure drop and heat transfer demonstrate the applicability of established equations for laminar flow in the design of microscale systems. The empirical relationship of Ergun [48] agrees well with single-phase pressure drop data, and the relationship of Larkins et al. [49] agrees well with the two-phase pressure drop measurements. During operation some non-uniformity of flow patterns between individual channels was observed, indicating variations in inlet pressure and gas/liquid feedrates from channel to channel. As discussed in the design section of the manuscript, flow uniformity improves with increasing

pressure drop across the pressure-drop channels (within the distribution zone), assuming that all pressure drop channels are identical. This last caveat introduces a significant fabrication challenge, as pressure-drop channel features are sufficiently small (25 μm width x 20 μm depth) as to present reproducibility issues. Thus, flow uniformity can be improved by both (1) increasing pressure drop across the pressure-drop channels via increased channel lengths, and (2) increasing pressure-drop channel dimensions to improve consistency and reproducibility during microfabrication.

Hydrodynamic observations and attempts to “map” flow regimes according to macroscale conventions illustrate significant differences for microscale systems. Figure 7 summarizes the presently obtained flow regime data alongside that of Wada et al. [39] and Losey [50] obtained in similar packed-bed systems, using coordinate maps following (a) the Baker coordinate map [51] commonly employed for open pipe flow, (b) the Charpentier-Favier coordinate map [52] which is popular for trickle-bed (packed pipe) flow, and (c) the Talmor coordinate map [53]. By comparing flow regime data obtained in the present work with those previously reported, we can comprehensively evaluate conventional flow regime map prediction of annular and dispersed flow regimes (observed in the present work) as well as slug flow, previously observed by both Losey [50] and Wada et al., [39]. In all three cases, experimental data does not follow trends established in the literature for macroscale trickle-beds. Suggested boundaries separating individual flow regimes are superimposed over the experimental data in Figure 7. Both the Baker and Charpentier coordinate maps are found capable of grouping like flow regimes with relatively smooth boundaries, while the Talmor map requires much more complex boundaries. In all three cases, data corresponding to the annular flow regime proved difficult to separate from the dispersed regime. The Charpentier-Favier coordinate map indicates that the boundary separating

annular flow and slug-flow in microscale packed-beds occurs at a near-constant liquid-to-gas flow ratio; i.e., increasing gas flowrate does not reduce the stability of the annular flow regime. This is in contrast to conventional packed-bed data, where increased gas flowrate results in lower liquid-to-gas flow ratio necessary for trickling-to-pulsing transition. The Charpentier-Favier and Baker coordinate maps both indicate that the dispersed flow regime occurs at the limit of large gas and liquid flow rates, analogous to conditions for dispersed-bubble flow in macroscale trickle-beds.

Further refinements in packed-bed models are expected to improve design of subsequent microscale trickle-bed reactors. Analysis of the estimated reactant molecular diffusivities indicate that the Bodenstein numbers span $O(10^0 - 10^2)$ over the range of conditions investigated (Table II). Thus, the inclusion of axial dispersion is expected to further refine model accuracy. Additional improvement in model accuracy is expected by including rate expressions for liquid-phase deactivation of singlet-oxygen product. The presently employed model accounts for gas-phase deactivation kinetics only, via the simplifying assumption of negligible liquid-phase deactivation owing to thin reaction depths within the liquid phase ($\sim 1 \times 10^{-6}$ cm).

More critical is the need for re-evaluation of gas-liquid contacting areas within the microdevice. Model values were based upon previously reported gas-liquid contacting areas obtained for the cyclohexane-hydrogen system in a similar microscale packed-bed under dispersed flow regime [50]. Visual confirmation of an annular flow regime during singlet-delta oxygen generation suggests that actual gas-liquid contacting areas encountered in the present work may be significantly smaller than expected. Analysis of flow regime maps in Figure 7 suggest that by increasing liquid flowrate (for a given constant gas flowrate), onset of the dispersed flow regime will occur resulting in improved gas-liquid mixing.

Assuming purely annular flow (instead of dispersed-flow) in the presence of the packing structure, and assuming model values for $\varepsilon_l = 0.08$, then $w_{film} \sim 65 \mu\text{m}$ and the minimum and maximum liquid-gas contacting areas can be estimated from geometry (Figure 8) as:

$$a_{l-g}^{\min} = \frac{2 \cdot \left(\frac{t_p}{z_p} \right) \cdot L_{pbr} \cdot h_{pbr}}{2 \cdot (\varepsilon_{pbr}) \cdot (w_{pbr} - w_{film}) \cdot L_{pbr} \cdot h_{pbr}} = \frac{\left(\frac{20}{78} \right)}{(0.4) \cdot (650 - 65)} = 1100 \text{ m}^{-1}$$

$$a_{l-g}^{\min} = \frac{2 \cdot \left(\frac{t_p}{z_p} \right) \cdot L_{pbr} \cdot h_{pbr}}{2 \cdot (\varepsilon_{pbr}) \cdot (w_{pbr} - w_{film}) \cdot L_{pbr} \cdot h_{pbr}} = \frac{\left(\frac{86}{156} \right)}{(0.4) \cdot (650 - 65)} = 2400 \text{ m}^{-1}$$

These numbers suggest interfacial transfer areas significantly lower than the value of 5000 m^{-1} employed in the reactor design model. This illustrates the need for continued efforts to accurately predict flow regimes within the microscale packed bed during the design phase, as well as the need to develop accurate experimental methods for measuring gas-liquid mass transfer. The present microdevice represents a first step towards achieving both of these goals. Further reduction in the size of the gas-liquid disengagement volume for the present microdevice would improve the accuracy of such mass-transfer measurements.

While not exploited in the present work, the use of packing elements formed via reactive extrusion (e.g. Deep-Reactive Ion Etching or DRIE) from two-dimensional lithography mask features also allows complete control over placement and shape of each element without imposing limits on total element quantity. This packed-bed design strategy represents a logical extension of, and improvement over, previous fundamental studies in structured two-dimensional beds constructed from conventional machining [54].

CONCLUSIONS

This manuscript reports the complete bottom-to-top modeling, design, construction and flow testing of a fully miniaturized trickle-bed reactor system. This system successfully integrates gas-liquid distributors, structured packed beds, gas-liquid separator and cooling channels into one compact microscale device. The resulting device was demonstrated for the exothermic reaction of chlorine gas and basic hydrogen peroxide to produce singlet-delta oxygen. This chemistry represented an aggressive test of microchemical systems capabilities, owing to the highly corrosive and reactive reagents, high heat of reaction, significant gas-liquid mass transport limitations, and subsequent deactivation challenges of gaseous product. Preliminary experiments verified the accurate design of gas and liquid distributors, gas-liquid separator and cooling channels. The applicability of well-established pressure-drop correlations, specifically those of Ergun [48] and Larkins *et al.* [49] was verified with water and helium fluids. Observations of the gas-liquid flow regimes within the structured microscale packed-bed system were compared with conventional, i.e. macroscale, regime maps. This comparison identified a significant disconnect between macroscale and microscale flow regime boundaries in gas-liquid packed-beds, which provides a basis for further hydrodynamic and interfacial mass transport studies.

Experimental data verified that the microdevice was capable of producing singlet-delta oxygen in measurable quantities, in general agreement with packed-bed reactor models employed for the presented design methodology [20]. Analysis of molecular diffusivities suggests further improvement in model accuracy may be achieved with inclusion of second-order dispersion terms. The resulting microscale trickle-bed system is also expected to serve as a flexible tool for relating bed and packing geometry to gas-liquid hydrodynamics and mass

transport, and demonstrates a significant step towards realizing fully integrated, miniaturized gas-liquid and gas-liquid-solid microreactor systems.

ACKNOWLEDGMENTS

Microfabrication of all devices was performed in the Microsystems Technology Laboratories (MTL) at M.I.T. The authors wish to acknowledge Dr. Hanqing Li's contributions to the device fabrication and Dr. Terry Rawlins's, Dr. Seonkyung Lee's, and Dr. Steve Davis's contributions to the spectroscopic measurements. This work was funded by the Tactical Technology Office at DARPA, the Missile Defense Agency (MDA), and the Air Force Research Laboratory (AFRL) (DARPA Order No. T171/00, Program Code: 4G10; Issued by DARPA/CMO under Contract No. MDA972-04-C-0140). The views and conclusions contained in this document are those of the authors and should not be interpreted as representing the official policies, either expressed or implied, of the Defense Advanced Research Projects Agency or the U.S. Government.

NOMENCLATURE

a = inter-phase transfer area, m^2

C_p = specific heat, $J/gm.K$

d = diameter, cm

D = packed-bed dispersion coefficient, cm^2/s

D_{A-B} = molecular diffusivity of solute A in solvent B, cm^2/s

Δe_i = uncertainty in calculated value i

h_a = convection heat transfer coefficient,

k = thermal conductivity,

L = length, cm

P = absolute pressure, kPa

Q = volumetric flowrate, cm^3/s

q^+ = rate of heat addition due to chemical reaction, J/s

q^- = rate of heat removal due to coolant flow, J/s

T = Temperature, K

t_p = pore throat, m

v_i = fluid velocity of phase i , cm/s

w_i = width of fluid i film

z_p = pore spacing, along axial length of bed

Symbols

ε = void fraction, dimensionless

μ = viscosity, $kg/m.s$

θ = wetting angle, radians

ρ = density, kg/m³

σ = surface tension, N/m

Dimensionless Numbers

$$N_{Bo} = \frac{\nu L}{D} = \text{Bodenstein number}$$

$$N_{Gr} = \frac{L^3 \rho_{air}^2 g \beta \Delta T}{\mu_{air}^2} = \text{Grashoff Number}$$

$$N_{Nu} = \frac{h_a D}{k} = \text{Nusselt Number}$$

$$N_{Pr} = \frac{C_p \mu}{k} = \text{Prandtl Number}$$

$$N_{Re} = \frac{\rho v D}{\mu} = \text{Reynold's Number}$$

$$N_{We} = \frac{\rho v^2 D}{\sigma} = \text{Weber Number}$$

$$\gamma = \left[\left(\frac{\rho_g}{\rho_{air}} \right) \left(\frac{\rho_l}{\rho_{water}} \right) \right]^{1/2}, \text{ Lockhart-Martinelli parameter for correcting gas, liquid space}$$

velocities (In Figure 7).

$$\lambda = \left(\frac{\sigma_{water}}{\sigma_l} \right) \left[\left(\frac{\mu_l}{\mu_{water}} \right) \left(\frac{\rho_{water}}{\rho_l} \right)^2 \right]^{1/3}, \text{ flow parameter for Baker Plot (Figure 7c).}$$

Subscripts

c = cooling channels

cap = capillary pore in gas-liquid separator

g = gas phase

l = liquid phase

l-g = liquid-gas interface

p = packing element

pbr = packed-bed region

pdc = pressure drop channels

REFERENCES

1. Dittrich, P.S., Tachikawa, K, Manz, A., Micro Total Analysis Systems. Latest Advancements and Trends. *Analytical Chemistry*. 2006;78(12):3887 – 3907.
2. Vilkner, T, Janasek, D, Manz, A, Micro Total Analysis Systems. Recent Developments. *Analytical Chemistry*. 2004;76(12):3373-3385.
3. El-Ali, J., Sorger, P.K., Jensen, K.F., Cells on Chips. *Nature*. 2006;442:403-411.
4. Holladay, J.D., Y. Wang and E. Jones. Review of Developments in Portable Hydrogen Production Using Microreactor Technology. *Chem. Rev.* 2004;104:4767-4790.
5. Jensen, K.F., Microreaction Engineering – Is Small Better? *Chem. Eng. Sci.* 2001; 56:293-303.
6. deMello, A.J., Control and Detection of Chemical Reactions in Microfluidic Systems. *Nature* 2006;422:394-402.
7. Pennemann, H., Watts, P., Haswell, S.J., Hessel, V., Loewe, H., Benchmarking of Microreactor Applications. *Organic Process Research and Development* 2004;8(3):422-439.
8. Jahnisch, K., Hessel, V., Lowe, H., Baems, M., Chemistry in Microstructured Reactors. *Angewandte Chemie-International Edition*, 2004;43(4):406-446.
9. Hessel, V., Hardt, S., Lowe, H., Chemical Micro Process Engineering: Fundamentals, Modeling and Reactions. John Wiley and Sons: 2004.
10. Stankiewicz, A.I., J.A. Moulijn, Process Intensification: Transforming Chemical Engineering. *Chem. Eng. Prog.* 2000;1:22-34
11. Jensen, K.F., Silicon-Based Microchemical Systems: Characteristics and Applications. *MRS Bulletin*. 2006;31(2):101-107.

12. Ajmera, S.K., M.W. Losey, K.F. Jensen and M.A. Schmidt. Microfabricated Packed-Bed Reactor for Phosgene Synthesis. *AIChE J.* 2001; 47:1639-1647.
13. Velasquez-Garcia, L.F., T.F. Hill, B.A. Wilhite, W.T. Rawlins, S. Lee, K.F. Jensen, A.H. Epstein and C. Livermore. A MEMS Singlet-Oxygen Generator – Part I: Design and Fabrication. *Accepted for publication in Journal of Microelectromechanical Systems.*
14. Ledermann, N., J. Baborowski, P. Muralt, N. Xantopoulos, J.-M. Tellenbach. Sputtered Silicon Carbide Thin Films as Protective Coatings for MEMS Applications. *Surface and Coatings Technology.* 2000;125:246-250.
15. DeMas, N., A. Gunther, M.A. Schmidt and K.F. Jensen. Microfabricated Multiphase Reactors for the Selective Direct Fluorination of Aromatics. *Ind. Eng. Chem. Res.* 2003; 42: 698-710.
16. Thorsen, T., Maerkl, S.J. and S.R. Quake. Microfluidic Large-Scale Integration. *Science.* 2002; 298: 580-584.
17. DeMas, N., A. Gunther, T. Kraus, M.A. Schmidt and K.F. Jensen. Scaled Out Multilayer Gas-Liquid Microreactor with Integrated Velocimetry Sensors. *I&EC Res.* 2005;44:8997-9013.
18. Arana, L.R., S.B. Schaevitz, A.J. Franz, M.A. Schmidt and K.F. Jensen. A Microfabricated Suspended-Tube Chemical Reactor for Thermally Efficient Fuel Processing. *J. Microelectromech. Syst.* 2003;12:600-612.
19. Sahoo, H.R., J.G. Kralj and K.F. Jensen. Multi-Step Continuous Flow Microchemical Synthesis Involving Multiple Reactions and Separations. *Angew. Chemie. Int. Ed.* 2007; 46: 5704-5708.

20. Wilhite, B.A., C. Livermore, Y. Gong, A.H. Epstein and K.F. Jensen. Design of a MEMS-based Microchemical Oxygen-Iodine Laser (μ COIL) System. IEEE J. Quant. Elec. 2004;40:1041.
21. Hill, T.F., L.F. Velasquez-Garcia, B.A. Wilhite, W.T. Rawlins, S. Lee, K.F. Jensen, A.H. Epstein and C. Livermore. A MEMS Singlet-Oxygen Generator – Part II: Testing. *submitted for publication in Journal of Microelectromechanical Systems*.
22. Wasserman, H.H. and R. W. Murray. Singlet Oxygen. New York, Academic Press Inc., 1979.
23. Clennan, E.L. New Mechanistic and Synthetic Aspects of Singlet Oxygen Chemistry. Tetrahedron. 2000;56:9151-9179.
24. Moseley, H. The Scientific Basis of PDT. SPIE. 2003;5287:35-38.
25. Takeda, S., K. Nanri, and T. Fujioka. Industrial and Reverse-Industrial Applications of COIL. SPIE. 1996;702:191-194.
26. von Bulow, H. and W. O. Schall. Oxygen-Iodine Lasers for Industrial Applications. SPIE. 1995;2502:258-265.
27. Powell, J. CO₂ Laser Cutting, 2nd Edition. New York: Springer, 1998.
28. Endo, M., F. Wani, S. Nagatomo, D. Sugimoto, K. Nanri, S. Tadeka and T. Fujioka. Development of Industrial COIL. SPIE. 1998; 3574:253-264.
29. McDermott, W.E., N.R. Pchelkin, D.J. Bernard and R.R. Bousek. An Electronic Transition Chemical Laser. Appl. Phys. Lett. 1978;32:469-473.
30. Dahlberg, M.R. and M.E. Cochrane. Tactical High Energy Laser (THEL) as a Weapon System in Future Theater Air and Missile Defense (TAMD). SPIE. 1999;3612:111-116.

31. Manke, G.C., C.b. Cooper, S.C. Dass, T.J. Madden and G.D. Hager. A Multiwatt All Gas-Phase Iodine Laser (AGIL). *IEEE J. Quant. Elec.* 2002;39:995-1002.
32. Henshaw, T.L., T.J. Madden, J.M. Herbelin, G.C. Manke II, B.T. Anderson, R.F. Tate and G.D. Hager. Measurement of Gain on the 1.315 μm Transition of Atomic Iodine Produced from the $\text{NCl}(a^1\Delta) + \text{I}_2(^2\text{P}_{3/2})$ Energy Transfer Reaction. *SPIE*. 1999;3612:147-151.
33. Carroll, D.L. and W.C. Solomon. ElectriCOIL: An Advanced Chemical Iodine Laser Concept. *SPIE*. 2001; 4184:40-44.
34. Kendrick, K.R., C.A. Helms, B. Quillen and R.J. Copland. Quantitative Determination of Oxygen Yield in a Chemical Oxygen-Iodine Laser. *SPIE*. 1998;3268:125-129.
35. Kwirandt, G.R. and W.O. Schall. Basic Experiments on the Production of $\text{O}_2(^1\Delta)$. *SPIE*. 1995;2502:331-337.
36. Zagidullin, M.V., V.D. Nikolaev, N.A. Khvatov and M.I. Svistun. The Sub- and Supersonic COILs Driven by Jet Type Singlet Oxygen Generator. *SPIE*. 1998; **3574**:246-252.
37. Truesdell, K.A., S. E. Lamberson, G. D. Hager. Phillips Laboratory COIL Technology Overview. *AIAA* 92-3003.
38. Losey, M.W., M.A. Schmidt and K.F. Jensen. Microfabricated Multiphase Packed-Bed Reactors: Characterization of Mass Transfer and Reactions. *Ind. Eng. Chem. Res.* 2001;40:2555-2562.
39. Wada, Y., M.A. Schmidt and K.F. Jensen. Flow Distribution and Ozonolysis in Gas-Liquid Multichannel Microreactors. *Ind. Eng. Chem. Res.* 2006; 45: 8036-8042.
40. Gunther, A., M. Jhunjhunwala, M. Thalmann, M.A. Schmidt and K.F. Jensen. Micromixing of Miscible Liquids in Segmented Gas-Liquid Flow. *Langmuir*, 2005; 21: 1547-1555.

41. London, A.P., A.A. Ayon, A.H. Epstein, S.M. Spearing, T. Harrison, Y. Peles and J.L. Kerrebrock. Microfabrication of a High Pressure Bipropellant Rocket Engine. *Sens. Actuators A, Phys.* 2001;A92:351-7.
42. Gianetto, A, and P.L. Silveston, Ed. *Multiphase Chemical Reactors*. New York: Springer-Verlag, 1986.
43. Amador, C., A. Gavrilidis and P. Angeli. Flow Distribution in Different Microreactor Scale-Out Geometries and the Effect of Manufacturing Tolerances and Channel Blockage. *Chem. Eng. J.* 2004; 101:379-390.
44. Sieder, E.N. and G.E. Tate. Heat Transfer and Pressure Drop of Liquids in Tubes. *Ind. Eng. Chem.* 1936;28:1429-1436.
45. Rawlins, W. T., S. Lee, and S. J. Davis. Singlet Oxygen Measurements for Micro-COIL. PSI-2918/TR-2096, May 2006.
46. Inoue, T., M.A. Schmidt and K.F. Jensen. Microfabricated Multiphase Reactors for the Direct Synthesis of Hydrogen Peroxide from Hydrogen and Oxygen. *Ind. Eng. Chem. Res.* 2007;46:1153-1160.
47. Ratner, D.M., E.R. Murphy, M. Jhunjhunwala, D.A. Snyder, K.F. Jensen and P.H. Seeberger. Microreactor-based Reaction Optimization in Organic Chemistry-Glycosylation as a Challenge. *Chem. Commun.* 2005;5:578-583.
48. Ergun, S. Fluid Flow Through Packed Columns. *Chem. Eng. Progress.* 1952;48:89-94.
49. Larkins, R.P., White, R.R. and D.W. Jeffrey. Two-Phase Concurrent Flow in Packed Beds. *AIChE J.* 1961;7:231-236.

50. Losey, M.W., Jackman, R.J., Firebaugh, S.L., Schmidt, M.A., Jensen, K.F., Design and Fabrication of Microfluidic Devices for Multiphase Mixing and Reaction. *Journal of Microelectromechanical Systems*. 2002;11:709-717.
51. Baker, D. Simultaneous Flow of Oil and Gas. *Oil and Gas J.* 1954; 53:183-195.
52. Charpentier, J.C. and M. Favier. Some Liquid Holdup Experimental Data in Trickle-Bed Reactors for Foaming and Nonfoaming Hydrocarbons. *AIChE J.* 1975;21:1213-1218.
53. Talmor, E. Two-Phase Downflow Through Catalyst Beds. *AIChE J.* 1997;23:868.
54. Melli, T.R. and L.E. Scriven. Theory of Two-Phase Cocurrent Downflow in Networks of Passages. *Ind. Eng. Chem. Res.* 1991;30:951-957.

TABLE I

DESIGN PARAMETERS OBTAINED FROM MIT μ COIL OPTIMIZATION STUDY

Parameter	Range	Predicted Optimum	Experimental
Bed cross-sectional area	$1.95 \times 10^{-7} \text{ m}^2$		
Packing diameter	$70 \times 10^{-6} \text{ m}$		
Bed porosity, dimensionless	0.40		
He:Cl ₂ gas inlet rate, 32-channel device	4.2 – 430 cm ³ /min (@STP)	175 cm ³ /min (@STP)	25 – 175 cm ³ /min (@STP)
BHP liquid inlet rate, 32-channel device	0.75 – 7.50 cm ³ /min	3 cm ³ /min	0.5 – 2.5 cm ³ /min
Packed Bed Length	0 – 1 cm	0.516 cm	0.61 cm
Packed-Bed Outlet Pressure	3-40 kPa	6.2 kPa	5 – 35 torr
$N_{Bo_{Cl_2}}$ @ 40 kPa	1.8 – 180	70	10-70
$N_{Bo_{O_2}}$ @ 40 kPa	1.2 – 120	50	8 – 50
$N_{Bo_{O_2H^-}}$ @ 40 kPa	$10^4 - 10^5$	5×10^5	$8 \times 10^4 - 4 \times 10^5$

TABLE II

PROPERTIES OF COOLANT FOR DESIGN OF HEAT EXCHANGER

Property (@ -10°C)	Value
Density	870.11 kg.m ⁻³
Specific heat	1.572 kJ.kg ⁻¹ .K ⁻¹
Thermal Conductivity	0.1171 W.m ⁻¹ .K ⁻¹
Viscosity	2.49x10 ⁻³ Pa.s ⁻¹
Prandtl Number	33.4

LIST OF FIGURES

Figure 1: The miniaturized trickle-bed reactor system; (a) gas-liquid distributors with bifurcations and pressure-drop channels; (b) the micromachined structured packed-bed, top and side-views, (c) gas-liquid separator pores for disengagement via capillary mechanism, (d) cooling channels for heat extraction, (e) singlet-oxygen production, visually confirmed via dimol emission at 634 nm; (f) the packaged microdevice with optical cuvette for measurement of singlet-oxygen concentration via monomol emission at 1280nm; (g) the completed microdevice, top view showing distributor, packed-beds and gas-liquid separator, (h) the completed microdevice, backside view showing inlet and outlet ports for fluidic connections. Images in (b), (c), (d), (e), (f) from [13].

Figure 2: Design flowsheet for microscale trickle-bed system.

Figure 3: Illustration of Capillary Separator Design; (a) liquid-filled stagnant (inactive) separator pores resist gas invasion when $P_{separator} < P_{cap}$; (b) liquid-filled flowing (active) separator pores withdraw liquid at rates determined from Hagen-Poiseuille equation.

Figure 4: Microdevice fabrication; (a) schematic view of device cross-section; (b) backside of completed microdevice identifying individual inlet and outlet ports; (c) frontside view of completed microdevice; (d) internal cooling channels.

Figure 5: Testing methodology; (a) packaging chuck, showing inlet and outlet ports, from [13]; (b) experimental apparatus: (1) Chlorine cylinder; (2) Helium cylinder; (3) Helium mass flow controller; (4) back-pressure controller; (5) liquid supply reservoir; (6) Helium mass flow controller; (7) Chlorine mass flow controller; (8) toggle valve; (9)

pressure transducer; coolant flow controllers for (10) liquid delivery/recovery and (11) microdevice; (12) chiller/recirculator; (13) liquid recovery reservoir; (14) optical cuvette; (15) focusing lense; (16) spectrometer; (17) LN moisture traps; (18) liquid removal pressure controller; (19) gas outlet pressure controller; (20) vacuum pump.

Figure 6: Evaluation of chip performance; (a) single- and two-phase pressure drop parity plot; (b) transient cooling of microdevice; (c) calculated heat transfer coefficient from steady-state cooling experiments. Trendlines calculated from Equations (5) and (6).

Figure 7: Summary of hydrodynamic observations in structured post-bed microreactors (present work; [39,50]; (a) Baker coordinate map, mapping corrected gas space velocity vs. corrected liquid space velocity; (b) Charpentier and Favier coordinate map, mapping corrected ratio of liquid-to-gas space velocity ratio to corrected gas space velocity; (c) Talmor coordinate map, mapping corrected gas-liquid space velocity ratio vs. dimensionless function of Weber and Reynolds #.

Figure 8: Estimation of gas-liquid mass transfer area, assuming stagnant, annular flow; (a) minimum pore throat; (b) maximum pore throat.

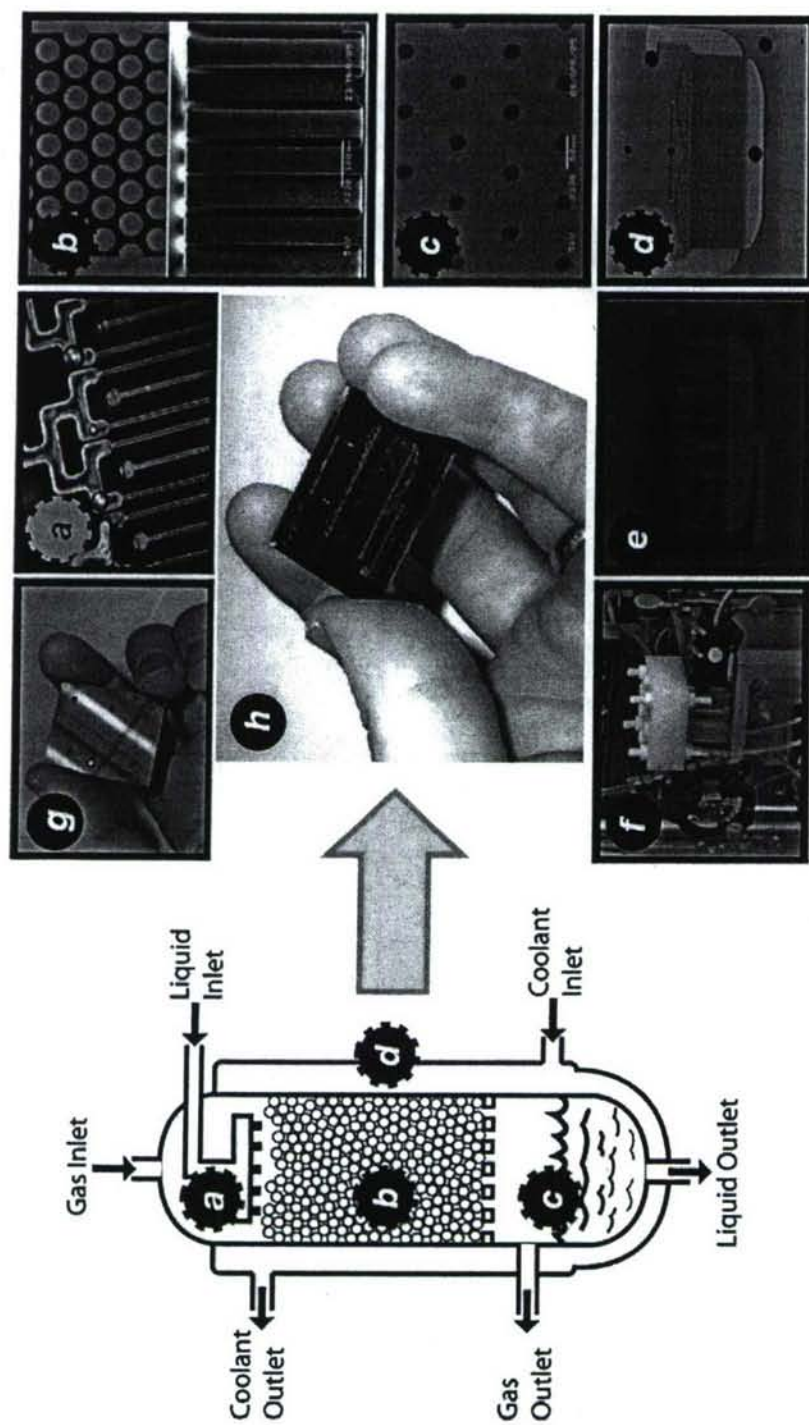


Figure 1

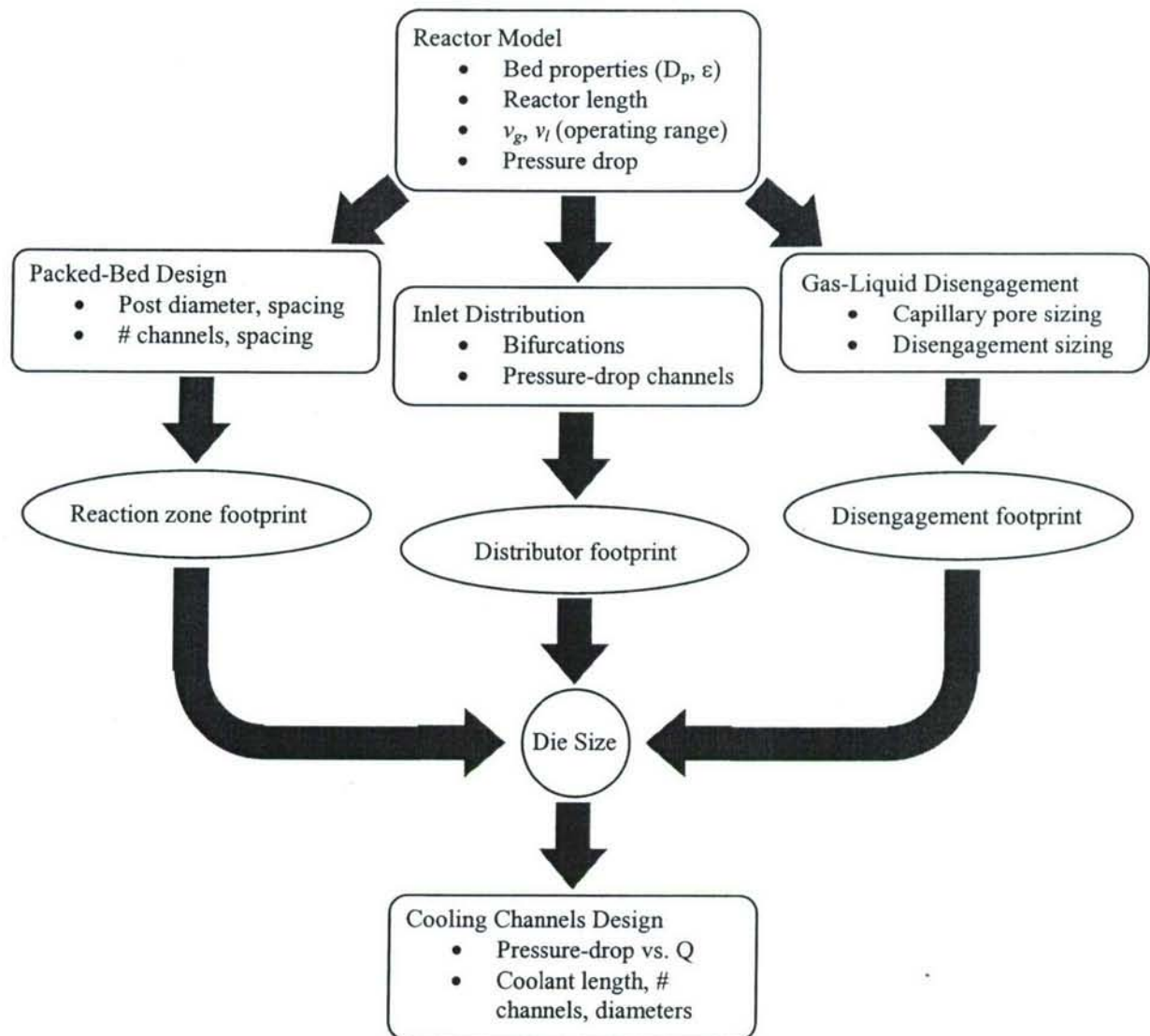
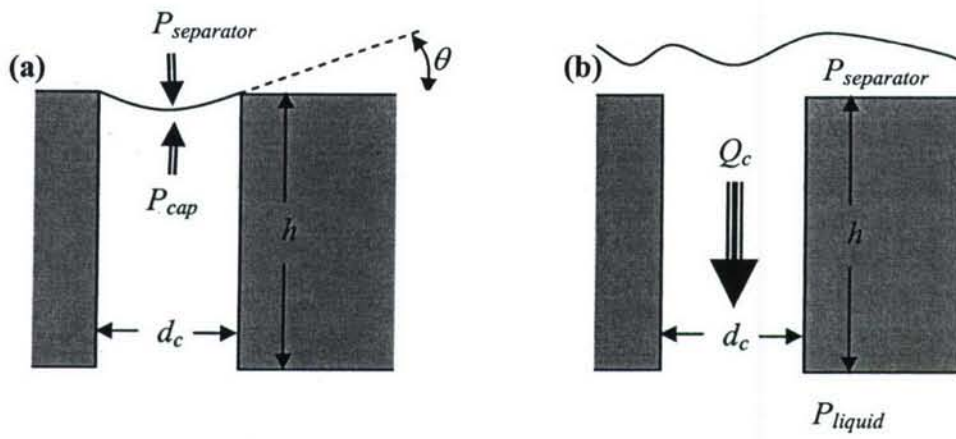


Figure 2



$$P_{cap} \leq (P_{separator} - P_{liquid}) < 0$$

Figure 3

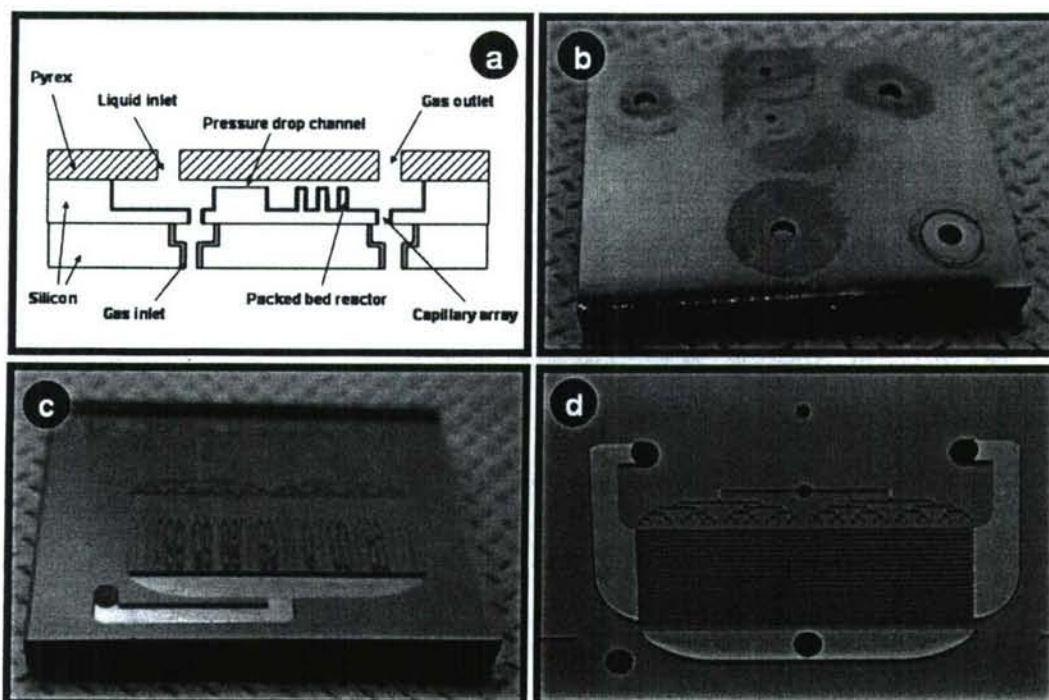


Figure 4

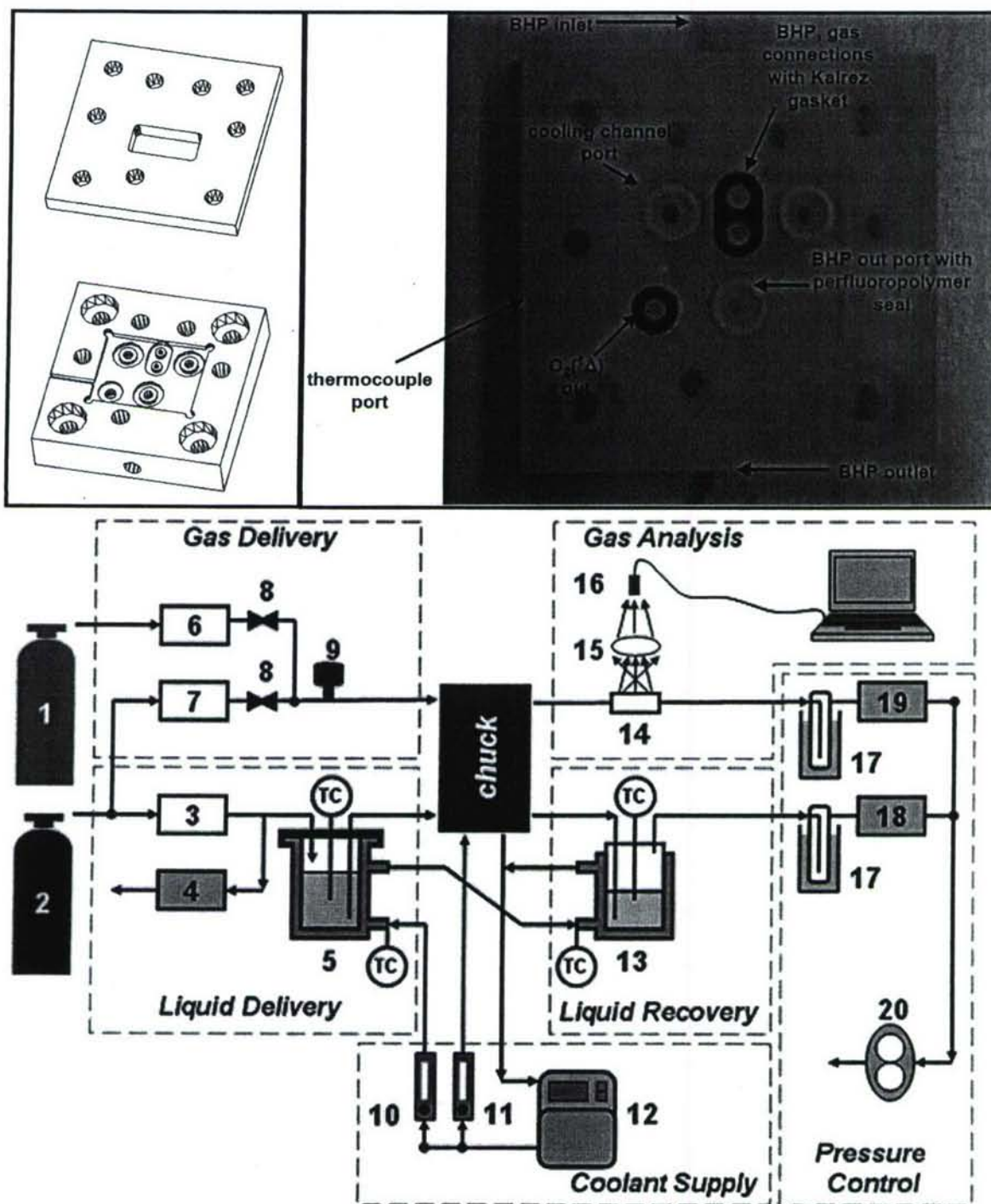


Figure 5

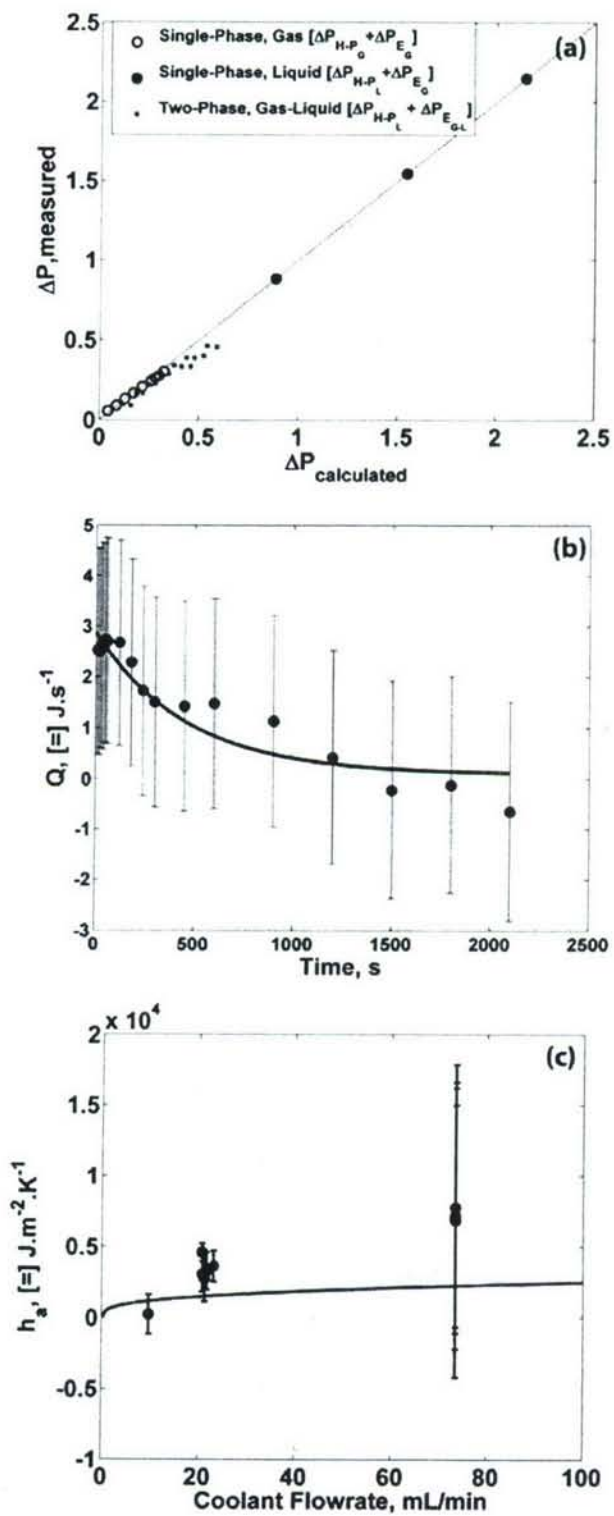


Figure 6

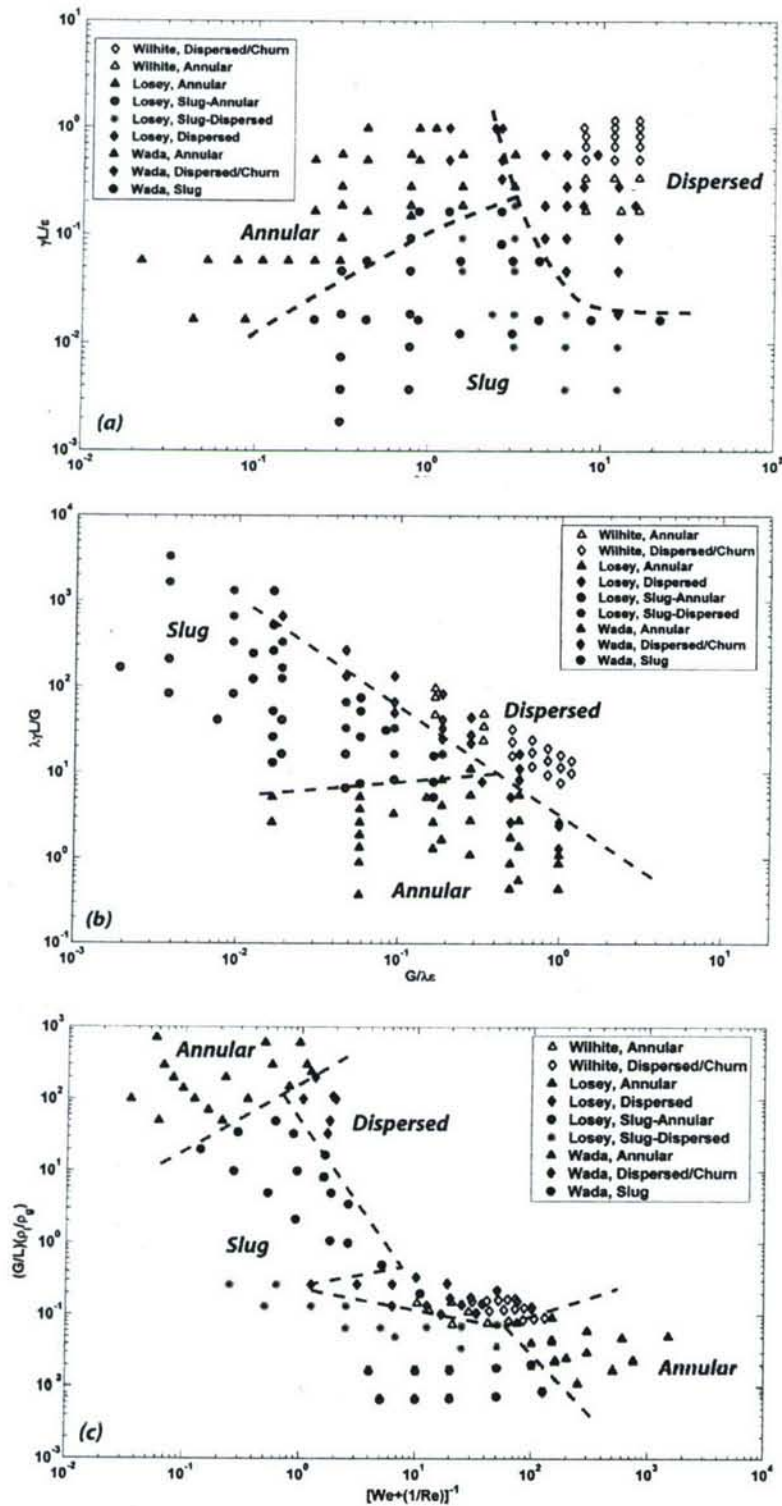


Figure 7

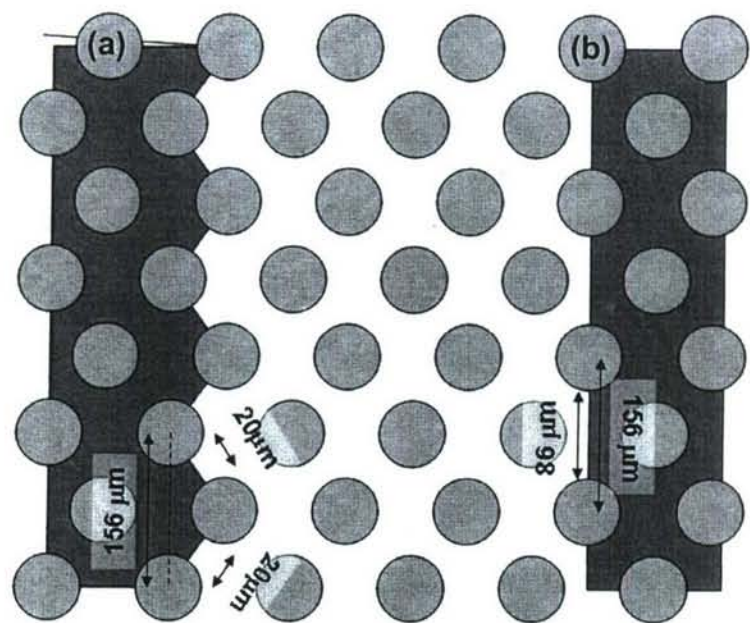


Figure 8